NASA CONTRACTOR REPORT

NASA CR-1805

JOINT DETERMINATION OF ORBITS OF SPACECRAFT AND MOONS OF MARS BY OPTICAL SIGHTING OF THE MOONS

by Charles B. Grosch and Donald F. Nickel

Prepared by
CONTROL DATA CORPORATION
Minneapolis, Minn. 55435
for Langley Research Center

NATIONAL AERONAUTICS AND SPACE ADMINISTRATION • WASHINGTON, D. C. • JULY 1971

1. Report No.	2. Government Accession No.	3. Recipient's Catalog No.
NASA CR-1805		

4. Title and Subtitle	5. Report Date
JOINT DETERMINATION OF ORBITS OF SPACECRAFT AND MOONS OF MARS BY OPTICAL SIGHTING OF THE MOONS	July 1971
	6. Performing Organization Code

7. Author(s)	8. Performing Organization Report No.
Charles B. Grosch and Donald F. Nickel	RD 2013
	10. Work Unit No.

9. Performing Organization Name and Address	11. Contract or Grant No.
Control Data Corporation 8100 34th Avenue So. Minneapolis, Minn. 55435	NAS1-9617
	13. Type of Report and Period Covered Contractor Report

12. Sponsoring Agency Name and Address	14. Sponsoring Agency Code
National Aeronautics and Space Administration Washington, D.C. 20546	

15. Supplementary Notes

16. Abstract

The feasibility of using a scanning optical system to provide the attitude and trajectory of an unmanned spacecraft during an orbit about Mars is investigated. It is assumed that the spacecraft is nearly attitude stabilized by a Sun-Canopus Tracking System. The scanning instrument yields a more accurate determination of its attitude by use of stellar detections across three slits. The same slits occasionally detect transits of the Martian moons, and these transits together with the stellar transits are sufficient to yield the trajectories of the moons and spacecraft as well as the higher harmonic coefficients of the Martian gravitation potential.

In the investigation, the accuracy with which the attitude, trajectories, and potential can be determined from the measurements is studied. Also, an analysis of the perturbations of the spacecraft's position due to the moon's force fields is given. Finally, the instrument detection problems are discussed and instrument design parameters are derived.

17. Key Words (Suggested by Author(s))	18. Distribution Statement
Onboard orbit determination Martian gravitational potential Martian moons Inertially stabilized scanning instrument Orbit determination by sighting Martian moons	Unclassified-Unlimited

19. Security Classif. (of this report)	20. Security Classif. (of this page)	21. No. of Pages	22. Price*
Unclassified	Unclassified	142	$3.00

*For sale by the National Technical Information Service, Springfield, Virginia 22151

FOREWORD

This report was prepared by Edina Space and Defense Systems, Division of Control Data Corporation, for National Aeronautics and Space Administration, Langley Research Center, under Contract NAS1-9617. Charles B. Grosch and Donald F. Nickel served as principal investigators in performing the analytical and instrumentation functions, respectively. Control Data Corporation desires to particularly acknowledge the technical guidance of Harold A. Hamer and Albert A. Schy of the Aeronautical and Space Mechanics Division, Flight Mechanics Branch, National Aeronautics and Space Administration, Langley Research Center, NASA Technical Representatives.

TABLE OF CONTENTS

TABLE OF CONTENTS -- Continued

JOINT DETERMINATION OF ORBITS OF SPACECRAFT AND MOONS OF MARS BY OPTICAL SIGHTING OF THE MOONS

By Charles B. Grosch and Donald F. Nickel

SUMMARY

The principal purpose of this study is to investigate the feasibility of using the moons of Mars as optical targets from which accurate navigational information may be derived during an unmanned Martian mission. The mission trajectory is fixed to be highly eliptical and have an orbital period equal to the rotational period of Mars.

Before considering the central problem, an investigation of position perturbations of the spacecraft due to the moons themselves is undertaken. An analysis is given which yields an approximate solution without undue numerical computation. Numerical results are then presented. It was found that the position perturbations of the spacecraft are almost entirely due to Phobos and are a quite complicated function of the particular spacecraft orbit chosen. A simple physical explanation of the results is given which, to a certain extent, enables one to predict the perturbations over any given spacecraft orbit.

The availability of moon sightings is first considered. Even though a moon may be within the instrument's field of view, it may well be undetectable because of Mars-scatter sunlight. It was found that Deimos is generally detectable with sufficient frequency, but in order to detect Phobos a sufficient number of times, a time interval of approximately eighty days is required.

Two spacecraft orbits are then studied in detail to determine the navigation accuracy which can be achieved by the moon sighting with the recommended scanning instrument. Navigation, here, is used to mean the determination of the trajectories of the spacecraft, the two moons, and the potential of Mars. It was found that if the direction to each moon can be measured with an accuracy of one arc minute, then the position accuracy of the spacecraft and Deimos is about five km, but since Phobos is sighted less frequently, its position accuracy is about ten km. The accuracy of the coefficient of the lower harmonics is about $\pm 10^{-6}$. The higher harmonics are more poorly determined because of the relatively high altitudes of the three bodies. It is recommended that they not be treated as unknowns.

To compute a moon direction in a preferred coordinate system from the moon transits requires that the attitude of the spacecraft be known. This attitude is determined from stellar transits and an assumed attitude motion model. The need for a model arises because the scanning instrument does not determine attitude at each transit; each transit provides only a constraint upon the attitude. The accuracy of the attitude determination is thus dependent upon the distribution of the observed stars, the accuracy of the model, and the accuracy of the measured transits.

Two spacecraft attitude models were investigated. Both assumed that the spacecraft is nearly inertially stabilized by a Sun-Canopus tracking system, but the spacecraft roll, pitch, and yaw may vary linearly over the data gathering interval. The first model assumed a five minute interval, the second a ten minute interval.

Second magnitude and brighter stars must be detected to obtain sufficient stellar transits. For either attitude model, the accuracy with which the moon's direction can be computed is somewhat less than the one minute assumed in computing the navigational errors. If the five minute interval model can be used, the resulting error is approximately five arc minutes, while it is approximately three arc minutes if the ten minute interval model can be used. For any case, the navigation errors must be scaled to include the effect of these instrument direction determination errors.

In completing the study, the instrument capable of achieving the accuracies outlined above is designed. In addition, two instrument related problems are discussed. They are: (1) determining a signal detection and processing system which can operate over the intensity range produced by the bright moons and dim stars, and (2) a method of compensating for the moons not being point targets. The recommended instrument weighs seven pounds, used 7.9 watts of power and is 18.8 inches long (including the sunshield).

INTRODUCTION

In principle, if the directions to the moons were measured at several points along the trajectory of a spacecraft orbiting Mars, these directions would be sufficient to imply the trajectories of the spacecraft, the trajectories of the moons, and also various unknowns associated with the force field near Mars. The underlying analysis is given in reference 1 and actual results using our moon during the ATS-III mission are given in reference 2.

In many ways, the moons are ideal navigational targets for use by a spacecraft orbiting Mars. They would be nearly point targets, quite bright, have no atmospheres to refract the optical line of sight, and have sufficient spread in their positions so that a relatively strong geometry can be obtained. However, unless the mission is rigidly planned beforehand, the direction of the moons, as viewed from the spacecraft, would be unknown and highly variable.

To provide mission flexibility, it was found necessary to consider a scanning rather than a tracking detection and measuring system. If a tracking system were considered, then a very difficult acquisition problem is presented for the following reasons:

(1) It is desirable to detect both moons. Moreover, it is desirable to detect them simultaneously even though they might be separated by as much as 90°.

(2) During an extended mission, the directions from the spacecraft to each moon vary considerably. Moreover, Mars itself will hinder moon detectability, either by direct obscuration or by scattering sunlight. In any event, it will be necessary to reacquire the moons periodically.

(3) During some periods, favorable sightings of Phobos occur during time intervals as short as fifteen minutes. Thus, the acquisition problem must be solved fairly quickly.

(4) If additional moons, undetectable from Earth, are present, a scanning sensor will have a good chance of seeing them. A fixed or tracking sensor would not.

For these reasons, a scanning system whose instantaneous field of view is small, but whose effective field is large by virtue of the scanning motion, was chosen. A schematic of the scanning system chosen is shown in figure 1. As shown in the figure, the optical system establishes three slits; detections of the moons and brighter stars are then made by these slits which are caused to rotate with respect to the spacecraft.

Spacecraft Trajectory and Attitude

Certain of the parameters associated with the spacecraft's trajectory and

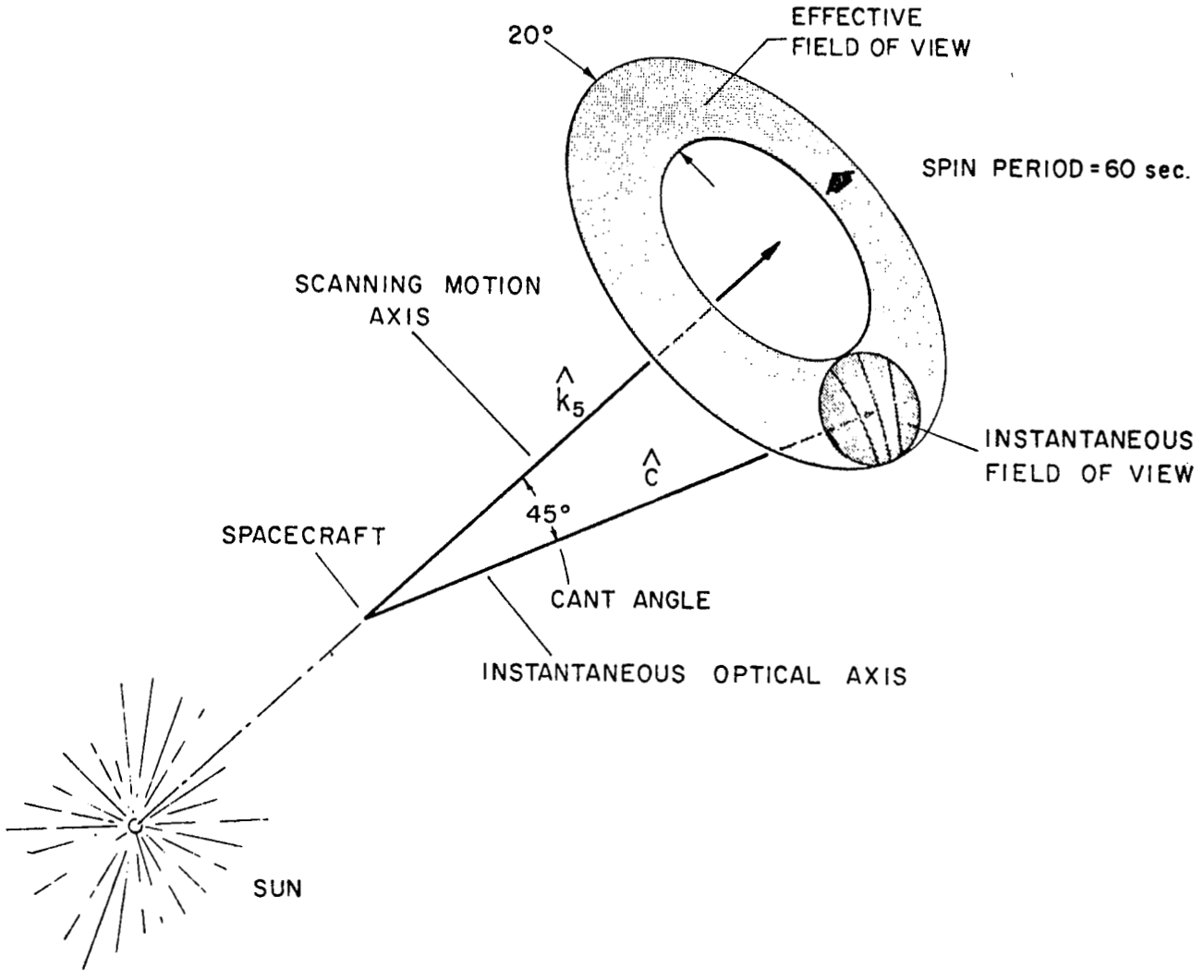

Figure 1: The scanning field of view.

attitude were fixed during the study. These fixed parameters are as follows:

Periapsis altitude	--	1000 km
Period	--	24.6228 hr. (synchronous)
Orbital mission life	--	90 days
Injection	--	0^h 6 March 74 = 2,442,120.5 J.D.

The periapsis altitude and orbital period yield the unperturbed orbital elements:

$e = 0.78199$
$a = 20415.5$ km

The time of injection is not an important parameter, i.e., results to be shown are a weak function of this time. This time, however, does place Saturn in the instrument's field of view over almost half of the twenty day mission. This fact is used advantageously to obtain a target for the computation of the spacecraft attitude. All other targets used for attitude computation are stars whose magnitudes are brighter than 2.2.

The attitude of the spacecraft is assumed to be nearly inertially stabilized by a Sun-Canopus tracking system. More specifically, consider a coordinate system S_5 such that $\hat{k}_5$ is the anti-sun direction and $\hat{i}_5$ is in the Sun-Canopus plane. It is then assumed that a system fixed in the spacecraft has an orientation which varies linearly with respect to S_5 (i.e., the three angles are linear functions of time) over any time interval of length five minutes and ten minutes (two cases). Stellar transits are then gathered by the instrument and these transits are used to compute the attitude.

The assumption concerning attitude model is not justified within. Such a justification could be made only if the attitude control system, the control law, and the external torques were specified. In fact, the attitude model cannot be chosen independent of these inputs. For example, if the external torques are small, and the system uses reaction jets whose impulses are known at each firing, then a better attitude model would be a polygonal line (each of the three angles). The change in the derivative of the polygonal line is at the time of a firing and specified by the impulse and the spacecraft moments of inertia.

The Moons, Phobos and Deimos

Mars has two small moons, Phobos and Deimos, which were discovered in 1877 the American astronomer Hall. The satirist, Jonathan Swift, however, spoke of their existence and even gave a surprisingly accurate description of the characteristics nearly two hundred years before in his Gulliver's Travels.

Earth-based observations of these moons are quite difficult. Optical sightings require at least a twelve inch aperture, and quantitative measurements can only be made near periods of mean opposition of Mars which occur roughly every 780 days. At these times, the orbits of Phobos and Deimos subtend twenty-five and sixty-two seconds of arc, respectively. Very recently, data from on-board optical sightings of Phobos during the Mariner VII mission was analyzed.

Surprisingly, it was found that Phobos's albedo was only 0.067 which is less than that given for any other celestial body. The albedo previously assumed for Phobos was 0.1, which has caused astronomers to underestimate the size of Phobos.

The observed perturbations of the orbits of the moons have been used by astronomers to compute the mass of Mars and its dynamic flattening. However, the most accurate data to date has been supplied by the Mariner-Mars fly-by mission. A serious discrepancy exists between the flattening of Mars as implied by the orbits of its moons (dynamic flattening) and the flattening as obtained by direct optical measurements. The dynamic flattening is about one-third the optical flattening. No acceptable reason for this discrepancy has been found, but if this discrepancy does exist, then the surface of Mars is far from being an equipotential surface.

Since Phobos is quite close to Mars (2.7 planetary radii versus 6.9 for Deimos), its orbit is significantly perturbed. Some investigators have reported an acceleration of Phobos along its orbital path ($.002^{\circ}/\text{year}^2$), others have not. If this acceleration exists, then two mechanisms are proposed: atmospheric drag, or a tital couple acting between an elastic Mars and Phobos. The astronomer, Shklovsky, proposed that drag does exist; in which case, Phobos would spiral inward. He calculated its remaining lifetime to be three million years -- exceptionally short for an astronomic body.

At any given time, the accuracy with which the positions of the moons can be determined from present measurements is somewhat difficult to estimate. The order of magnitude of the position errors is 500 km in the radial direction (with respect to the center of Mars), 500 km in the direction perpendicular to the orbital plane, and "several times" this value in the along-track direction.

A photographic search for other moons of Mars was made at the time of oppositions during the years of 1954, 1956, and 1958. No new moons were detected and it was concluded that none exist with a diameter greater than 1.4 kilometers.

Tables I - III list the astronomic characteristics of Mars and its moons as used in this study. Comments are given in the text concerning the accuracy of several of the numerical values.

TABLE I

PHYSICAL CONSTANTS FOR MARS

Mass	Radii (km)	Flattening	Potential	Rotational Period	Spin Axis Direction
$(6.4192 \pm .0002) \times 10^{26}$ grams	$R_c = 3388 \pm 26$ $18 \leq R_e - R_p \leq 36$	$(150 \pm 50)^{-1}$	$C_{20} = -2.011 \times 10^{-3}$ $C_{30} = 10^{-6}$ $C_{40} = 10^{-6}$ $C_{50} = 10^{-6}$ $C_{21} = 2 \times 10^{-5}$ $S_{21} = 1 \times 10^{-5}$	24.6228 hr.	r.a. = 317.01° dec. = 53.09°

TABLE II

ORBITAL PARAMETERS OF MARS

$a = 1.5236915$ A.U.
$e = 0.093381$
$i = 1.8498387^{\circ}$ (measured from the ecliptic plane)
$\Omega = 49.3594543^{\circ}$
$\omega = 335.5863554^{\circ}$
Time at perihelion = 2,441,890.5 J.D.
Time at aphelion = 2,442,230.5 J.D.

TABLE III

CONSTANTS OF THE MARTIAN SATELLITES

Constant	Phobos	Deimos
Mass	3.46×10^{19} grams	4.32×10^{18} grams
Radii (km)	$R_e = 9$, $R_p = 11$	4
a (km)	9400	23,500
e	0.017	0.0028
i (with respect to Martian Equator)	0.95°	1.3°
Period (hrs.)	7.6538	30.2986
Albedo	0.067	0.1

SYMBOLS

a, e, Ω, ω, i	orbital elements of spacecraft's unperturbed orbit
A_M	average number of stars per square degree within the brightness range $M + \frac{1}{2}$ to $M - \frac{1}{2}$
$\hat{c}$	unit vector in direction of instrument's optical axis
C_{nm}, S_{nm}	coefficients of spherical harmonics in the expansion of the potential of Mars
$\hat{d}_i$	unit vector from spacecraft to ith moon (1, 2) corresponds to (Phobos, Deimos)
D	effective optical aperture diameter
$f(t)$	signal obtained from the output of a detector as a target (moon or star) cross a scanning slit
Δf	filter noise equivalent bandwidth
$h(t)$	impulse response of filter
$\hat{i}_5$	unit vector perpendicular to $\hat{k}_5$ and such that Canopus is in the $\hat{i}_5$, $\hat{k}_5$ plane
I_s	peak star signal current
$\hat{k}_5$	unit vector in direction of instrument's spin axis
$\overline{N_1^2}$	shot noise power
$\overline{N_2^2}$	noise power due to scanning the stellar background of stars dimmer than the threshold magnitude
N_B	total integrated starlight from stars of sixth magnitude and dimmer which is expressed as equivalent tenth magnitude stars per unit area on the celestial sphere
$\overline{R}$	position vector of the spacecraft with respect to center of mass of Mars
$\widehat{s\omega}$	slit width in arc minutes
S_A	total slit area projected on the celestial sphere as seen by the photocathode through the slit plane
S_K	photocathode sensitivity per unit area of optical aperture for a zero magnitude star having a given spectral energy distribution

SYMBOLS - (Continued)

t_1	random time error in the leading edge threshold crossing
t_2	random time error in the trailing edge threshold crossing
T_s	transit time of a point star image to cross the slit
$y(t)$	filter output of the signal $f(t)$
ϵ_o	overall optical efficiency
$\overline{\lambda^2}$	square of the star intensity averaged with respect to star density and star magnitude with the average taken only for stars which are dimmer than the threshold magnitude M_o
$\nu(0)$	initial true anomaly of a moon
ρ_{12}	correlation coefficient for random noise amplitudes at times t_1 and t_2
ω_c	filter frequency parameter
$\sigma^2(t_s)$	variance of the star pulse transit time

Coordinate systems:

e_3, a_3	elevation and azimuth, respectively, of $\hat{d}$ -- these angles being measured with respect to S_3
S_1	celestial coordinate system
S_3	Mars coordinate system
S_5	Sun-Canopus system

In general:

A'	is the transpose of a matrix A
$\hat{u}$ or $\vec{u}$	implies $\hat{u}$ unit vector
δu	is the error in u
$\sigma(\delta u)$	is the standard deviation of δu

PERTURBATIONS OF SPACECRAFT'S TRAJECTORY DUE TO THE MOONS

Introduction

Perturbations of the spacecraft's trajectory due to the attractive forces generated by the moons is an important consideration, not because of the intrinsic interest in obtaining precise numerical values, but because of the desirability of knowing whether or not these perturbations are significant. If so, a knowledge of the position of the moons (as a function of time) is required as input information to a trajectory determination program. In addition, if some known set of initial parameters for the spacecraft's trajectory yield significant perturbations, then this information would be of value in defining the mission. If, however, some known set of initial parameters yields insignificant perturbation, then this information would be equally valuable. The analysis described in this section was performed to ascertain the effect of the perturbations.

To facilitate the analysis the following assumptions are made:

(1) The orbits of the moons are circular in the equational plane of Mars. These orbits will be unperturbed by the force field of the spacecraft.

(2) If the moons did not exist, the orbit of the spacecraft would be a Kepler ellipse (i.e., the only perturbing forces on the spacecraft are due to the moons).

(3) Phobos and Deimos are both spheres of radius 8 and 4 km, respectively, and have mean densities equal to that of Mars.

(4) The unperturbed elements a and e of the spacecraft are fixed at a = 20415.5 km and e = 0.78199. The effect of different sets of Ω, ω, and i, however, is studied.

Assumption (3) is used to compute the mass of each moon. Since the magnitude of the perturbations of interest is directly proportional to these masses, an explanation of the validity of assumption (3) is presented below:

The value used for the mean densities of the moons is an estimation. It is highly improbable, however, that the mean densities exceed that of Mars. In fact, Redmond and Fish (reference 3) give the density of chrondite as an upper bound on the density of Phobos.

Also, the radii of the moons are estimated from their observed brightness and assumed albedo, both of which are poorly known(1). Since an error of 0.1 in magnitude implies a 40% error in radius, the calculated radii are highly sensitive to small errors in the observed brightness.

Table IV gives a comparison of values assumed here and those given by Redmond and Fish. It can be noted that the assumed mass of Phobos is 4.55 times greater than the upper bound given in reference 3.

TABLE IV

SOME PHYSICAL CHARACTERISTICS OF THE MOONS OF MARS

	Phobos		Deimos	
	Present Study	Redmond and Fish	Present Study	Redmond & Fish
Radius (km)	8.0	6.4 to 7.8	4.0	not given
Density (g/cm^3)	4.02	2.8 to 3.76	4.02	"
Mass (g)	3.46×10^{19}	3.1 to 7.6×10^{18}	4.32×10^{18}	"

(1) Phobos was photographed in 1969 by Mariner 7 (reference 4). The albedo was estimated to be 0.065, which is "lower than that known for any planet, satellite, or asteroid in the solar system". Its shape was determined to be more nearly that of a prolate spheroid with an equatorial radius of 9 km and a polar radius of 11 km. These dimensions imply a volume 2.1 times greater than that used here. This information is recent and was received too late to be used in the analysis. However, it does indicate that the mass used in this study is probably a slight underestimate rather than a large overestimate, as is predicted by Redmond and Fish.

Equations of Motion

Reference is made to figure 2. Let

$\bar{R}$ position vector of the spacecraft with respect to the center of the mass of Mars

$\bar{\rho}_i$ position vector of the ith moon with respect to the same center (i = 1 denotes Phobos, i = 2 denotes Deimos)

$\bar{d}_i = \bar{R} - \bar{\rho}_i$ vector from ith moon to the spacecraft

m_i mass of ith moon ($m_1 = 3.46 \times 10^{19}$ grams, $m_2 = 4.32 \times 10^{18}$ grams).

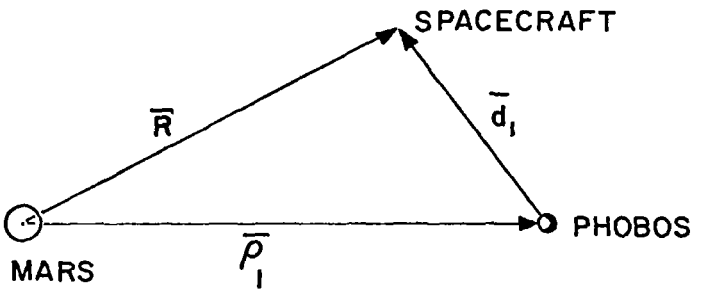

Figure 2: The relative position of Mars, Phobos, and spacecraft

As shown in reference 5, the equation of motion of the spacecraft is then

$$\ddot{\bar{R}} + \frac{\mu \bar{R}}{R^3} = -G \sum_{i=1}^{2} \left(\frac{m_i}{d_i^3} \bar{d}_i + \frac{m_i}{\rho_i^3} \bar{\rho}_i \right) \qquad (1)$$

where

G universal gravitational constant

μ = GM, M being the mass of Mars = 6.4192×10^{26} grams

= 5.5429×10^{11} km^3/hr^2.

Approximation of the Equation of Motion

Determination of the perturbation of a minor planet's position is a classical and central problem in celestial mechanics. The classical method of attacking the problem is through the LaGrange equations which are the differential equations which the oscillating orbital elements must satisfy in the presence of a disturbing function. In the classical theory, advantage is taken of the fact that the orbital eccentricity and inclination are small. In the case under study, the eccentricity of the spacecraft is quite large ($e \doteq .8$) and all inclinations are of interest. Hence, it is difficult to apply the classical methods to obtain an approximate analytic solution. However, the method used in reference 6 can be applied to reduce the numerical computations.

Let

$$\bar{X} = \begin{pmatrix} \bar{R} \\ \dot{\bar{R}} \end{pmatrix},$$

$$\bar{X}_o = \begin{pmatrix} \bar{R}_o \\ \dot{\bar{R}}_o \end{pmatrix}$$

where R_o satisfies equation (1) with the right-hand side zero. Thus, the terminus of $\bar{R}_o$ is on the reference Kepler orbit.

The differential equation satisfied by $\bar{X}$ can be written as

$$\dot{\bar{X}} = \bar{F}(\bar{X}) + \begin{pmatrix} 0 \\ 0 \\ 0 \\ \bar{A}(\bar{X}, t) \end{pmatrix}$$

where $\bar{A}(\bar{X}, t)$ is a small acceleration which arises because of the forces on the spacecraft due to the presence of the moons. An approximate equation satisfied by $\delta\bar{X} = \bar{X} - \bar{X}_o$ is

$$\dot{\delta\bar{X}} = \frac{\partial\bar{F}}{\partial\bar{X}}\,\delta\bar{X} + \begin{pmatrix} 0 \\ 0 \\ 0 \\ \bar{A}(\bar{X}_o, t) \end{pmatrix} \qquad (2)$$

where

$\frac{\partial\bar{F}}{\partial\bar{X}}$ is a 6 x 6 matrix evaluated at $\bar{X}_o(t)$.

Let

$\delta\bar{X}(0) = 0$, then the solution to equation (2) is

$$\delta\bar{X}(t) = \Phi(t) \int_0^t \Phi^{-1}(s) \begin{pmatrix} 0 \\ 0 \\ 0 \\ \bar{A}(\bar{X}_o, s) \end{pmatrix} ds \qquad (3)$$

where

$$\dot{\Phi}(t) = \frac{\partial \bar{F}}{\partial \bar{X}} \Phi(t), \quad \Phi(0) = I .$$

An analytic solution for $\Phi(t)$ and $\Phi^{-1}(t)$ is given by Kochi (reference 6).

If Φ is partioned so that

$$\Phi = \begin{pmatrix} \Phi_1 & \Phi_2 \\ \Phi_3 & \Phi_4 \end{pmatrix} , \text{ then reference 6 states that}$$

$$\Phi^{-1} = \begin{pmatrix} \Phi_4' & -\Phi_2' \\ -\Phi_3' & \Phi_1' \end{pmatrix} , \text{ where } A' = A^T .$$

Hence, the first three components of equation (3) yield

$$\delta\bar{R}(t) = \int_0^t \left(\Phi_2(t) \Phi_1'(s) - \Phi_1(t) \Phi_2'(s) \right) \bar{f}(s) \, ds \qquad (4)$$

where

$$\bar{f}(s) = \bar{A}(\bar{X}_o(s), s).$$

The integration in equation (4) may be simplified. From the analytic form of $\Phi(t)$ it can be observed that each $\Phi_i(t)$ can be written as

$$\Phi_i(t) = \alpha_i(t) + t\beta_i(t)$$

where

$$\alpha_i(t) \text{ and } \beta_i(t)$$

are periodic with a period equal to that of the reference Kepler orbit. Denote this period as T. Also let $t = nT + \tau$, $0 \leq \tau < T$. To take advantage of the periodicity of the α's and β's, the integral is written

$$\delta\bar{R}(t) = \int_0^{nT} + \int_{nT}^{nT + \tau} .$$

With little loss of generality, one may choose the initial time as the time at which the reference Kepler position is at its periapsis. Thus, the spacecraft trajectory and its reference trajectory are chosen to be tangent at this time. The force field of the moons will later separate the trajectories. With this choice the form of α's and β's is given in reference 6 as

$$\alpha_1(t) = \begin{pmatrix} a_{11} & a_{12} & 0 \\ a_{21} & a_{22} & 0 \\ 0 & 0 & a_{33} \end{pmatrix}$$

$$\alpha_2(t) = \frac{1}{n^*(1+e)} \begin{pmatrix} a_{14} & a_{15} & 0 \\ a_{24} & a_{25} & 0 \\ 0 & 0 & a_{36} \end{pmatrix}$$

$$\beta_1(t) = 3\,\frac{1+e}{1-e}\; n^* \begin{pmatrix} b_1 & 0 & 0 \\ b_2 & 0 & 0 \\ 0 & 0 & 0 \end{pmatrix}$$

$$\beta_2(t) = \frac{3}{1-e} \begin{pmatrix} 0 & b_1 & 0 \\ 0 & b_2 & 0 \\ 0 & 0 & 0 \end{pmatrix}$$

where

$$n^* = \sqrt{\frac{\mu}{p^3}}\,, \quad p = a\left(1 - e^2\right)$$

a and e being elements of the reference orbit.

Thus,

$$\int_0^{nT} = \int_0^{T} \left(U(u,\tau)\; \bar{g}\,(u) + V(u,\tau)\; \bar{h}\,(u) \right) du$$

where

$$U(u,\tau) = \frac{1}{n^*\,(1+e)} \left(-\alpha_1(\tau)\; \alpha_2'(u) + \alpha_2(\tau)\; \alpha_1'(u) \right)$$

(equation continued)

$$+ \frac{3(nT + \tau)}{1 - e} \begin{pmatrix} b_1(\tau) & c_1(u) & b_1(\tau) & c_2(u) & 0 \\ b_2(\tau) & c_1(u) & b_2(\tau) & c_2(u) & 0 \\ 0 & & 0 & & 0 \end{pmatrix}$$

$$V(u, \tau) = - \frac{3}{1 - e} \begin{pmatrix} b_1(u) & c_1(\tau) & b_2(u) & c_1(\tau) & 0 \\ b_1(u) & c_2(\tau) & b_2(u) & c_2(\tau) & 0 \\ 0 & & 0 & & 0 \end{pmatrix}$$

$$\bar{g}(u) = \sum_{i=0}^{n-1} \bar{f}\,(i\,T + u)\,, \quad n \geq 1$$

$$\bar{h}(u) = u\,\bar{g}\,(u) + T \sum_{i=1}^{n-1} i\,\bar{f}\,(i\,T + u)\,, \; n \geq 1$$

here

$$c_1 = a_{12} - a_{14}$$

$$c_2 = a_{22} - a_{24}\,.$$

Finally,

$$\delta\bar{R}(t) = \int_0^T \left(U(u, \tau)\,\bar{g}\,(u) + V(u, \tau)\,\bar{h}\,(u) \right) du$$

$$+ \int_0^\tau \left(U(u, \tau) + (u + n\,T)\,V\,(u, \tau) \right) \bar{f}\,(n\,T + u)\,du\,. \qquad (5)$$

Formulas for the a's, b's and c's are given in Appendix A.

The matrices $U(u, \tau)$ and $V(u, \tau)$ are also a function of a and e, but not of the other orbital elements. Thus, this formulation is convenient here for a and e have been given fixed numerical values. However, $\bar{g}(u)$ and $\bar{h}(u)$ are functions of the other orbital elements.

To utilize equation (5) with Kochi's $\xi(t)$, $\bar{f}(s)$ must be written with components resolved in a coordinate system which moves with the Kepler orbit. These components must be in the radial direction; in the direction perpendicular to the radial and orbital normal directions (positive in the direction of orbital motion) and in the direction of the orbital normal.

Thus,

$$\bar{f}(s) = \mu \frac{m_1}{M} \bar{f}_1(s) + \mu \frac{m_2}{M} \bar{f}_2(s) \qquad (6)$$

where

$$\bar{f}_i(u) = \begin{pmatrix} \dfrac{-R_o + \rho_i P_{1i}}{d_i^3} - \dfrac{P_{1i}}{\rho_i^2} \\ \dfrac{\rho_i P_{2i}}{d_i^3} - \dfrac{P_{2i}}{\rho_i^2} \\ \dfrac{\rho_i P_{3i}}{d_i^3} - \dfrac{P_{3i}}{\rho_i^2} \end{pmatrix}$$

$$P_{1i} = \cos(\Omega - \nu_i)\cos(\omega + \nu) - \sin(\Omega - \nu_i)\cos i \sin(\omega + \nu_i)$$

$$P_{2i} = -\cos(\Omega - \nu_i)\sin(\omega + \nu) - \sin(\Omega - \nu_i)\cos i \cos(\omega + \nu_i)$$

$$P_{3i} = \sin(\Omega - \nu_i)\sin i$$

$$\nu_i = \nu_i(s) = \nu_i(0) + \sqrt{\frac{\mu}{\rho_i^3}}\, s$$

$$\nu = \nu(s)$$

$$R_o = R_o(s)$$

$$d_i = \sqrt{R_o^2 + \rho_i^2 - 2\rho_i R_o P_{1i}} \ .$$

here

- i inclination of reference Kepler orbit
- Ω longitude of ascending node
- ω argument of periapsis
- ν_i true anomaly of the ith moon
- ν true anomaly of the spacecraft if it were on the reference Kepler orbit

It must be noted that equation (5) was derived by using a single reference Kepler trajectory to linearize the equation of motion (1). For most purposes this is too inaccurate an approximation, but here the additive forces are so small that the approximation is adequate. To indicate the adequacy of the approximation, one case was run in which the numerical result from equation (5) was compared with the direct numerical integration of equation (1). The results were in agreement within 0.1 km after ten spacecraft orbits.

Numerical Results

Figure 3 plots the position perturbations of the spacecraft as a function of ω (the argument of periapsis) at three positions along the 30th orbit of the spacecraft. That is, at $t = 0$, the perturbed and unperturbed position and velocity of the spacecraft are chosen to be identical. The attractive forces of the moons then are allowed to separate the two trajectories. At $t = 0$, the spacecraft is at periapsis and both moons have zero true anomaly.

The salient features shown in figure 3 are as follows:

1. The perturbations of position are largest at periapsis and smallest at apoapsis.

2. The perturbations are a strong function of ω. Large perturbations being present for $\omega = 80^\circ$ and 110°.

Figure 4 gives the perturbations at periapsis and apoapsis as a function of the number of spacecraft orbits. Here $\omega = 80^\circ$, which is near a critical argument of periapsis. Note that the position perturbations are approximately a quadratic function of time.

Virtually all the perturbations shown in figures 3 and 4 are produced by Phobos, the inner and more massive moon. Not shown in these figures is the resolution of the position perturbations into three orthogonal components. At periapsis and apoapsis the direction of the perturbation is chiefly in the along-track direction. The perturbations of figure 4 are in the negative direction (opposite to that of the orbital motion), while in figure 3 some of the values of ω yield positive along-track errors while others yield negative errors. Between periapsis and apoapsis the radial component is significant, but the cross-track is always small.

Figure 5 shows contours of equal along-track perturbations at the periapsis of the 30th orbit of the spacecraft. Here $i = 40^\circ$. Again, note that critical values of ω exist near $\omega = 80^\circ$ and 100°. No critical values of Ω exist. Also, there is a zero contour near $\omega = 90^\circ$ and the along-track perturbations have opposite signs on opposing sides of this contour.

Figure 6 is a plot of the effect of variations in ω and time upon the along-track perturbations of periapsis. The results shown in figures 3, 4, 5, and 6 are summarized as follows:

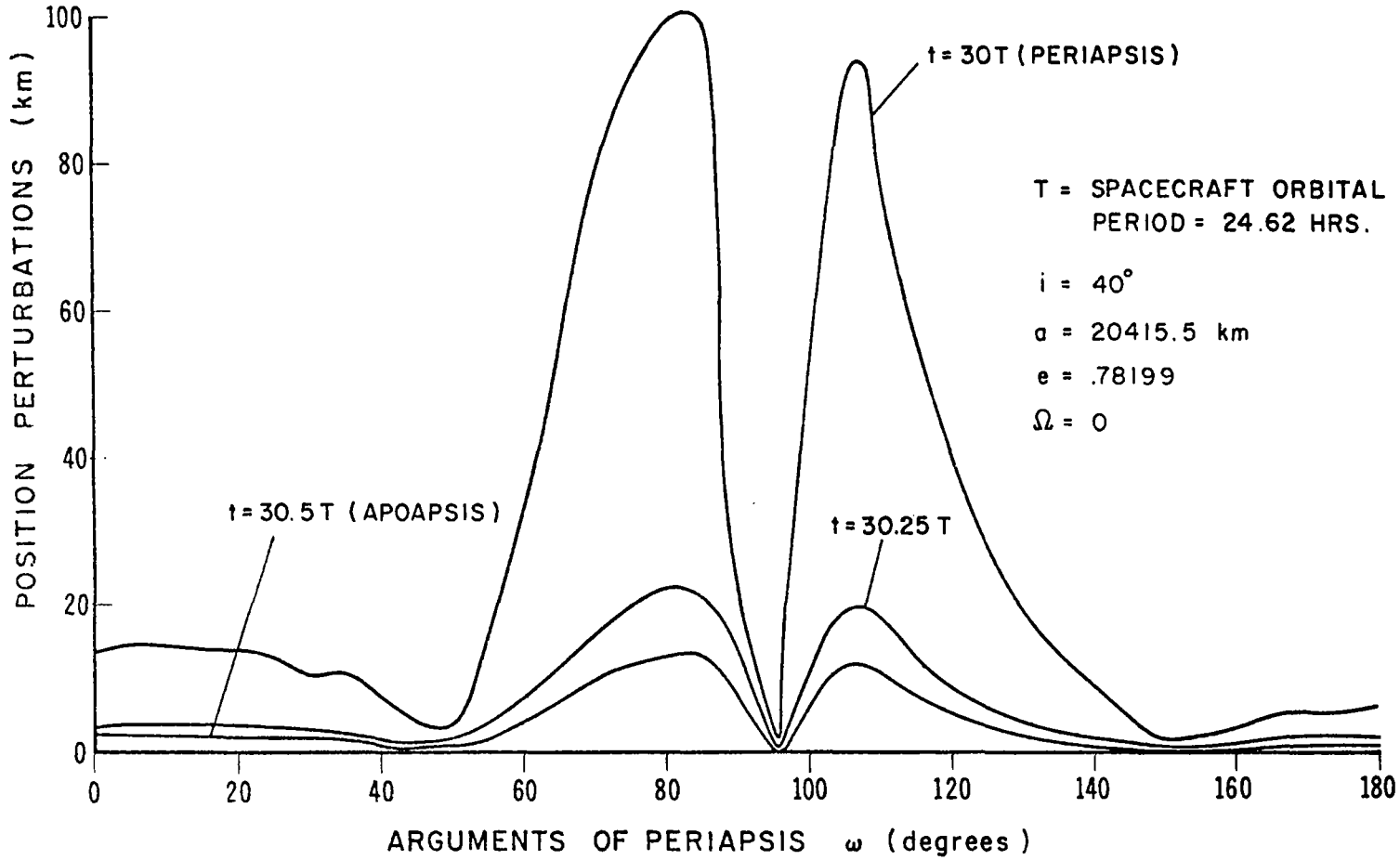

Figure 3: Position perturbations due to Phobos and Deimos as a function of ω at three points on the 30th orbit of the spacecraft.

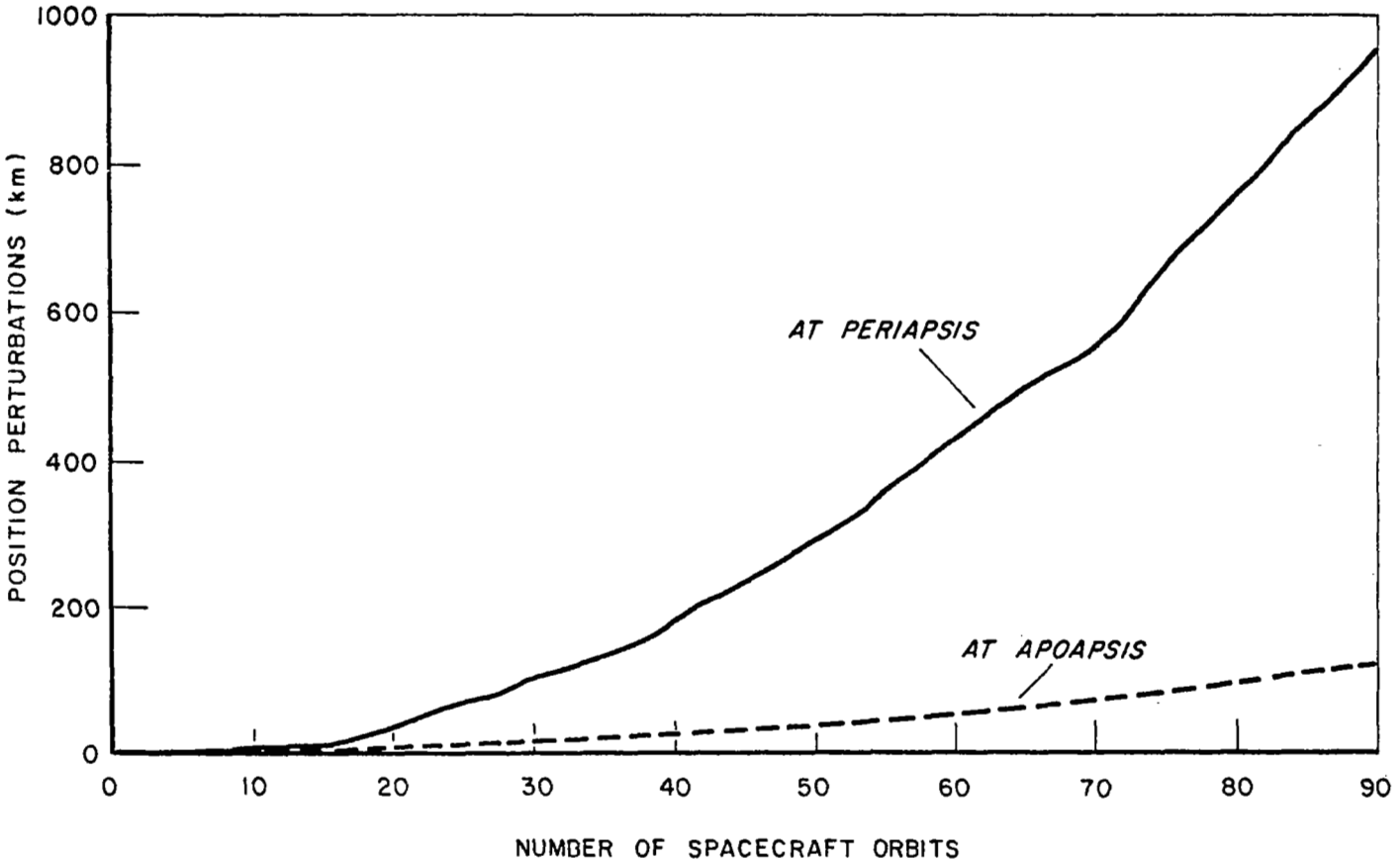

Figure 4: Position perturbations at periapsis and apoapsis as a function of number of spacecraft orbits. $\Omega = 0$, $\omega = 80^{o}$, $i = 40^{o}$.

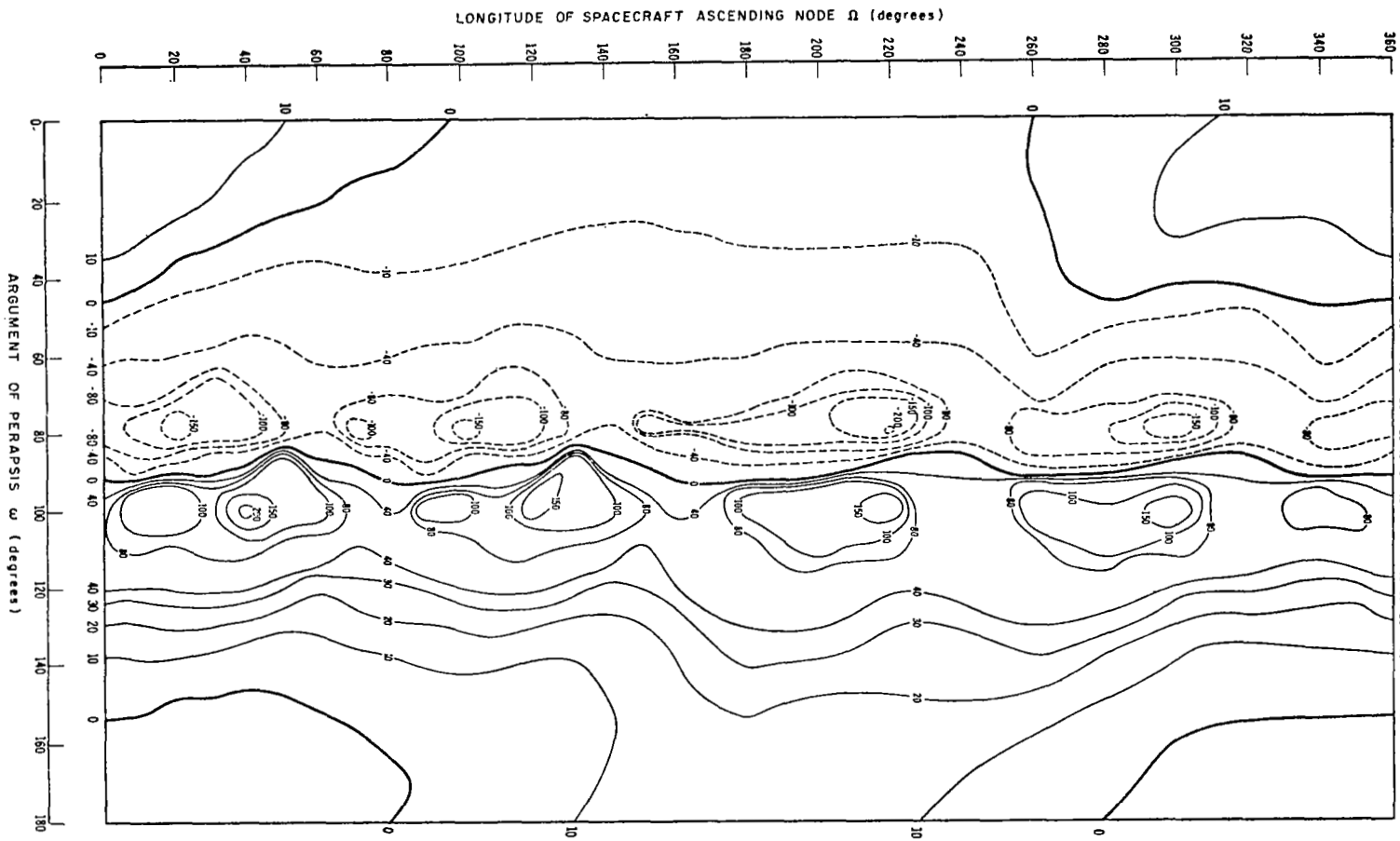

Figure 5: Contours of constant along-track position perturbation (measured in km) at periapsis after 30 orbital periods. The unperturbed elements i, e, and a are fixed so that $i = 40^{\circ}$, a = 20415.5 km, and e = .78199.

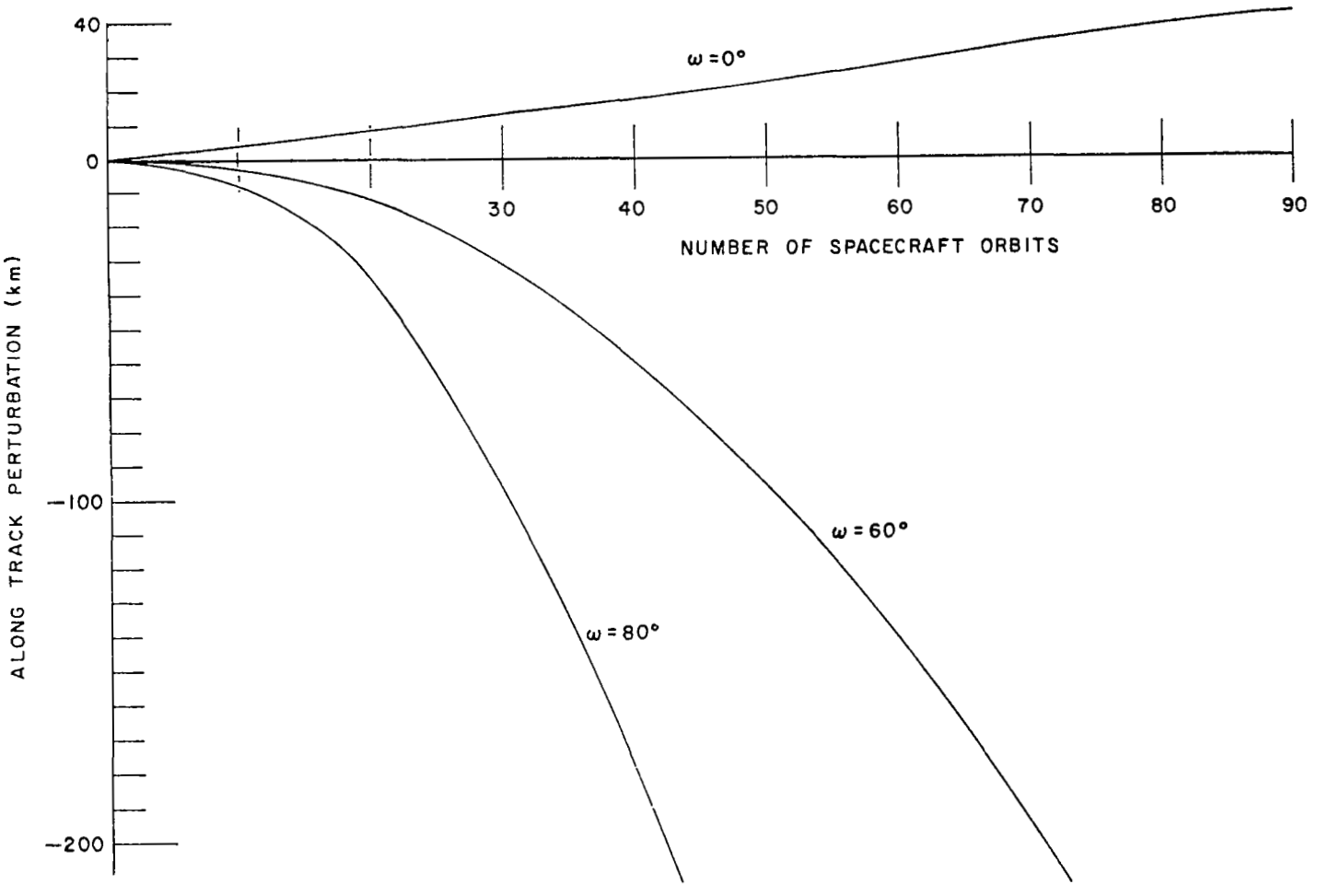

Figure 6: Along-track perturbations at periapsis as a function of number of spacecraft orbits $\Omega = 0$, $\omega = 0^{\circ}, 60^{\circ}, 80^{\circ}$, $i = 40^{\circ}$.

1. The perturbations due to Phobos can be as large as 200 km after thirty spacecraft orbits. However, those due to Deimos are generally less than one km. An exception occurs near $\omega = 40^{\circ}$, 140° which yields perturbations as large as 22 km.

2. Throughout any one orbital period the perturbations are always largest at periapsis and smallest at apoapsis.

3. The cross-track perturbations are always small. At periapsis and apoapsis the perturbations are chiefly along-track. Between periapsis and apoapsis, the radial component can be significant.

4. For any fixed true anomaly, and if ω is near 80° or 100°, the perturbations are approximately a quadratic function of the number of orbital periods of the spacecraft. For ω removed from the critical values, the perturbations increase less rapidly.

5. The perturbations are a weak function of Ω, but a strong function of ω. Near $\omega = 80^{\circ}$, 100° the perturbations are quite large, but near $\omega = 90^{\circ}$ (periapsis farthest from the Martian equator) they are small. In addition, the along-track perturbations are of opposite signs across a zero near $\omega = 90^{\circ}$.

It is important that the numerical results be given a physical rationale, for only then can results be predicted for cases other than those plotted. The results 2 and 5 (of the above summary) require some further explanation.

The equation of motion of the spacecraft (1), does not allow a constant energy of the spacecraft in that energy is transferred to the spacecraft via the moons. The major effect of a change in energy upon the orbital element is a change in the semi-major axis, a. Now, if a non-zero δa exists, and all other Kepler elements remain unchanged, then at periapsis

$$\begin{aligned} \delta r_p &= \delta a \\ \delta s_p &= -3\pi n \sqrt{\frac{1+e}{1-e}}\, \delta a \end{aligned} \tag{7}$$

while at apoapsis

$$\begin{aligned} \delta r_a &= \delta a \\ \delta s_a &= -\frac{3\pi}{2} \sqrt{\frac{1-e}{1+e}}\, (2n+1)\, \delta a \end{aligned} \tag{8}$$

where δr and δs are, respectively, the radial and along-track perturbations, and n is the number of spacecraft orbital periods. Since $e \doteq .8$, for fixed n, $\delta s_p \doteq 9\, \delta s_a$ which is approximately satisfied by our numerical results (figures 3 and 4). Equations (7) and (8) are not an accurate constraint followed by the numerial results, but they do predict a larger perturbation at periapsis than at apoapsis.

To aid in the explanation of result 5, consider figure 7. Shown here are three spacecraft trajectories which differ only in their location of periapsis. Trajectories for $\omega = 0$, 78.8°, and 90° are shown. But, before considering the effect of periapsis location, consider the effect of changes of Ω. If Ω is changed slightly, then only the relative initial position of Phobos[2] is changed, but after thirty spacecraft orbits, approximately 101 revolutions of Phobos occur. Thus, one would expect the perturbations to depend only weakly on Ω, at least for large n.

A change in ω does more than change the relative initial position of the bodies; for at a "critical" ω the paths of the bodies will intersect. This is illustrated in figure 7. First note that if such an intersection is to take place, it must be along the line of nodes of the spacecraft's orbit. If $\omega = 0$, then the intersection of the spacecraft's orbit with the ascending line of nodes is interior to the orbit of Phobos, while the intersection with the descending line of nodes is exterior. As ω increases to 180°, the intersection along the descending node moves toward the center of Mars. At $\omega = 78.8^\circ$ it is at the orbital radius of Phobos. This is a "critical" value[3] of ω. A second critical value of ω exists at $\omega = 111.2^\circ$, but for this case the intersection of the two paths occurs at the ascending node.

At and near a critical value of ω, close encounters with Phobos can be expected. These close encounters in turn imply relatively large perturbations.

Since the spacecraft has its maximum speed at periapsis, and since $\omega = 78.8^\circ$ implies an intersection with Phobos along the descending node; it is expected that the close encounters with Phobos would perturb the spacecraft in the negative along-track direction. This is indeed the case as shown in figure 5. The second critical value of ω, i.e., $\omega = 111.2^\circ$ can similarly be expected to give rise to positive along-track perturbation. This is also the case.

Thus far all results shown are for $i = 40^\circ$, but results for other inclinations cannot differ greatly except for the singular case $i = 0^\circ$. Results for this inclination are shown in figure 8 in the same format as figure 3. In addition to position perturbations at three points along the thirtieth spacecraft orbit, the values of the spacecraft argument of periapsis, ω, that yield a collision with Phobos are shown. Such a collision occurs only if

$$\bar{R}(t, \omega) = \bar{R}_1(t)$$

which implies that $|\bar{R}(t, \omega)| = 9350$ km. Thus, (refer to figure 9)

$\nu = 101.19^\circ$ or 258.81°.

---

(2) Deimos need not be considered since its effects are negligible.

(3) For $i = 0^\circ$, all values of ω are "critical", otherwise the critical value of ω is independent of i.

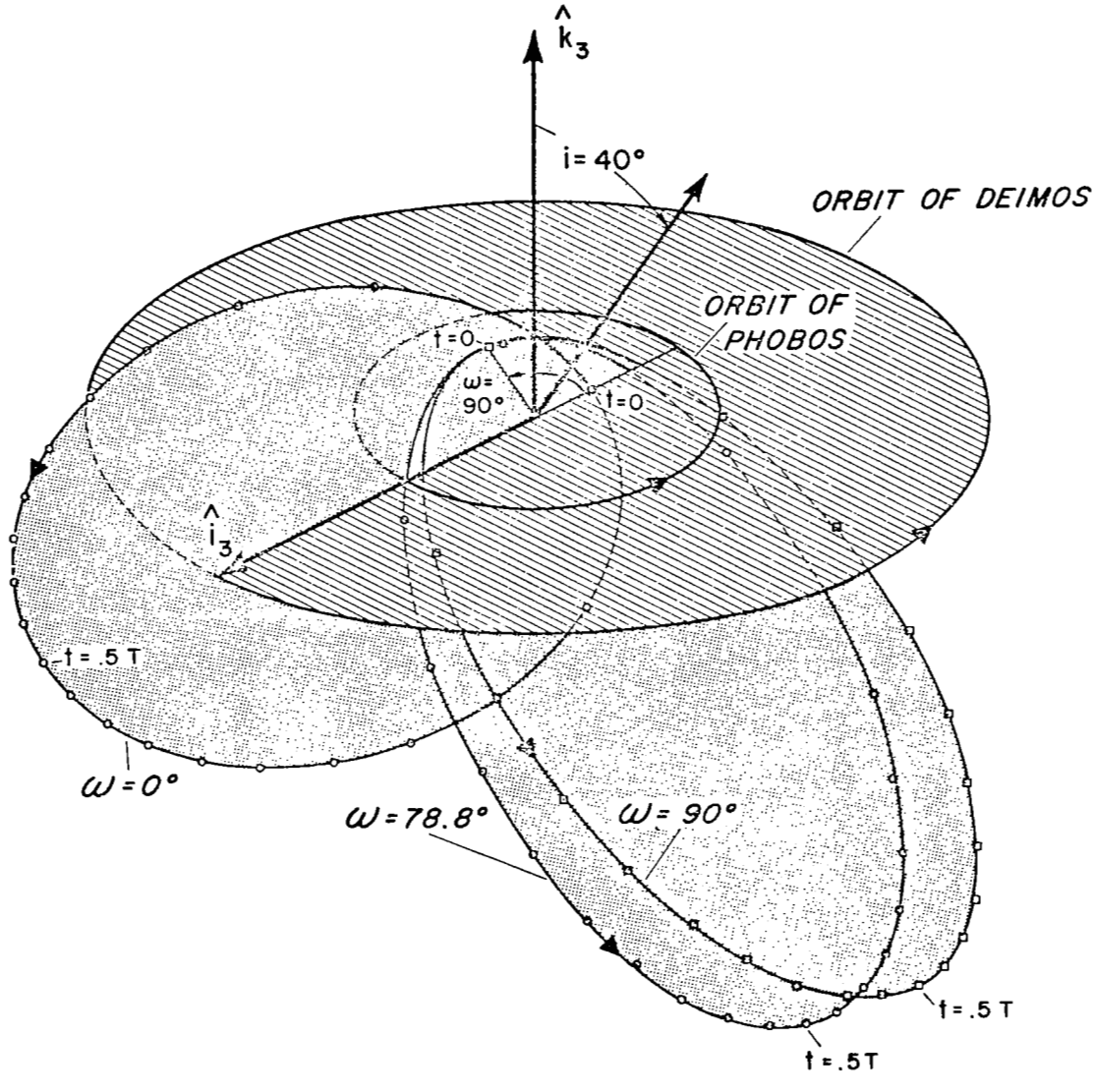

Figure 7: Geometry of three spacecraft orbits, each of which has the same orbital elements except for ω . Ω = 180°, i = 40°

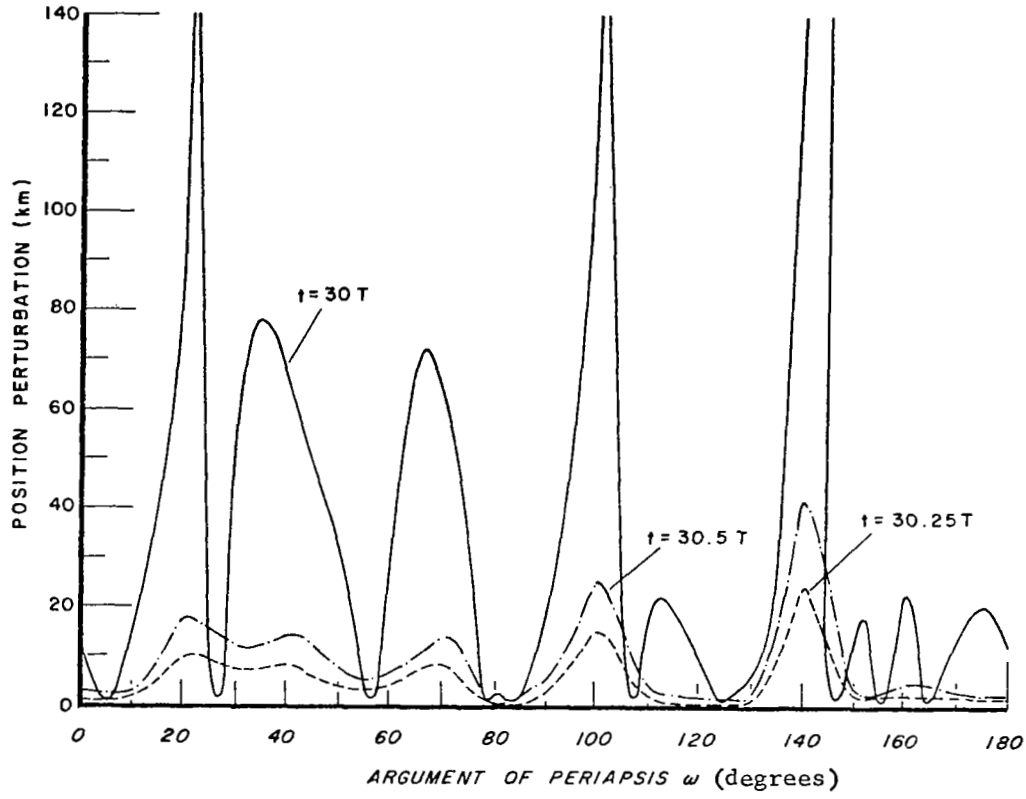

VALUES OF ω FOR WHICH COLLISION OCCURS AT ν = 101.19° : ω_{11}

1,3 15,48 29,93 11,35 25,80 7,22 12,38

10,32 24,77 6,19 20,64 2,5 16,51 21,67 3,9

27,87 9,29 23,74 5,16 19,61 1,3 15,48 29,93

4,13 18,53 0,0 14,45 28,90 10,32 24,77 6,19

VALUES OF ω FOR WHICH COLLISION OCCURS AT ν = 258.81° ω_p

Figure 8: Position perturbations due to Phobos as a function of ω at three points on the 30th orbit of the spacecraft. $i = 0^{\circ}$. The number of complete revolutions of the spacecraft and Phobos associated with each ω which yields collision is shown as number pairs.

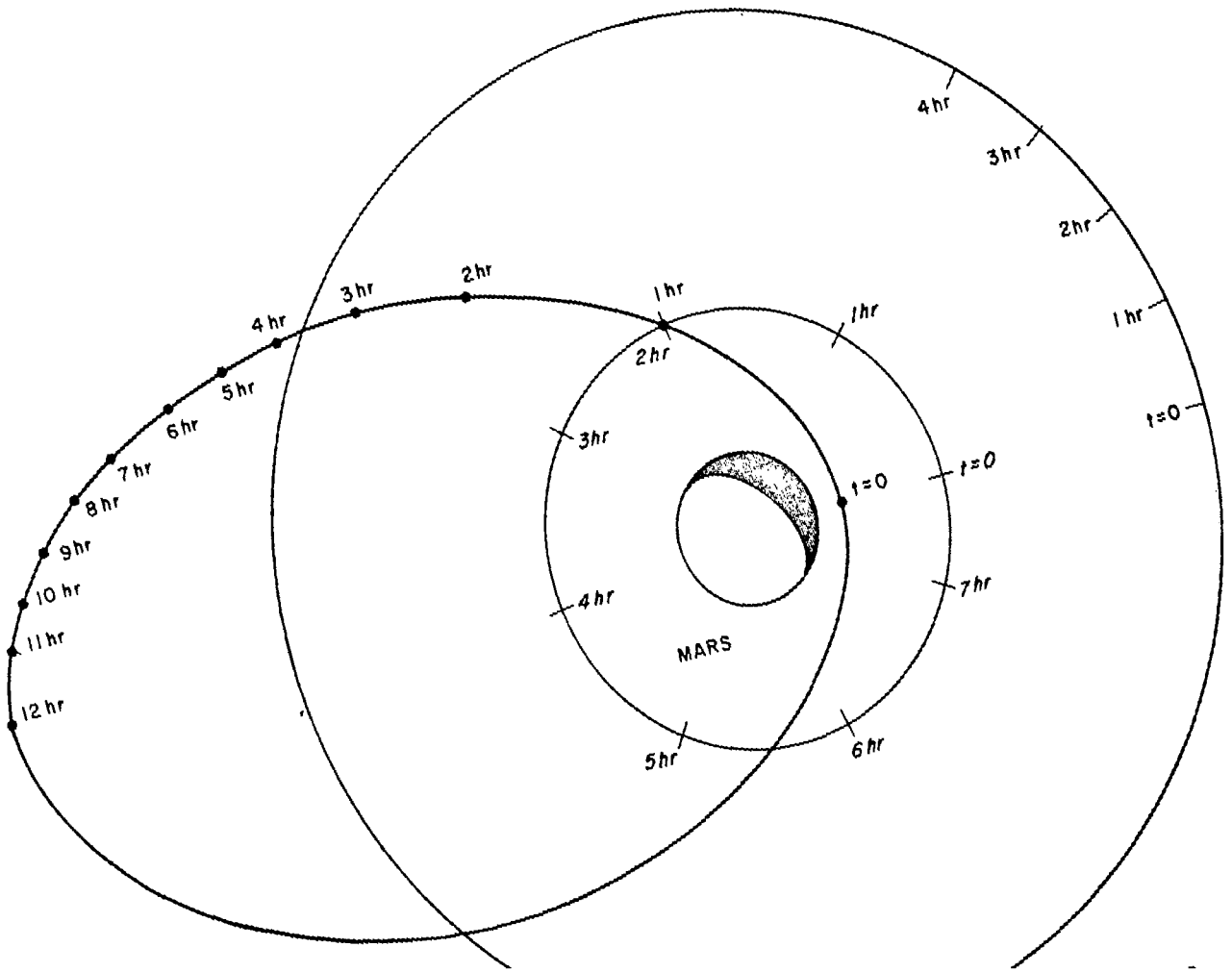
4hr
3hr
2hr
1hr
t=0
1hr
2hr
3hr
4hr
5hr
6hr
7hr
8hr
9hr
10 hr
11 hr
12 hr
1hr
2hr
3hr
t=0
t=0
7hr
4hr
MARS
5hr
6hr

An explanation of the results shown in figure 8 will now be given. By a previous argument, values of ω near those which yield collision at $\nu = 101.19^{o}$ are expected to imply a negative along-track perturbation. The converse holds (positive along-track perturbations) for all values of ω near those which imply collision at $\nu = 258.81^{o}$.

Denote the values of ω which yield collision at $\nu = 101.19^{o}$ as ω_n (because they tend to produce a negative along-track perturbation), and those which yield collision at $\nu = 258.81^{o}$ as ω_p. Note from figure 8 that for $\omega = 21.9^{o} = \omega_n$ a collision occurs after 1 + spacecraft orbits and 3 + Phobos orbits. Now, for all values of ω near 22^{o} a large perturbation results. Consider now $\omega = 55^{o}$. Note that a small perturbation is present near this value of ω. This might be expected, for there exists a $\omega_n = 54.8^{o}$ and a $\omega_p = 56.7^{o}$. Since these collision yielding values cause perturbations in the opposite directions, a cancellation of effects can be expected. In general, if ω_p and ω_n are approximately equal and occur after approximately the same number of spacecraft orbits, then it should be expected that small perturbations will result for values of ω near ω_p and ω_n. On the other hand, if ω_p (or ω_n) takes on a value which is relatively distant from any ω_n (or ω_p), then large perturbations can be expected.

DETECTABILITY OF THE MOONS

Introduction

An initial concern is that the proposed scanning system may be unable to detect the moons a sufficient number of times so as to yield an accurate solution to the navigation problem. This concern is present because the scan can very well carry the field of view near or into the sunlit Martian hemisphere and the reflected scattered sunlight may generate a sufficiently high noise level in the sensor photodetector to obscure the signal generated by the moon.

Figure 10 shows the geometry for the case $i = 0^\circ$ and the sun in the plane of the Martian equator. The spin direction of the instrument is the negative sun direction, $\hat{k}_5$, and the optical axis, $\hat{c}$, is inclined 45°. Additional assumptions are as follows:

1. The instrument's field of view is 20°, with $\hat{k}_5$ as the center of the field of view (figures 1 and 10).

2. The moons are not detectable if obscured by Mars or exterior to the scanned field.

3. If there exists a ray from the spacecraft to a point on the visible sunlight portion of Mars, such that the angle between the instantaneous optical axis and the ray is less than 40°, then the moon is not detectable. The method of implementing this assumption is considered as Appendix B.

4. The orbit of the spacecraft is a Kepler ellipse with a = 20415.5 km and e = 0.78199.

The general problem of the viewing geometry relative to a spacecraft and the moons is discussed by Harrison and Campbell (reference 7). These authors consider the distance of closest approach, approximate frequency of this approach, solar lighting of the moons, and direction to the moon for four particular spacecraft orbits. However, the viewability assumption (3) was not imposed by these authors.

Results

Cases which have been examined are as follows:

$i = 0^\circ, 30^\circ, 60^\circ, 90^\circ$

$\omega = 0^\circ, 60^\circ, 120^\circ, 180^\circ, 240^\circ, 300^\circ$

$\Omega = 0^\circ, 60^\circ, 120^\circ, 180^\circ, 240^\circ, 300^\circ$

$\nu(0) = 0^\circ, 60^\circ, 120^\circ$

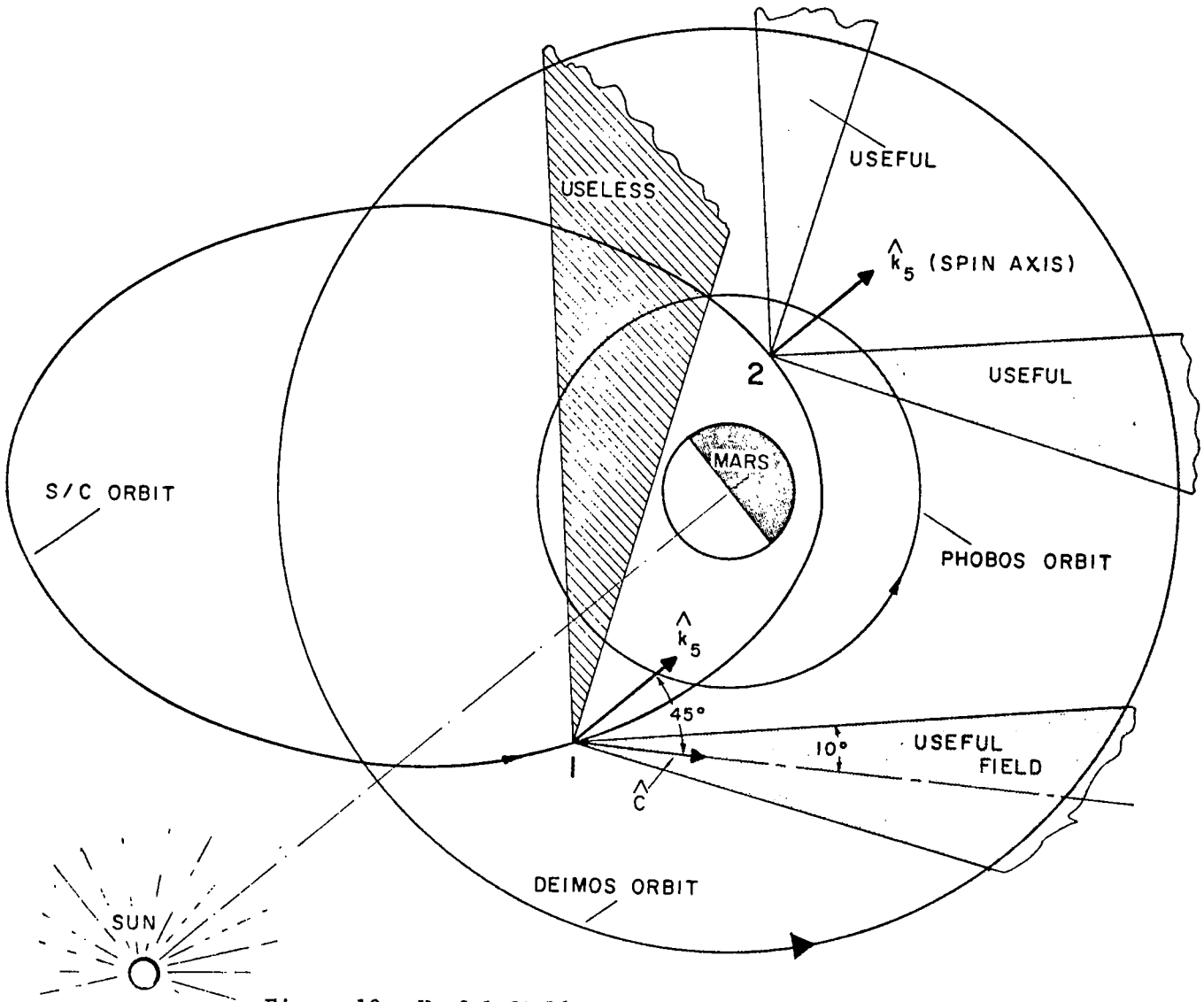

Figure 10: Useful field of view for two positions of the spacecraft in the special case in which the sun and spacecraft lie in the equatorial plane.

where

i spacecraft inclination

ω spacecraft argument of the periapsis

Ω spacecraft longitude of ascending node

$\nu(0)$ initial true anomaly of moon

These choices yield 342 distinct cases. Each case is examined over eleven orbits of the spacecraft as follows: Each spacecraft orbit is divided into one hundred positions such that the time interval between successive positions is constant (approximately fifteen minutes). Each position is then examined for moon availability. The number of positions of the spacecraft which yield moon availability is then called the number of sightings for that orbit.

The minimum number of Phobos sightings over the initial true anomaly of Phobos, $\nu(0)$, is given in Table V. The data is presented as a function of i, ω, and Ω. That is, for each triad of i, ω, and Ω the minimum number of sightings over $\nu(0)$ is given. Eleven spacecraft orbits were used.

From Table V it is noted that the availability of Phobos has a tendency to decrease with increasing inclination. Table VI has been prepared in a manner similar to Table V for the availability of Deimos.

Table VII gives the number of Phobos sightings over 88 spacecraft orbits ($\doteq$ 90 days) for those cases which yield the fewer number of sightings from Table V.

In obtaining these tables, it is assumed the spacecraft is at the periapsis of the first orbit on 0^h of 6 March 1974. The direction of the sun at this time with respect to the Martian coordinate system is

$$\hat{s} = .220\ \hat{i}_3 - .731\ \hat{j}_3 + .646\ \hat{k}_3.$$

The direction of the sun then varies as time progresses. The sun is considered a point source.

Other instrument fields of view and other minimum bright source shield angles (the angle defined in assumption (3)) were run, but these cases give either marginally acceptable Phobos detectability or, imply an instrument of unacceptably large dimensions.

The general conclusion from Tables V, VI, and VII is that over a small number of orbits (11) the number of Phobos sightings may well be too few to determine its orbit. However, only three cases (3, 5, and 6 detections) yield a marginal number of Phobos sightings over eighty-eight orbits of the spacecraft. Except for eight cases (Table VI), the number of Deimos detections is adequate.

The range of instrument magnitude, distance, and subtended angle is given in Table VIII. The method used to calculate the magnitude is given in Appendix C.

TABLE V

MINIMUM NUMBER OF PHOBOS SIGHTINGS OVER $\nu(0)$ AS A FUNCTION OF SPACECRAFT ORBITAL ELEMENTS (11 ORBITS)

$i = 0$

$\Omega + \omega$	0°	60°	120°	180°	240°	300°
	5	6	21	6	6	10

$i = 30^\circ$

Ω \ ω	0°	60°	120°	180°	240°	300°
0°	5	6	7	5	5	9
60°	8	4	3	3	6	5
120°	3	3	1	4	4	10
180°	4	6	6	2	5	6
240°	2	6	5	7	6	3
300°	4	1	5	4	2	1

$i = 60^\circ$

Ω \ ω	0°	60°	120°	180°	240°	300°
0°	4	5	4	6	14	1
60°	3	4	4	5	2	8
120°	3	3	3	2	0	3
180°	3	4	7	1	3	3
240°	1	3	3	2	4	3
300°	4	2	5	4	7	1

$i = 90^\circ$

Ω \ ω	0°	60°	120°	180°	240°	300°
0°	1	5	2	2	4	2
60°	2	2	3	0	2	4
120°	3	0	2	1	0	5
180°	2	1	7	1	2	3
240°	0	4	3	1	5	2
300°	1	2	2	2	4	0

TABLE VI

MINIMUM NUMBER OF DEIMOS SIGHTINGS OVER $\nu(0)$ AS A FUNCTION OF SPACECRAFT ORBITAL ELEMENTS (11 ORBITS)

$i = 0$

$\Omega + \omega$	0°	60°	120°	180°	240°	300°
	57	81	79	85	45	40

$i = 30^\circ$

Ω \ ω	0°	60°	120°	180°	240°	300°
0°	23	23	36	59	79	41
60°	29	28	19	20	38	76
120°	71	13	16	17	48	45
180°	27	21	16	36	57	119
240°	32	21	22	44	109	55
300°	17	14	10	42	41	48

$i = 60^\circ$

Ω \ ω	0°	60°	120°	180°	240°	300°
0°	18	17	26	23	70	146
60°	16	17	14	25	117	46
120°	59	6	8	18	68	64
180°	21	21	15	35	51	56
240°	27	17	16	22	53	57
300°	12	8	4	28	59	70

$i = 90^\circ$

Ω \ ω	0°	60°	120°	180°	240°	300°
0°	40	16	19	21	43	50
60°	25	16	10	30	54	45
120°	60	4	7	19	59	58
180°	23	23	17	38	46	49
240°	29	15	19	19	49	63
300°	17	5	5	59	65	57

TABLE VII

CASES OF MINIMUM PHOBOS SIGHTINGS
EXTENDED TO 88 SPACECRAFT ORBITS

Spacecraft Orbital Elements				Number of Phobos Sightings	
i	ω	Ω	ν (0)	11 Orbits	88 Orbits
30°	60°	300°	60°	1	26
	120°	120°	120°	1	27
	300°	300°	60°	1	17
60°	0°	240°	0°	1	11
	180°	180°	0°	1	5
	240°	120°	0°	0	11
	300°	0°	60°	1	15
90°	0°	240°	0°	0	14
	60°	120°	0°	0	25
	180°	60°	0°	0	13
	240°	120°	0°	0	6
	300°	300°	0°	0	3

TABLE VIII

RANGE OF MAGNITUDE, DISTANCE, AND SUBTENDED ANGLE
OVER ALL STUDIED CASES FOR DETECTABILITY OCCURRED

	Phobos		Deimos	
	Maximum	Minimum	Maximum	Minimum
Magnitude	- 6.81	-3.06	-3.29	0.77
Distance (km)	10,873	1,707	41,929	9,470
Subtended Angle (minutes of arc)	32.4	4.7	2.9	0.7

THE NAVIGATION PROBLEM

Introduction

The problem is to obtain the time-path of the spacecraft and moons, and the harmonic coefficients of the Martian potential by sightings of the moons from the spacecraft. The measured quantity is thus the parallax of the moons as viewed from the spacecraft. It is intuitively evident that this parallax is a function of the trajectories of the spacecraft and the observed moons; these trajectories are in turn functions of the potential. It is not obvious that the problem can be inverted, i.e., the trajectories determined from the measured parallax. It turns out that this is the case, at least if a sufficient time interval is allowed for the moon sightings.

As before, let

$\bar{R}$ = position vector of the spacecraft

$\bar{R}_i$ = position vector of the ith moon, (1, 2) corresponds to (Phobos, Deimos)

the origin of these vectors being the center of mass of Mars, then

$$\hat{d}_i(t) = \frac{\bar{R}_i(t) - \bar{R}(t)}{|\bar{R}_i(t) - \bar{R}(t)|} \qquad \text{(figure 11)} \qquad (9)$$

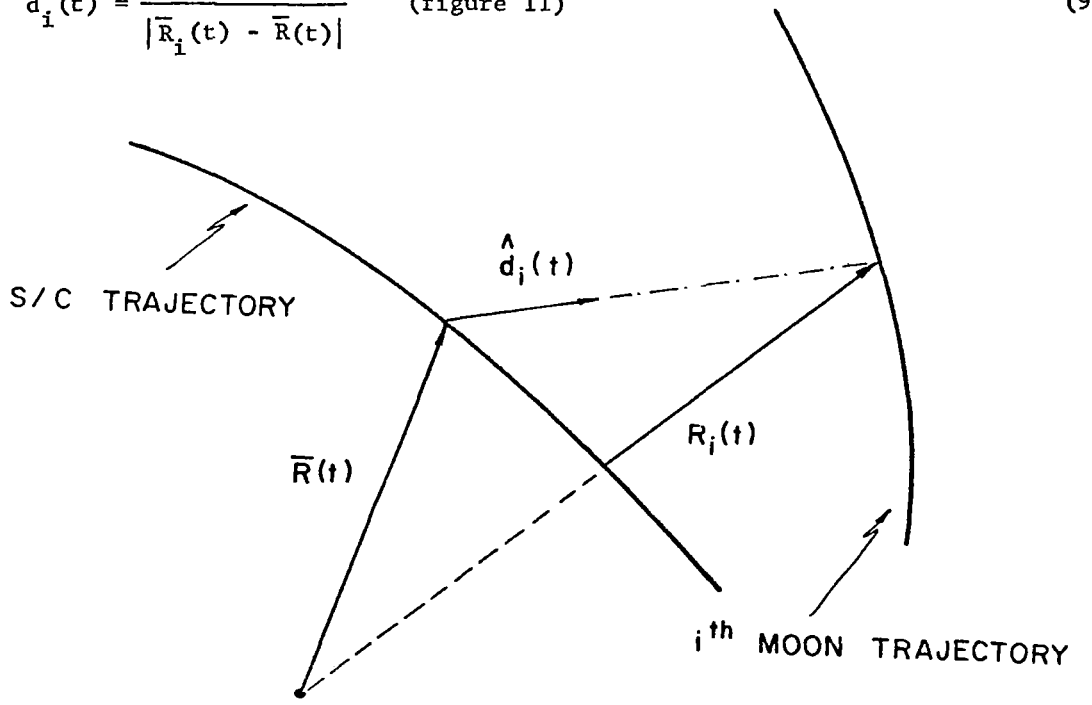

Figure 11: The measured direction $\hat{d}_i(t)$.

is the direction of the moon as viewed from the spacecraft.

If $\hat{d}_i(t)$ were measured at any number of values of t, this information alone is insufficient to determine $\bar{R}(t)$ and $\bar{R}_i(t)$. Each measurement simply yields two independent equations in six unknowns. Moreover, these unknowns change at each measurement. More information, however, is available in that the equations of motion must be satisfied by $\bar{R}(t)$ and $\bar{R}_i(t)$. Thus,

$$\ddot{\bar{R}}(t) = \bar{F}\ (\bar{R}(t)) \tag{10}$$

Here, it will be assumed that the right-hand of equation (10) is derivable from a potential. In order to simplify the expression for the potential, a coordinate system with one axis parallel to the direction of the Martian North Pole is chosen to resolve the position vectors.

Let S_1 be the "celestial" coordinate system with associated unit vectors $\hat{i}_1$, $\hat{j}_1$, and $\hat{k}_1$. The direction $\hat{i}_1$ is from the sun's center to the First Point of Aries, and $\hat{k}_1$ is normal to the earth's equatorial plane. Also, let S_3 be the "Martian" system whose orientation is defined with respect to S_1 by two angles, ξ_1 and ξ_2. That is,

$\hat{i}_1 \rightarrow \hat{i}_2$ rotation $\xi_1 + 90^0$ about $\hat{k}_1 = \hat{k}_2$

$\hat{k}_2 \rightarrow \hat{k}_3$ rotation ξ_2 about $\hat{i}_2 = \hat{i}_3$

where

ξ_1 the assumed right ascension of the Martian North Pole = 317.9^o

ξ_2 the assumed co-declination of this point = 35.3^o.

The origin of S_3 is the center of mass of Mars. The equations of motion (10) will be written with components in S_3. The orientation of S_1 with respect to S_3 is given by

$$\begin{pmatrix} \hat{i}_1 \\ \hat{j}_1 \\ \hat{k}_1 \end{pmatrix} = A \begin{pmatrix} \hat{i}_3 \\ \hat{j}_3 \\ \hat{k}_3 \end{pmatrix}$$

where

$$A = \begin{pmatrix} -\sin\xi_1 & -\cos\xi_1\cos\xi_2 & \cos\xi_1\sin\xi_2 \\ \cos\xi_1 & -\sin\xi_1\cos\xi_2 & \sin\xi_1\sin\xi_2 \\ 0 & \sin\xi_2 & \cos\xi_2 \end{pmatrix} \tag{11}$$

The Martian potential, at any generic point, chosen here is written

$$V(r, \phi, \theta) = -\frac{\mu}{r}\left[1 + \sum_{n=2}^{5}\sum_{m=0}^{n}\left(\frac{r_e}{r}\right)^n P_n^m(\cos\phi) \times \left(C_{nm}\cos(m\theta + \dot{\lambda}t) + S_{nm}\sin(m\theta + \dot{\lambda}t)\right)\right] \quad (12)$$

where

$\mu = M G = 5.5429 \times 10^{11}$ km^3/hr^2

r_e equatorial radius of Mars = 3388 km

r distance of point from center of mass of Mars

ϕ co-elevation of point with respect to S_3

θ azimuth of point with respect to S_3

$\dot{\lambda}$ rate of rotation of Mars about $\hat{k}_3$

P_k^j associated Legendre function of the first kind of degree k and order j.

The right-hand side of (10) is thus $\overline{F} = -\nabla V$.

Methods of using the constraints provided by equation (9) to yield estimates of the initial conditions and parameters C_{nm}, S_{nm} in equation (12) are well known and will not be considered. However, the effect of errors in measuring $\hat{d}$ upon the outputs will be considered.

Error Analysis

Two spacecraft orbits defined in Table IX are chosen for study. These particular orbits were chosen because of their relatively poor yield of Phobos sightings.

TABLE IX

ORBITS TO BE STUDIED

Spacecraft				Phobos				Deimos			
Orbit No.	ω	i	Ω	ν_o	t_1(hrs)	t_n(hrs)	n	ν_o	t_1(hrs)	t_n(hrs)	n
1	0^o	60^o	240^o	0^o	1034.0	2117.1	11	0^o	101.67	2154.31	146
2	300^o	30^o	300^o	60^o	197.7	2143.0	13	60^o	245.0	2092.0	154

In the table, ω, i, and Ω are the initial orbital elements (t = 0) and are defined with respect to S_3; ν_o is the initial moon true anomaly; t_1 and t_n are, respectively, the times of the first and last moon sighting, and n is the number of moon sightings.

To investigate the effect of random errors in the measurement of the direction to the moons at each sighting, the following major assumptions were made:

(1) The only forces upon the spacecraft and the moons are derivable from the potential shown in equation (12).

(2) No systematic error exists in the measured direction. However, deterministic errors in some of the parameters of the potential shown in equation (12) are allowed.

(3) The error distributions of each measured angle are independent and identical and

$$\sigma\left(\delta\ e_3\right) = \cos e_3\ \sigma\left(\delta\ a_3\right) = 1 \text{ arc minute.}$$

The errors in the measured elevation and azimuth of the direction to the moon are $\delta\ e_3$ and $\delta\ a_3$, respectively, these angles being measured with respect to the Martian system, S_3.

(4) The random input errors are so small that each output error is a linear combination of the input errors.

The accuracy of the direction measurement is open to question. In fact, for the proposed instrument, this accuracy is not constant. As will be shown, it is a strong function of the particular stellar background against which the moon is viewed and the moon's position within the instrument's field of view. A different instrument (or the same basic instrument with a different slit configuration and field of view) would possess a different direction accuracy. To account approximately for this effect, the output error may then be scaled. On the average, the designed instrument for this study has a direction accuracy of five minutes of arc. Hence, the errors to be shown may be multiplied by five to account more nearly for our particular instrument.

A problem containing twenty three unknowns was first examined. These unknowns are as follows: the initial position and velocity of the three bodies, and the five harmonic coefficients (C_{20}, C_{30}, C_{40}. C_{21}, and S_{21}). The initial position and velocity for the three bodies are defined as follows: Let

t_1 = time at which Phobos is first sighted

τ_1 = time at which Deimos is first sighted.

Then, the initial positions are

$\bar{R}(t_1)$, $\bar{R}_1(t_1)$, $\bar{R}_2(\tau_1)$ if $t_1 \leq \tau_1$

$\bar{R}(\tau_1)$, $\bar{R}_1(t_1)$, $\bar{R}_2(\tau_1)$ if $t_1 > \tau_1$.

A corresponding definition is used for initial velocity.

Values assigned to the five harmonic coefficients so that a simulated "measured direction" is computable are:

$$C_{20} = -2.011 \times 10^{-3}$$

$$C_{30} = C_{40} = 10^{-6}$$

$$C_{21} = 2 \times 10^{-5}$$

$$S_{21} = 10^{-5}$$

Only C_{20} is given a numerical value in the literature. This value is obtained by Earth-based observation of the moons. The values given for C_{30} and C_{40} are simply a guess. Values of C_{21} and S_{21} were computed by assuming Mars has an axis of dynamic symmetry, but this axis is not parallel to $\hat{k}_3$. We assume the true right ascension and co-declination of the axis of symmetry differ from ξ_1 and ξ_2 by one minute of arc.

Results

Although not shown, the results of the problem containing twenty-three unknowns were somewhat disappointing in that the errors incurred in the higher harmonic coefficients, C_{30} and C_{40} are generally greater than the assigned values. This occurs because of the relatively high altitude of the three bodies. It is concluded then that C_{30} and C_{40} should not be treated as unknowns. It should be emphasized, however, that the inability to obtain these quantities results not from a defect in the measurement, but from the choice of spacecraft orbit. In all examples to be considered, C_{30} and C_{40} will be assumed known. The two cases for which numerical results are shown contain twenty-one unknowns.

Figures 12 and 13 are plots of the errors in initial position and speed of the spacecraft, Deimos and Phobos as a function of the sighting time interval during orbit number 1 (Table IX). Also shown in figure 12 are the number of sightings of the two moons at various times. Position and speed errors are defined, respectively, as follows:

$$\sqrt{\sigma^2(r) + \sigma^2(s) + \sigma^2(z)} \quad , \quad \sqrt{\sigma^2(\dot{r}) + \sigma^2(\dot{s}) + \sigma^2(\dot{z})}$$

where

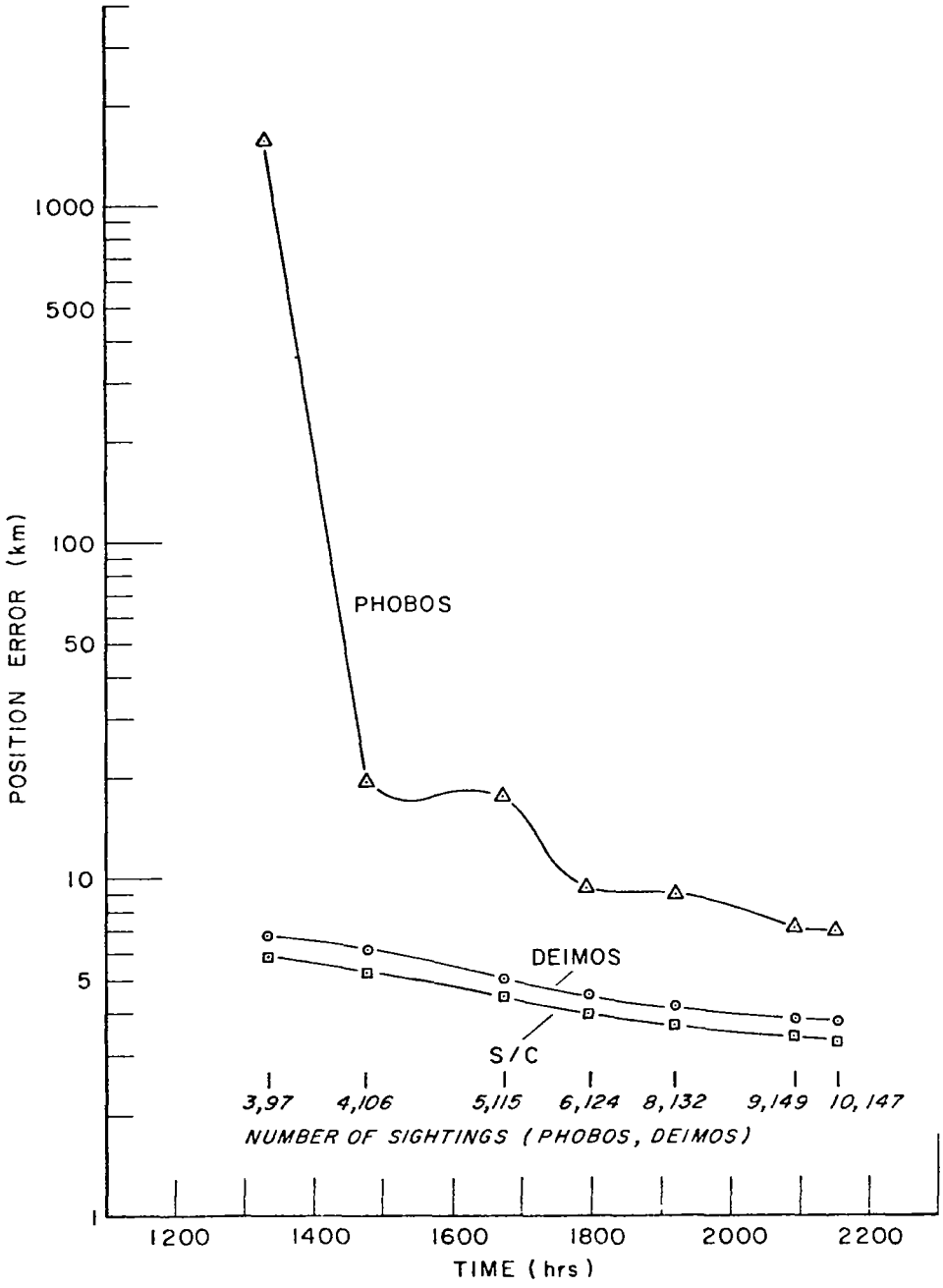

Figure 12: Error in initial position of the three bodies as a function of sighting time interval. Orbit No. 1.

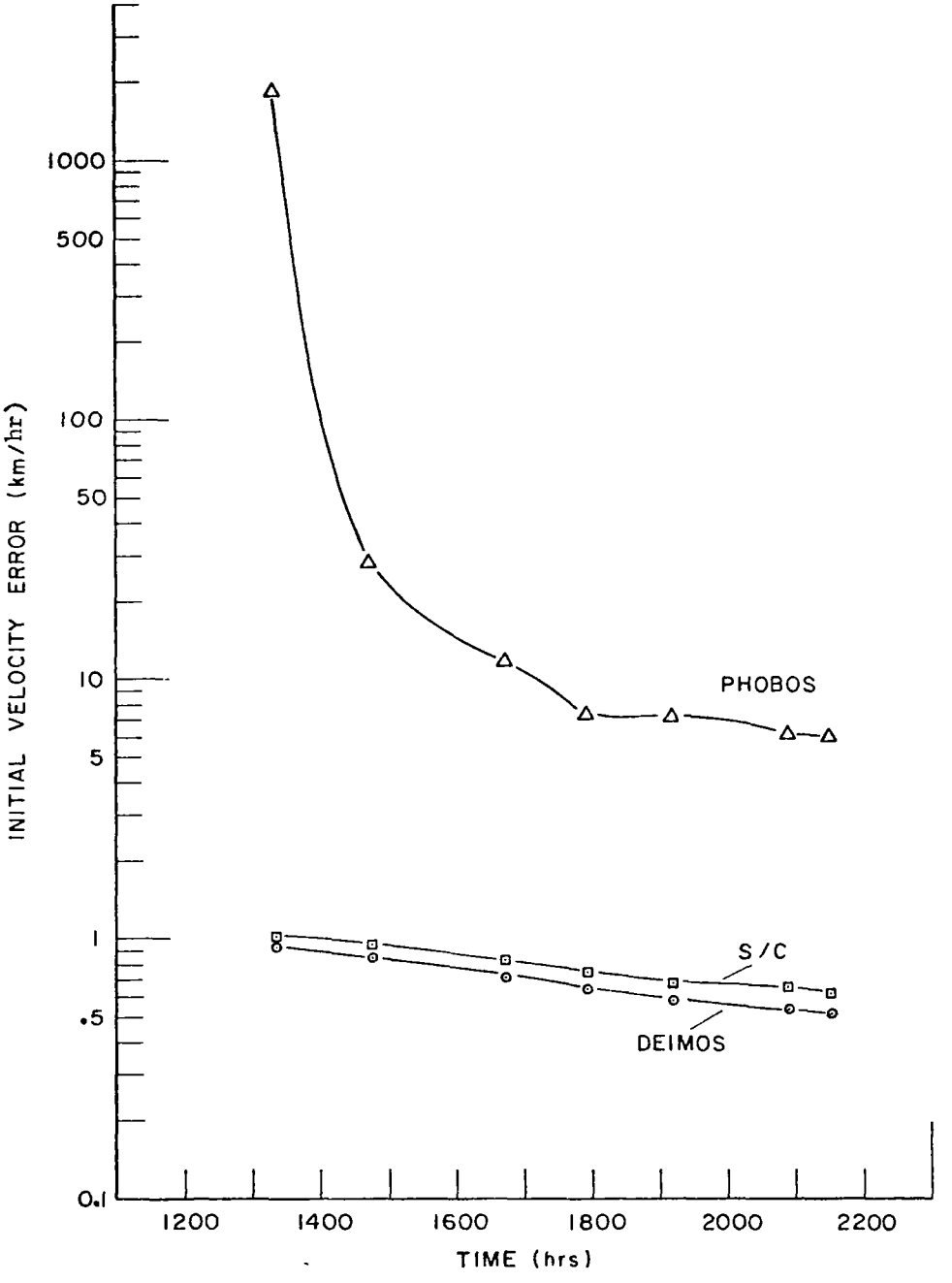

Figure 13: Error in initial speed of the three bodies as a function of the sighting time interval. Orbit No. 1. 43

σ (r) standard deviation of initial radial position error

σ (s) standard deviation of initial along-track position error

σ (z) standard deviation of initial cross-track position error.

In the figures, the errors are shown as continuous. This is an approximation for the errors change discontinuously as each new measurement is taken and the error functions are descending staircase functions.

Initially, the position errors of Phobos are two orders of magnitude greater than those of the spacecraft and Deimos. However, as more sightings of Phobos are taken, the position errors of Phobos are reduced so that after 2100 hours ($\approx$ 85 spacecraft orbits) the errors are more comparable.

The initial speed errors of the three bodies are greatest for Phobos and smallest for Deimos. This order is the same as the true initial speeds which are as follows:

Phobos	7.570×10^3 km/hr
Spacecraft	5.101×10^3 km/hr
Deimos	4.857×10^3 km/hr.

Figure 14 is a plot of the normalized error in the three harmonics coefficients which are treated as unknowns in the total problem. Here normalized error of C_{20} is defined as

$$\tilde{C}_{20} = \sigma\left(\delta C_{20}\right)/|C_{20}| \ .$$

Similar definitions are used for $\tilde{S}_{21}$ and $\tilde{C}_{21}$.

All three harmonics are quite well determined by the measurements. Figures 15, 16, and 17 are the same format as figures 12, 13, and 14, respectively, except the latter figures are derived from orbit number 2. This orbit not only yields more Phobos sightings (15 versus 10) and total moon sightings (167 versus 157), but also produces a better viewing geometry. As a result, all errors are reduced from those produced by orbit number 1 by approximately a factor of two.

Effect of Errors in Assumed Known Parameters

In addition to random errors, errors will be present in the harmonic coefficient which are not treated as unknowns but are assumed known. These latter errors are deterministic.

In reducing the measurements, it was assumed that the mass of Mars was known, and all harmonic coefficients other than C_{20}, C_{21}, and S_{21} were zero.

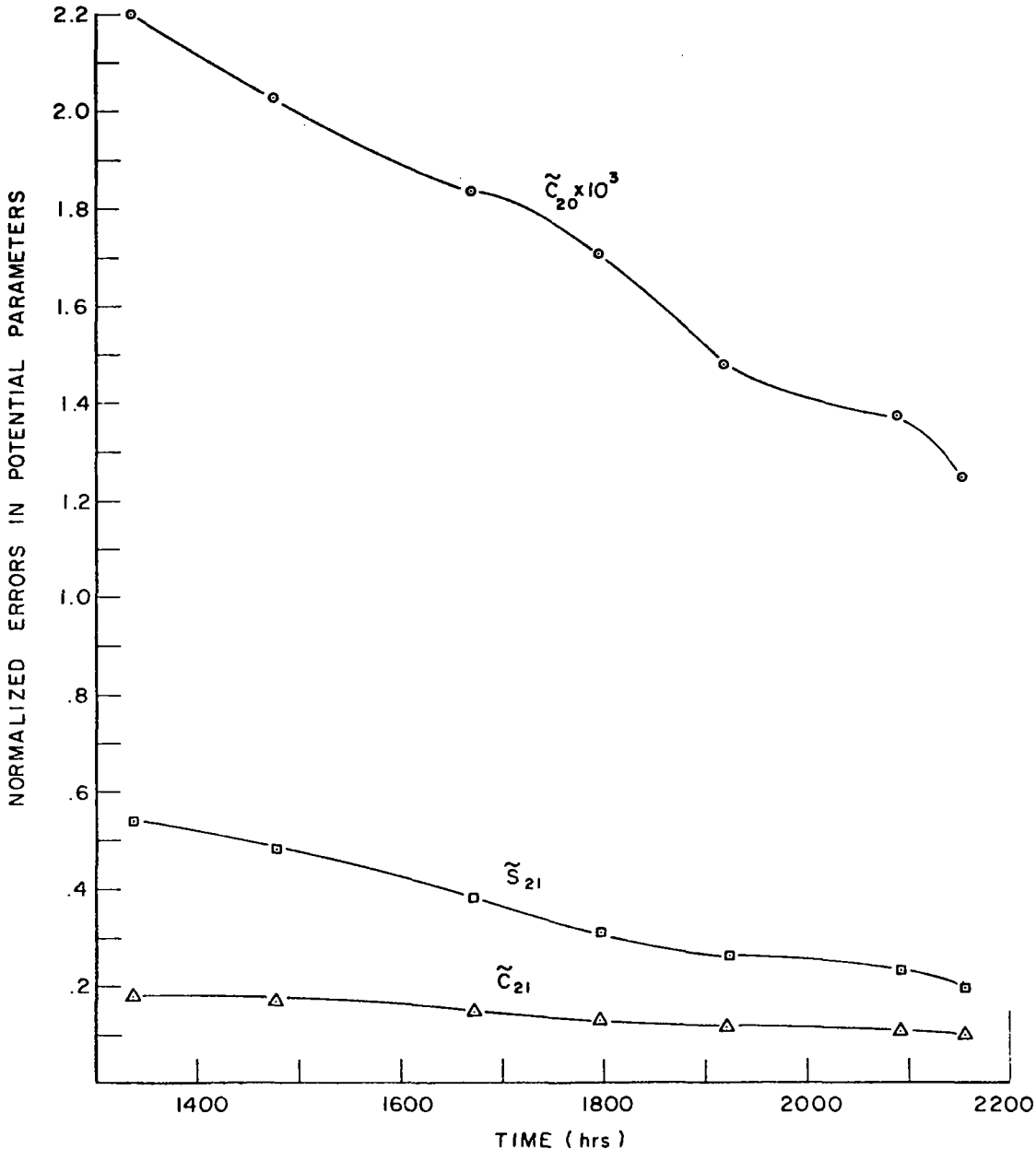

Figure 14: Normalized error in the harmonic coefficients as a function of sighting interval. Orbit No. 1.

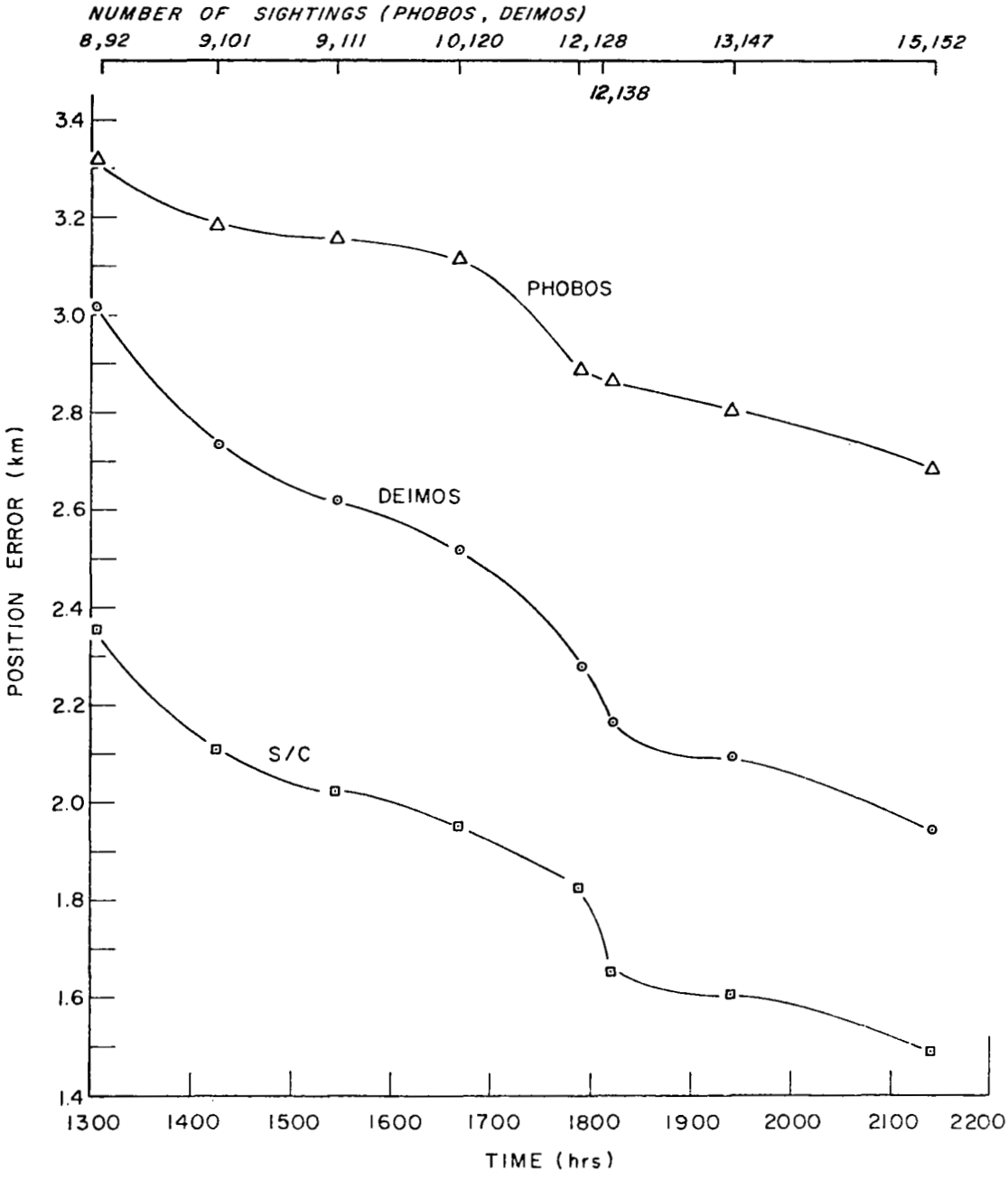

Figure 15: Initial error in position of the three bodies as a function of sighting time interval. Orbit No. 2.

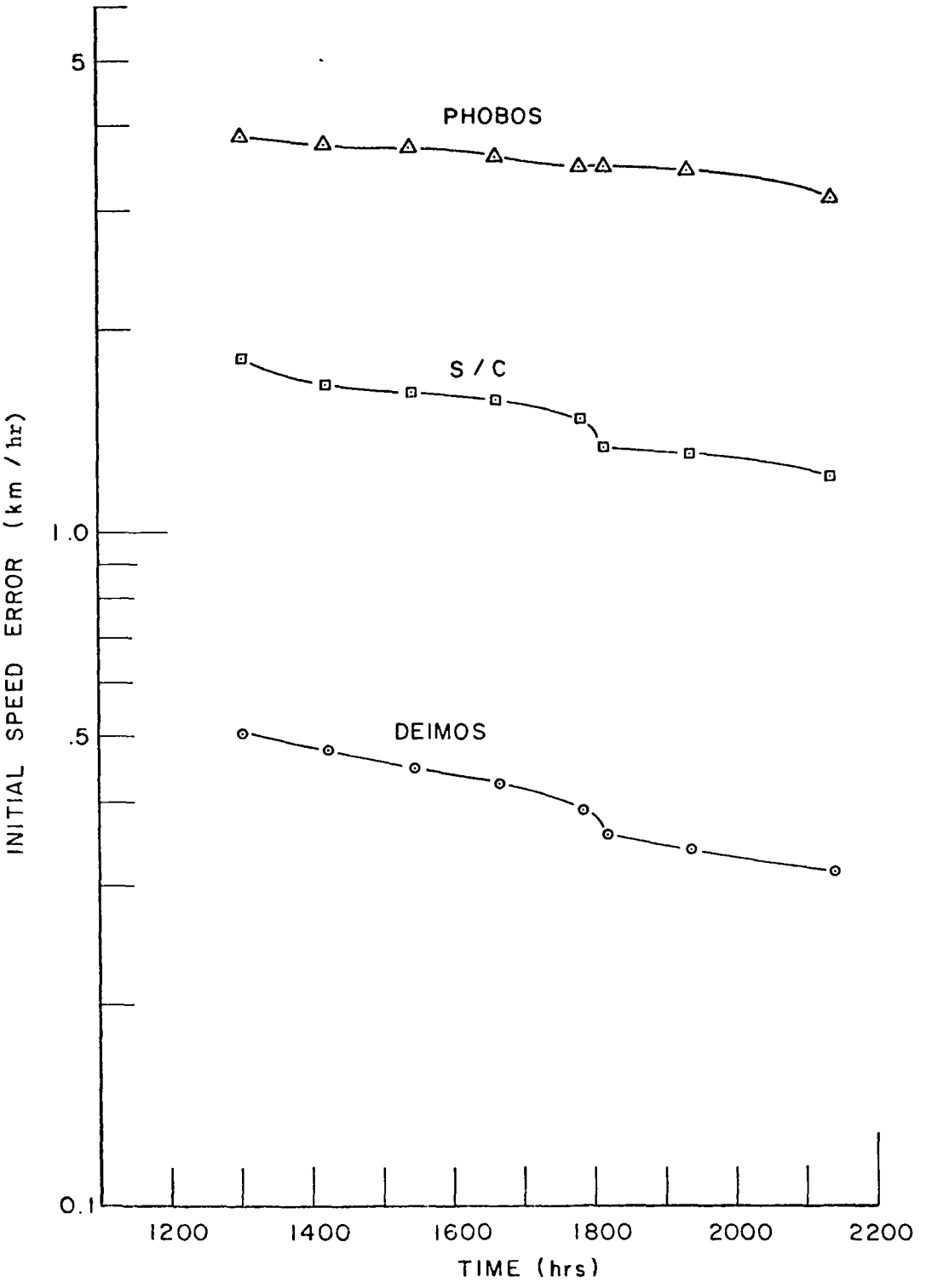

Figure 16: Error in initial speed of the three bodies. Orbit No. 2.

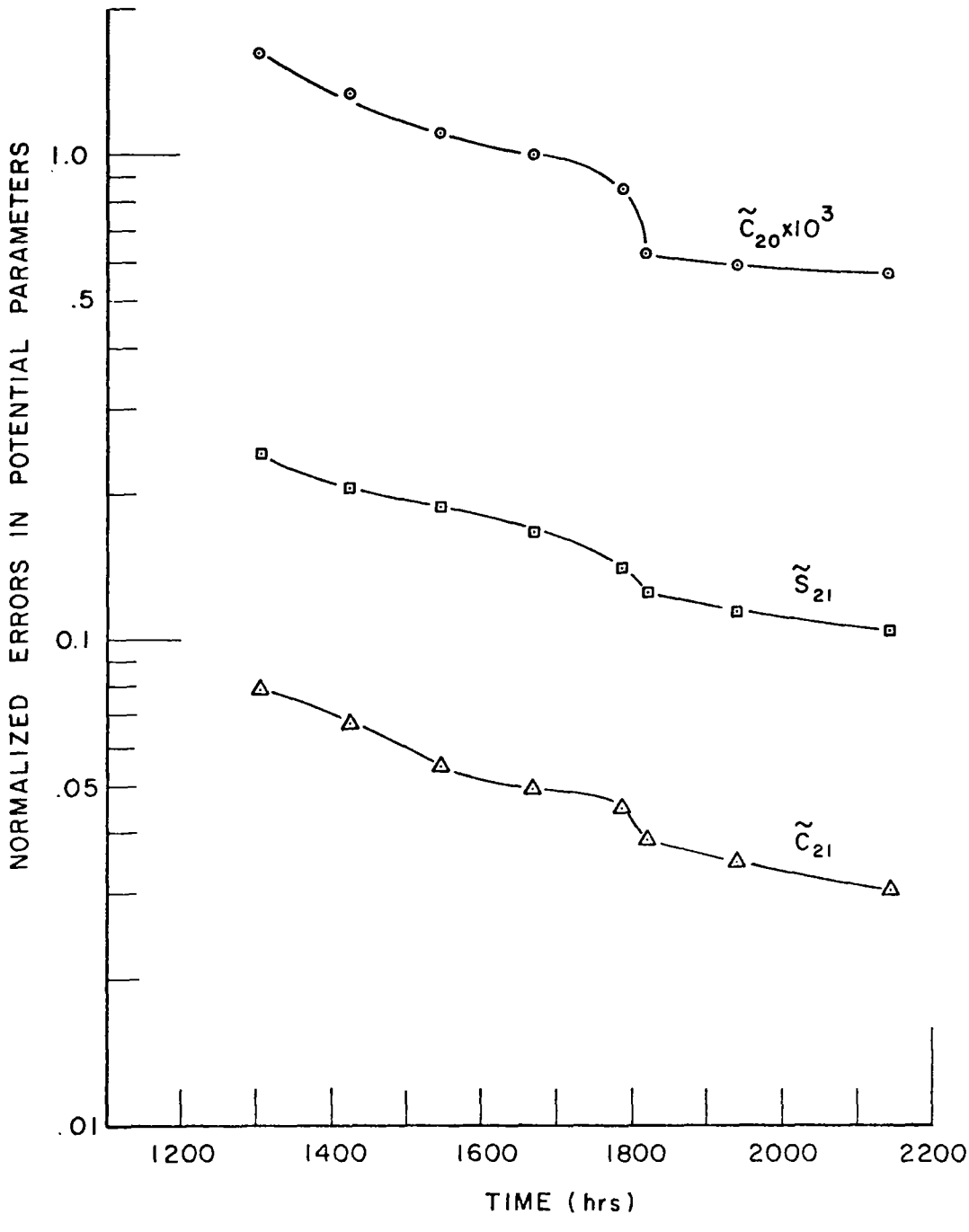

Figure 17: Normalized error in the harmonic coefficients as a function of sighting interval. Orbit No. 2.

Now suppose this were not true, but δ M/M = δ C_{30} = δ C_{40} = δ C_{31} = δ S_{31} = 10^{-6}. These input errors will then induce errors in the unknowns. Results are shown in Tables X and XI. These tables are derived from orbit number 1, but orbit number 2 yields results quite similar. Again, the units of position and speed errors are km and km/hr, respectively.

Three salient results are obtained from these tables.

(1) The resulting errors are small. However, if the inputs δ C_{31}, and δ S_{31} were increased by a factor of ten, then significantly large errors in most outputs would result and thus C_{31} and S_{31} should be chosen as unknowns and solved for.

(2) In contrast to the effect of random input errors, the effect of the deterministic errors is to sometimes increase and sometimes decrease the errors of the unknowns as more sightings are used.

(3) The error in the mass of Mars produces a negligible error in all unknowns and these errors are almost independent of the number of sightings used.

The result (3) has an analytic explanation. The equations of motion of the three bodies are of the form

$$\ddot{\bar{R}} = -\frac{G M \bar{R}}{|\bar{R}|^3} + \bar{g}(\bar{R})$$

where $\bar{g}(\bar{R})$ is small. Suppose a change of scale is made in length and mass so that

$$\bar{r} = \lambda \bar{R}$$

$$m = \lambda^3 M$$

where λ is a constant. Since no lengths are measured, λ will not appear in the constraint equations (9) if these equations are expressed in the new variables. In terms of the new variables, the equations of motion become

$$\ddot{\bar{r}} = -\frac{G m \bar{r}}{|\bar{r}|^3} + \bar{g}(\lambda \bar{r}) .$$

Thus, for small $\bar{g}$ the total system is nearly independent of λ. Let

$$\lambda = 1 + \frac{1}{3}\frac{\delta M}{M} ,$$

then

TABLE X

ERRORS IN UNKNOWNS PRODUCED BY DETERMINISTIC ERRORS IN FIVE GIVEN PARAMETERS. ORBIT NO. 1, 100 MOON SIGHTINGS

Erroneous Input	Deimos		Phobos		Spacecraft		Harmonic Coefficient		
	Position	Speed	Position	Speed	Position	Speed	$\tilde{C}_{20}$	$\tilde{C}_{21}$	$\tilde{S}_{21}$
$\delta M/M$	7.8×10^{-3}	1.6×10^{-3}	3.2×10^{-3}	2.5×10^{-3}	6.9×10^{-3}	1.7×10^{-3}	3.3×10^{-7}	6.7×10^{-6}	3.4×10^{-6}
δC_{30}	9.2×10^{-3}	1.4×10^{-3}	1.6	1.9	1.3×10^{-2}	3.6×10^{-3}	9.9×10^{-6}	7.1×10^{-3}	6.4×10^{-3}
δC_{40}	1.3×10^{-3}	2.8×10^{-4}	4.2×10^{-1}	4.8×10^{-1}	2.2×10^{-3}	5.1×10^{-4}	1.2×10^{-5}	6.8×10^{-2}	5.0×10^{-2}
δC_{31}	1.2×10^{-1}	1.7×10^{-2}	18	20	1.8×10^{-1}	4.3×10^{-2}	2.9×10^{-4}	1.7×10^{-2}	9.5×10^{-2}
δS_{31}	8.4×10^{-2}	1.3×10^{-2}	13	15	1.1×10^{-1}	3.3×10^{-2}	2.4×10^{-4}	1.2×10^{-1}	1.5×10^{-1}

TABLE XI

ERRORS IN UNKNOWNS PRODUCED BY DETERMINISTIC ERRORS IN FIVE GIVEN PARAMETERS. ORBIT NO. 1, 157 MOON SIGHTINGS

Erroneous Input	Deimos		Phobos		Spacecraft		Harmonic Coefficient		
	Position	Speed	Position	Speed	Position	Speed	$\tilde{C}_{20}$	$\tilde{C}_{21}$	$\tilde{S}_{21}$
$\delta M/M$				Same as Table X					
δC_{30}	1.9×10^{-2}	2.0×10^{-3}	2.1×10^{-2}	1.3×10^{-2}	2.8×10^{-2}	4.7×10^{-3}	1.3×10^{-5}	1.1×10^{-2}	1.0×10^{-3}
δC_{40}	8.0×10^{-3}	1.3×10^{-3}	1.2×10^{-2}	5.0×10^{-3}	5.4×10^{-3}	1.4×10^{-3}	1.0×10^{-5}	6.3×10^{-2}	1.0×10^{-2}
δC_{31}	2.1×10^{-1}	2.4×10^{-2}	2.8×10^{-1}	1.5×10^{-1}	3.5×10^{-1}	4.5×10^{-2}	3.9×10^{-4}	1.0×10^{-1}	5.1×10^{-2}
δS_{31}	1.9×10^{-1}	2.1×10^{-2}	2.9×10^{-1}	1.6×10^{-1}	2.8×10^{-1}	4.4×10^{-2}	1.8×10^{-4}	1.9×10^{-1}	5.8×10^{-2}

$$\bar{r} = \bar{R} + \frac{1}{3}\frac{\delta M}{M}\bar{R}$$

$$m \approx M + \delta M.$$

So, for

$$\delta M/M = 10^{-6},\ \delta \bar{r} = \bar{r} - \bar{R} \approx \frac{1}{3} 10^{-6} \bar{R} .$$

Thus, a small change in the mass of Mars can be expected to cause an error in the computed position which is almost entirely in the radial direction. In Table XII a comparison is given between results obtained from this analysis and the previous error analysis. Again, the unit of length is km.

TABLE XII

COMPARISON OF INITIAL POSITION ERRORS PREDICTED FROM SIMPLIFIED ANALYSIS AND ERRORS OBTAINED FROM NUMERICAL ERROR ANALYSIS

	$\delta \bar{r} = (\delta M/3M) \bar{R}$			Error Analysis		
Component of Error	Phobos	Deimos	S/C	Phobos	Deimos	S/C
Radial	3.1×10^{-3}	8.0×10^{-3}	7.3×10^{-3}	3.2×10^{-3}	7.8×10^{-3}	6.9×10^{-3}
Along-track	0	0	0	4×10^{-8}	3×10^{-8}	-9×10^{-8}
Across-track	0	0	0	-3×10^{-8}	3×10^{-8}	4×10^{-8}

SPACECRAFT ATTITUDE

Introduction

In the previous section it was assumed that the direction to a moon was measured. This cannot be done without first determining the attitude of the spacecraft from transits of stellar targets. This latter problem is now considered.

Analysis

The general problem is to find the orientation of a coordinate system fixed in the spacecraft with respect to a stationary coordinate system. The basic input measurements which yield this orientation, or attitude, are the readout of an angle encoder at the instant known stars cross each of three slits.

Consider a transparent slit etched on an otherwise opaque focal plane of an optical system as shown in figure 18. If the slit is a straight line segment and the optical system is free of distortion, then a portion of a plane will be defined which contains the slit and the nodal point of the lens system. Given a distant bright point source, this source will be sensed by a detector behind the slit if, and only if, it lies on the plane defined by the slit and optical system. If a point source crosses the plane, the source image transits the slit. The encoder readout at the instant the point source lies in the plane is called the transit angle.

For any transit of a star, the following equation may be written

$$\hat{n}\ (\theta,\ t) \cdot \hat{s} = 0 \tag{13}$$

where

$\hat{n}$ unit vector normal to the slit plane at the instant of transit,

$\hat{s}$ unit vector in the direction of star, and

θ angle encoder reading at transit time t.

To specify the vehicle orientation at any specific instant requires three independent angles while equation (13) yields only one condition. Additional equations are obtained as the instrument motion causes the sensor to scan the celestial sphere and other stars are encountered. This results in a set of conditions

$$\hat{n}\ (\theta_i,\ t_i) \cdot \hat{s}_i = 0\ . \tag{14}$$

If no further information is introduced, this simply adds one equation and three unknown angles at each isolated transit time. However, the physics which governs the motion of the satellite may be invoked to develop a time-dependent

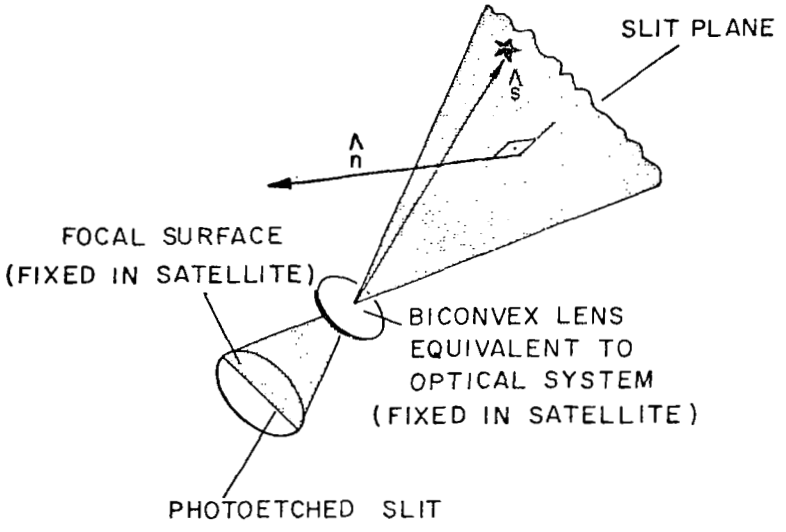

Figure 18: The relationship between the slit plane and the target star at the instant of transit.

characterization of the attitude which involves just a few unknown parameters. This "attitude model" may then be used to internally couple the condition in equation (14).

Observe that since the optical system has its position defined with respect to the satellite via the encoder, the components of $\hat{n}$ are most easily written in a coordinate system fixed in the satellite. On the other hand, $\hat{s}$ is most easily written in a celestial coordinate system (a system in which the star directions are cataloged). In order that these vectors may be written in the same coordinate system, parameters which specify the orientation of the coordinate system fixed in the satellite with respect to the celestial system must be introduced. However, these are precisely the unknown attitude model parameters which are to be determined. Solution for these parameters yields a state vector which, when inserted in the attitude model, results in a time history of the attitude over the interval spanned by the transit data.

Two additional observations may be made. First, each stellar target will yield two spatially independent measurements -- e.g., azimuth and elevation -- if more than one slit is employed in the sensor. The set of basic constraint equations then takes the form

$$\hat{n}_j (\theta_i, t_i) \cdot \hat{s}_i = 0 \qquad (15)$$

where j indexes the set of slits. The additional information per star which is gained from a multi-slit system may be exploited to reduce the number of required stellar targets or to increase the data sampling rate. Second, if the number of independent conditions in equation (15) exceeds the dimensionality of the state vector, then this set of equations is redundant and may be solved in a least-squares sense. The internal consistency of the resulting solution is a measure jointly of the adequacy of the attitude model and the accuracy of the transit angles.

In order to write equation (15) in more detail, let several coordinate systems, S_i, with associated unit vectors $\hat{i}_i$, $\hat{j}_i$, $\hat{k}_i$ be defined as follows:

S_1 Celestial coordinate system; $\hat{i}_1$ direction of the First Point of Aries, $\hat{k}_1$, in direction of the celestial North Pole.

S_5 Sun-Canopus system; $\hat{k}_5$ in the anti-Sun direction, and $\hat{i}_5$ in the Sun-Canopus plane.

S_7 Spacecraft fixed system; $\hat{k}_7$ is the direction of the instrument's spin axis, and $\hat{i}_7$ is the direction determined by the angle encoder zero.

S_8 Instrument fixed system which rotates with respect to S_7 about $\hat{k}_7 = \hat{k}_8$.

S_{10j} System fixed in the jth slit; $\hat{j}_{10j}$ is normal to the jth slit. This system is also fixed in the rotating instrument.

The orientation of S_5 with respect to S_1 is known; S_5 is introduced only to

simplify the description of the spacecraft attitude. It is assumed that the spacecraft has a Sun-Canopus tracking system so that the spacecraft fixed system, S_8, is nearly aligned with S_5.

Now,

$$\begin{pmatrix} \hat{i}_5 \\ \hat{j}_5 \\ \hat{k}_5 \end{pmatrix} = B \begin{pmatrix} \hat{i}_1 \\ \hat{j}_1 \\ \hat{k}_1 \end{pmatrix} \tag{16}$$

where the matrix B is given as follows: The third row of B is composed of the components of a unit vector from the sun to Mars. This vector being resolved in S_1. The first and second rows are then given by

$$Kb_{11} = \cos\delta_c \cos\alpha_c \left(1 - b_{31}\, b_{33}\right) - \left(b_{32} \cos\delta_c \sin\alpha_c + b_{33} \sin\delta_c\right) b_{33}$$

$$Kb_{12} = \cos\delta_c \sin\alpha_c \left(1 - b_{32}\, b_{33}\right) - \left(b_{31} \cos\delta_c \cos\alpha_c + b_{33} \sin\delta_c\right) b_{33}$$

$$Kb_{13} = \sin\delta_c \left(1 - b_{33}^2\right) - \left(b_{31} \cos\alpha_c + b_{32} \sin\alpha_c\right) \cos\delta_c\, b_{33}$$

$$b_{21} = b_{32}\, b_{13} - b_{33}\, b_{12}$$

$$b_{22} = b_{33}\, b_{11} - b_{31}\, b_{13}$$

$$b_{23} = b_{31}\, b_{12} - b_{32}\, b_{11}$$

Here α_c, δ_c are respectively the right ascension and declination of Canopus.

$$K^2 = 1 - \left[\left(b_{31} \cos\alpha_c + b_{32} \sin\alpha_c\right) \cos\delta_c + b_{33} \sin\delta_c\right]^2$$

$$B = \left(b_{ij}\right).$$

Let the orientation of S_8 with respect to S_5 be defined by three angles η_1, η_2, and s so that

$\hat{j}_5 \rightarrow \hat{j}_6$ rotation η_1 about $\hat{i}_5 = \hat{j}_6$

$\hat{i}_6 \rightarrow \hat{i}_7$ rotation η_2 about $\hat{j}_6 = \hat{j}_7$

$\hat{i}_7 \rightarrow \hat{i}_8$ rotation s about $\hat{k}_7 = \hat{k}_8$

Hence

$$\begin{pmatrix} \hat{i}_8 \\ \hat{j}_8 \\ \hat{k}_8 \end{pmatrix} = D\,C \begin{pmatrix} \hat{i}_5 \\ \hat{j}_5 \\ \hat{k}_5 \end{pmatrix} \tag{17}$$

where

$$D = \begin{pmatrix} \cos s & \sin s & 0 \\ -\sin s & \cos s & 0 \\ 0 & 0 & 1 \end{pmatrix}$$

$$C = \begin{pmatrix} \cos \eta_2 & \sin \eta_1 \sin \eta_2 & -\cos \eta_1 \sin \eta_2 \\ 0 & \cos \eta_1 & \sin \eta_1 \\ \sin \eta_2 & -\sin \eta_1 \cos \eta_2 & \cos \eta_1 \cos \eta_2 \end{pmatrix}$$

the angles η_1, η_2, and s are, of course, unknown.

The remaining problem is to describe the orientation of the jth slit system, S_{10j}, with respect to S_8. To this end,

$\hat{k}_8 \rightarrow \hat{k}_9$ rotation σ about $\hat{j}_8 = \hat{j}_9$

$\hat{i}_9 \rightarrow \hat{i}_{10j}$ rotation ρ_j about $\hat{k}_9 = \hat{k}_{10}$, j = 1, 2, 3

Here

$\rho_1 = \epsilon - \Gamma$

$\rho_2 = \epsilon$

$\rho_3 = \epsilon + \Gamma$ (see figure 19).

Thus, the plane defined by the jth slit is the $(\hat{i}_{10j}, \hat{k}_{10})$ plane, and

$$\hat{j}_{10j} = -\sin \rho_j \cos \sigma\, \hat{i}_8 + \cos \rho_j\, \hat{j}_8 + \sin \rho_j \sin \sigma\, \hat{k}_8 . \tag{18}$$

Now, $\hat{j}_{10j}$ is normal to the jth slit plane. In obtaining equation (18), it was

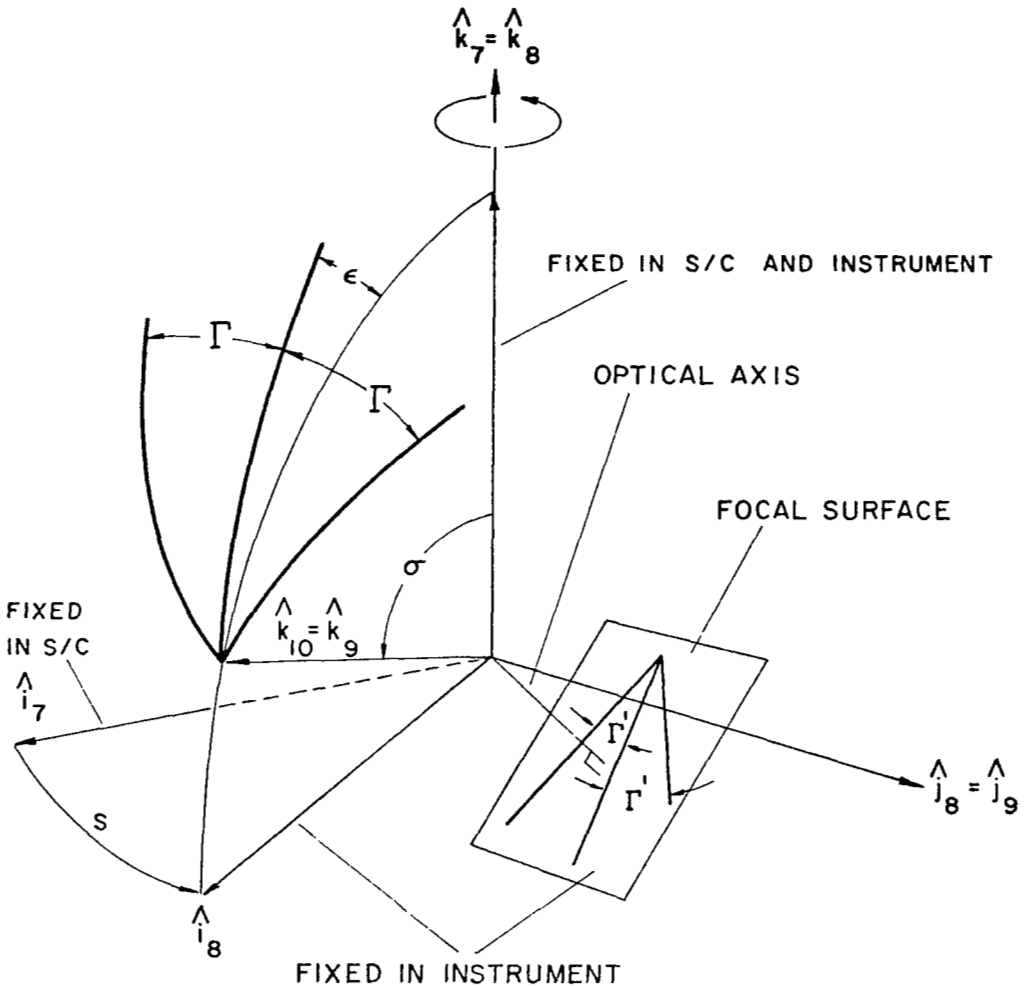

Figure 19: The orientation of the slits as defined by ϵ, Γ, σ.

tacitly assumed that the three slits are designed to intersect at a point so the center slit bisects the angle formed by the outer two slits as shown in figure 19.

The components of the slit plane normal in the coordinate system, S_1, can now be obtained by combining equations (16), (17), and (18). Hence

$$\hat{j}_{10j} = \left(-\sin\rho_j \cos\sigma,\ \cos\rho_j,\ \sin\rho_j \sin\sigma\right) D\ C\ B \begin{pmatrix} \hat{i}_1 \\ \hat{j}_1 \\ \hat{k}_1 \end{pmatrix} .$$

So, equation (13) becomes

$$0 = \left(-\sin\rho_j \cos\sigma,\ \cos\rho_j,\ \sin\rho_j \sin\sigma\right) D(s)\ C\left(\eta_1, \eta_2\right) B\ \hat{s} \qquad (19)$$

where

$\hat{s}$ denote the direction of the star which transits the jth slit, this direction being resolved in S_1.

If the spacecraft were truly stabilized by the Sun-Canopus tracking system, then η_1 and η_2 would be constant angles. Here it will be assumed that these angles can be approximated by linear functions of time during the time interval over which stellar transits are gathered (approximately five minutes). It is thus assumed that

$$\eta_1 = \eta_{10} + \dot{\eta}_1 (t - t_o)$$

$$\eta_2 = \eta_{20} + \dot{\eta}_2 (t - t_o)$$

$$s = s_o + \dot{s} (t - t_o) + \theta$$

where

η_{10}, $\dot{\eta}_1$, η_{20}, $\dot{\eta}_2$ s_o, and $\dot{s}$ are constant

θ is the angle encoder reading

$$\rho_1 = \epsilon - \Gamma$$

$$\rho_2 = \epsilon$$

$$\rho_3 = \epsilon + \Gamma$$

Hence, each transit gives one equation in eight unknowns: three initial attitude angles (η_{10}, η_{20}, s_o), three rates ($\dot{\eta}_1$, $\dot{\eta}_2$, and $\dot{s}$), and two angles

associated with the slit orientation (ϵ, σ). It is assumed that the angle between the slits, Γ, is known.

In general, at least eight transits from two distinct stars are required. At each transit the transit time, t, and the angle, θ, are measured. The direction to the star $\hat{s}$ is determined by use of a star catalog.

Direction to a Moon

After the attitude is determined from the stellar transits, the direction to the moon can be found from the moon transits. This direction must be resolved in the coordinate system, S_3, (the Martian system).

At the instant the moon's center lies in the jth slit, one can write

$$0 = \left(-\sin \rho_j \cos \sigma,\ \cos \rho_j,\ \sin \rho_j,\ \sin \rho_j \sin \sigma\right) D\, C \begin{pmatrix} \cos e_5 \cos a_5 \\ \cos e_5 \sin a_5 \\ \sin e_5 \end{pmatrix}$$

where

e_5, a_5 are the elevation and azimuth, respectively, of the moon's direction with respect to S_5

D, C are known matrices computed by use of the stellar targets. C is a function of the time of moon transit, and D is a function of this time and the angle encoder

σ and ρ_j are known angles also computed by use of the stellar targets.

Hence, the transit of the moon across all three slits yields three equations in the two unknowns, e_5 and a_5. After obtaining these angles, the direction of the moon with respect to S_3 may be found as simply

$$\begin{pmatrix} \cos e_3 \cos a_3 \\ \cos e_3 \sin a_3 \\ \sin e_3 \end{pmatrix} = A'\, B' \begin{pmatrix} \cos e_5 \cos e_5 \\ \cos e_5 \sin e_5 \\ \sin e_5 \end{pmatrix}$$

where

B' is the transpose of B

A is the matrix which transforms the S_3 components of a vector into the S_1 components of that vector. This matrix is given in equation (11).

Error Analysis

The problem now to be considered is that of estimating the accuracy to which the spacecraft attitude and moon direction may be determined from erroneous transits. The following assumptions are made:

(1) The true spacecraft attitude varies linearly with time in the data gathering time interval, i.e., the angles η_1, η_2 and s_o are linear functions of time. Moreover, the time rates of each of these angles is less than a minute of arc per minute.

(2) The eight unknowns associated with the attitude determination problem are computed from data gathered over five minutes and ten minutes of time (two cases) but the moon direction is obtained from only three successive moon transits. The rotation rate of the instrument is one RPM so the instrument completes, respectively, five and ten rotations in gathering the stellar transits.

(3) At each transit a random error is made in reading the angle encoder and transit time. These errors are unbiased and independent. Moreover, all encoder errors are independently distributed as well as all time errors. The standard deviation of each angle error is one minute of arc, and that of the transit time is .1 second of time.

(4) The criterion for stellar detectability is the same as for moon detectability given earlier except an additional restriction that detectable stars be brighter than magnitude 2.2 is imposed. Saturn is included as a stellar target.

(5) A moon being in the field of view does not affect stellar detectability.

The time error given in assumption (3) has almost no effect on the output errors. This is because neither the attitude nor the moons' directions change greatly in 0.1 seconds.

The attitude can be obtained at any time that two or more stars are detected per scan of the instrument. However, here the attitude is used only to compute the moon direction and, hence, has interest only near the times a moon is in the field of view. Results will be shown only for these times.

Figure 20 is a plot of the error in direction (two angles) of the moon and error in spececraft attitude at the first forty-four moon sightings of orbit number 1 (defined earlier). For this plot a five minute data gathering interval is used. Here we define attitude error as

$$\sqrt{\sigma^2 (\delta \eta_{10}) + \sigma^2 (\delta \eta_{20}) + \sigma^2 (\delta s_o)} .$$

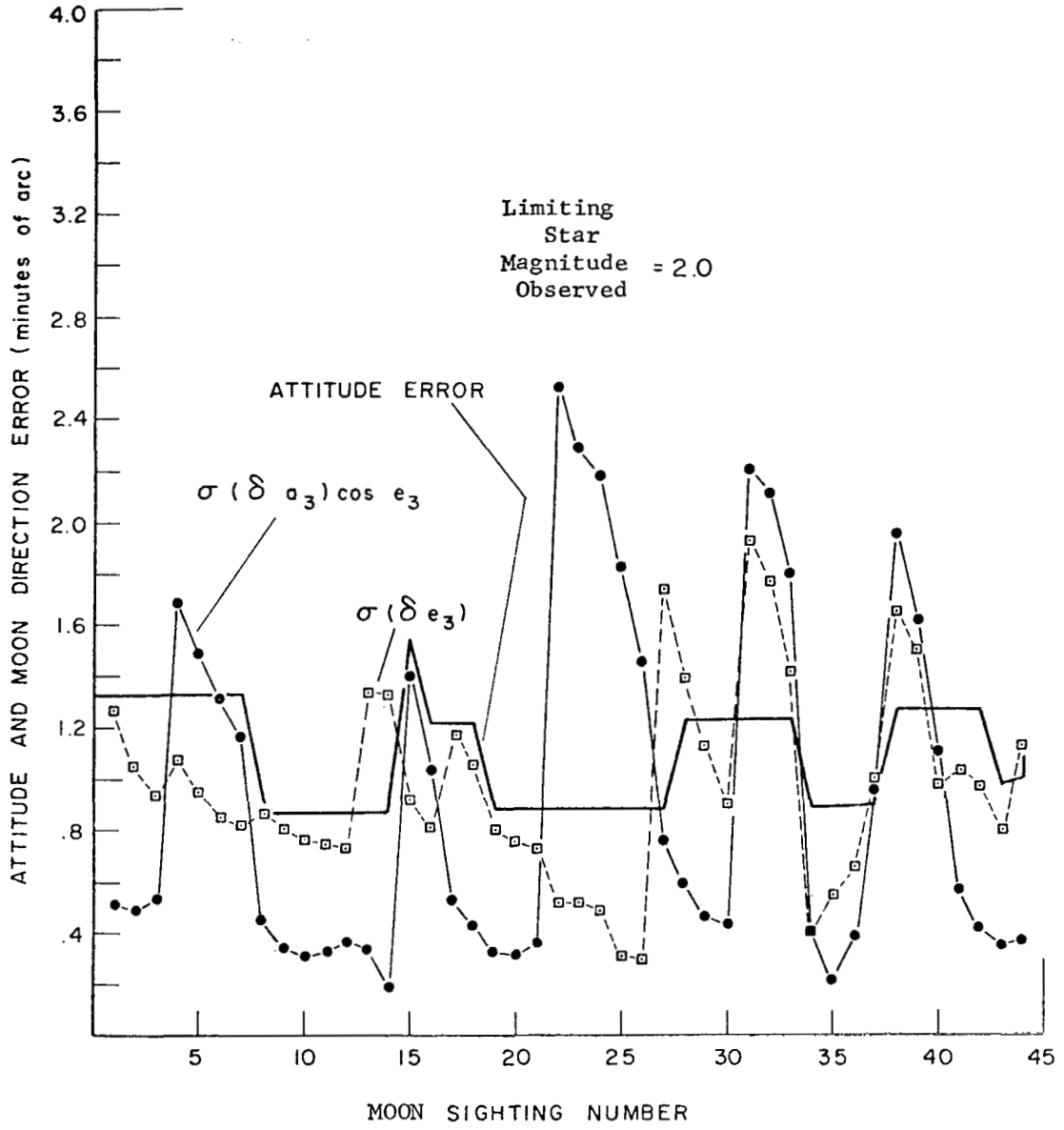

Figure 20: Attitude error and direction error as a function of sighting number. Orbit number 1.

Note that attitude error is almost constant over many sets of consecutive sighting numbers. This condition occurs when consecutive sighting numbers have corresponding times relatively close which, in turn, implies that the detected stellar field changes very little. The azimuth and elevation errors, however, change even though the attitude error may not; for, the moon direction does change and the slit configuration does not allow for computation of equal direction error independent of the moon's location in the field of view. Figure 20 may be incomplete in that it gives the attitude and direction errors at only 44 out of the 157 moon sightings which were used. At some of the moon sightings other than those shown in figure 20, the stellar background is poor in that only one or two stars are available. At these sightings the errors can become quite large.

A more complete indicator of the errors is given in figure 21 which is a plot of the cumulative probability distribution of the two components of the moon direction error. This plot was obtained from the direction errors at each moon sighting over orbit number 1 for the five and ten minute data gathering intervals. From figure 21 it is noted that if the probability is set at .5, then each direction component has an error of approximately five arc minutes if the five minute data gathering interval can be used. (The corresponding attitude error is 3.2 arc minutes.) However, if the ten minute data gathering interval can be used, then the corresponding direction errors are approximately three arc minutes. Hence, our assumption in the discussion of the navigation problem that each component error of one arc minute is optimistic.

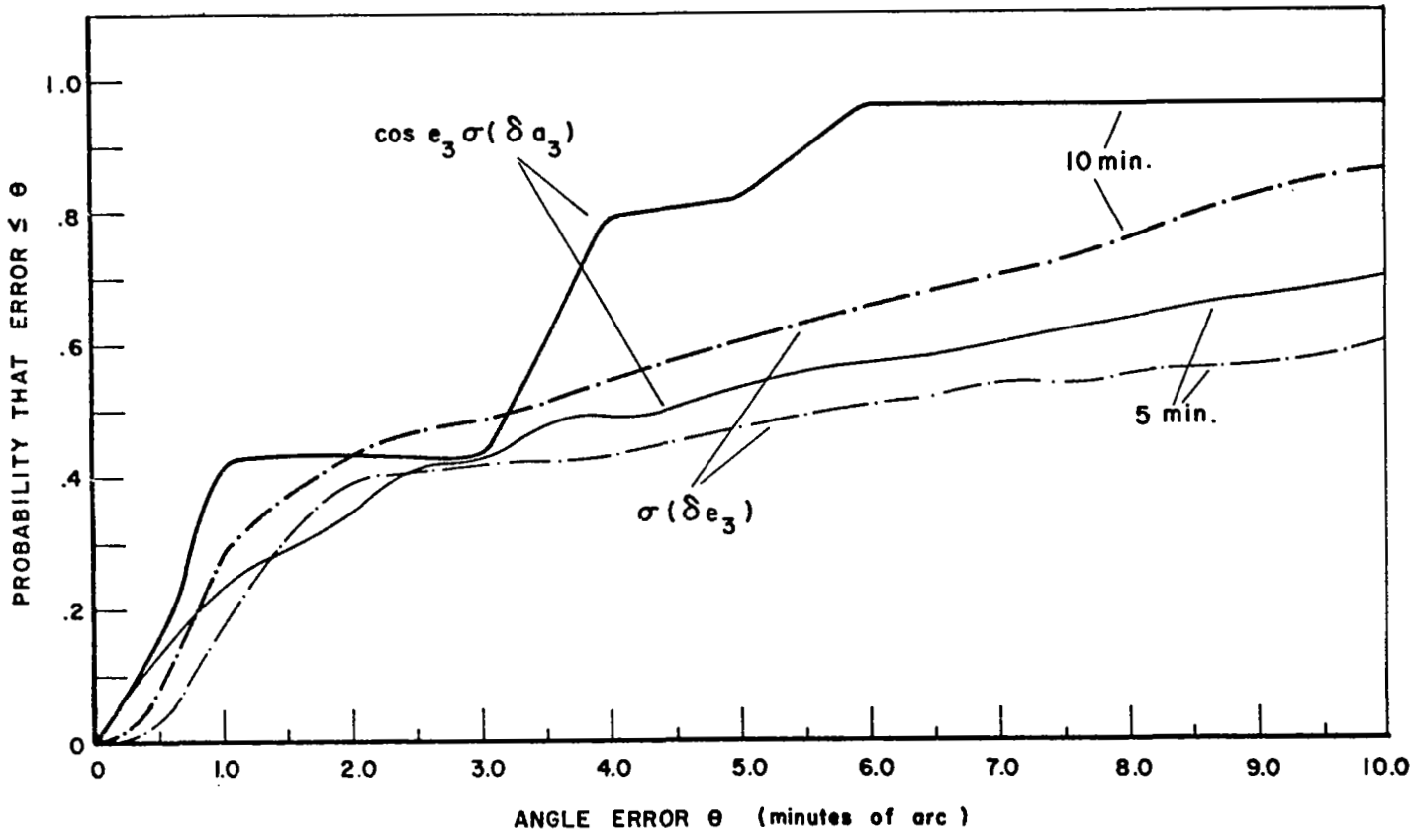

Figure 21: Cumulative probability distribution of moon direction error for cases in which stellar transits are gathered over 5 and 10 minutes of time. Orbit number 1.

SENSOR DESIGN AND ANALYSIS

Introduction

The sensor design is based on a realizable electronic implementation of the signal detection process which allows operation over a wide range of signal amplitudes without compromising the capability of the sensor to acquire measurements with the required accuracy. The sensor accuracy is analyzed for both star transit measurements and Mars moon transits. Correction factors for the moon transit measurements are approximately determined as a function of moon-sun phase angle and moon-spacecraft distance. A more refined analytical model for estimating moon transit correction factors is also presented.

Instrument Parameters

A large number of interacting parameters must be selected in arriving at a suitable instrument design for the studied application. Previously, it has been determined (pages 31-36) that in order to obtain a sufficient frequency detection for the moons of Mars and the stars brighter than second magnitude, the field of view must be at least 20^{o} when canted at an angle (Γ) 45^{o} with respect to the vehicle spin axis. In this section a realizable detection method is demonstrated that will detect celestial targets over a wide range of star intensities (10^{4}) as will be encountered during the mission. In the process of mathematically deriving the signal-to-RMS noise ratio at the output of the design filters, preferred values of instrument parameters such as scan period, aperture size, and slit width are determined.

A summary of the instrument parameters investigated throughout the total study is found in Table XIII.

TABLE XIII

SENSOR PARAMETERS

Slit Width	—	3.77 arc minutes
Cant Angle	—	45^{o}
Field of View	—	20^{o}
Scan Period	—	60 seconds
Aperture	—	0.5 inch
Limiting Magnitude Star	—	$2^{m}.2$

Signal Detection

The brightest celestial target to be detected is Phobos at - 8.3 magnitude

and the dimmest star to be detected is about + 2.2 magnitude. This constitutes a dynamic intensity range of about 10^4. This wide range of target intensities (factor of 10^4) requires special consideration for signal filtering and signal detection. It is desirable to employ a pulse detection method which automatically adjusts the threshold up and down with the intensity of the target being detected. A realizable method for implementing an automatic detection threshold is diagrammed in figure 22.

The method employs two low-pass filters, denoted by F_1 and F_2, with the inputs of each drived by the unfiltered star signal, f(t). Filter F_1 has a transfer function which approximates a linear phase versus frequency characteristic which allows preservation of the symmetrical properties of the signal pulse (reference 8, p. 131). Pulse symmetry is desirable for accurate transit time determination since the transit time is chosen as the average of the leading and trailing edge threshold crossings. The time constants for filter F_1 are adjusted so that the ratio of the peak output signal to the noise equivalent bandwidth is maximized. This results in a filter impulse response which is very closely matched to the input star signal (reference 8, pp. 122-143). The filter labeled F_2, shown in figure 22, is also a linear phase filter, although the requirements for linear phase are less critical than for filter F_1. Filter F_2 will be utilized to filter the input star signal before the peak value of the star signal is stored with a peak detector. The peak detector output is then multiplied by an appropriate factor, such as 0.6, to serve as the threshold for the transit level detector. Filter F_2, driving the peak detector input, must exhibit less delay of its output with respect to the input than the output-input delay of the "matched" filter since the peak for the output from F_2 must occur slightly before the 50% output level of F_1 occurs. The output pulse from the transit level detector is used to gate the contents of the binary clock into a storage register.

The primary level detector shown in figure 22 has a threshold which is set sufficiently above the RMS noise level to meet a specified false detection rate. This level detector triggers whenever the leading edge of a pulse from the output of filter F_2 exceeds the pre-set threshold. The leading edge of the primary level detector output triggers suitable digital delay pulses to strobe the transit level detector output and to reset (discharge) the peak detector circuit after the transit detection has occurred in preparation for storing the peak of the next star signal.

Figure 23 shows a plot of the output signal (noise free) from filters F_1 and F_2 for a symmetrical noise-free input signal which represents a typical star pulse (noise-free) at the photomultiplier output. The transfer function for filter F_1 was taken from reference 9 as

$$H(s) = \frac{1}{\left[2.42\left(\frac{s}{\omega_c}\right)^2 + 2.62\left(\frac{s}{\omega_c}\right) + 1\right]\left[0.734\left(\frac{s}{\omega_c}\right)^2 + 0.49\left(\frac{s}{\omega_c}\right) + 1\right]}. \qquad (20)$$

This transfer function approximates the linear phase-frequency characteristic and at four frequencies it matches the linear phase characteristic exactly.

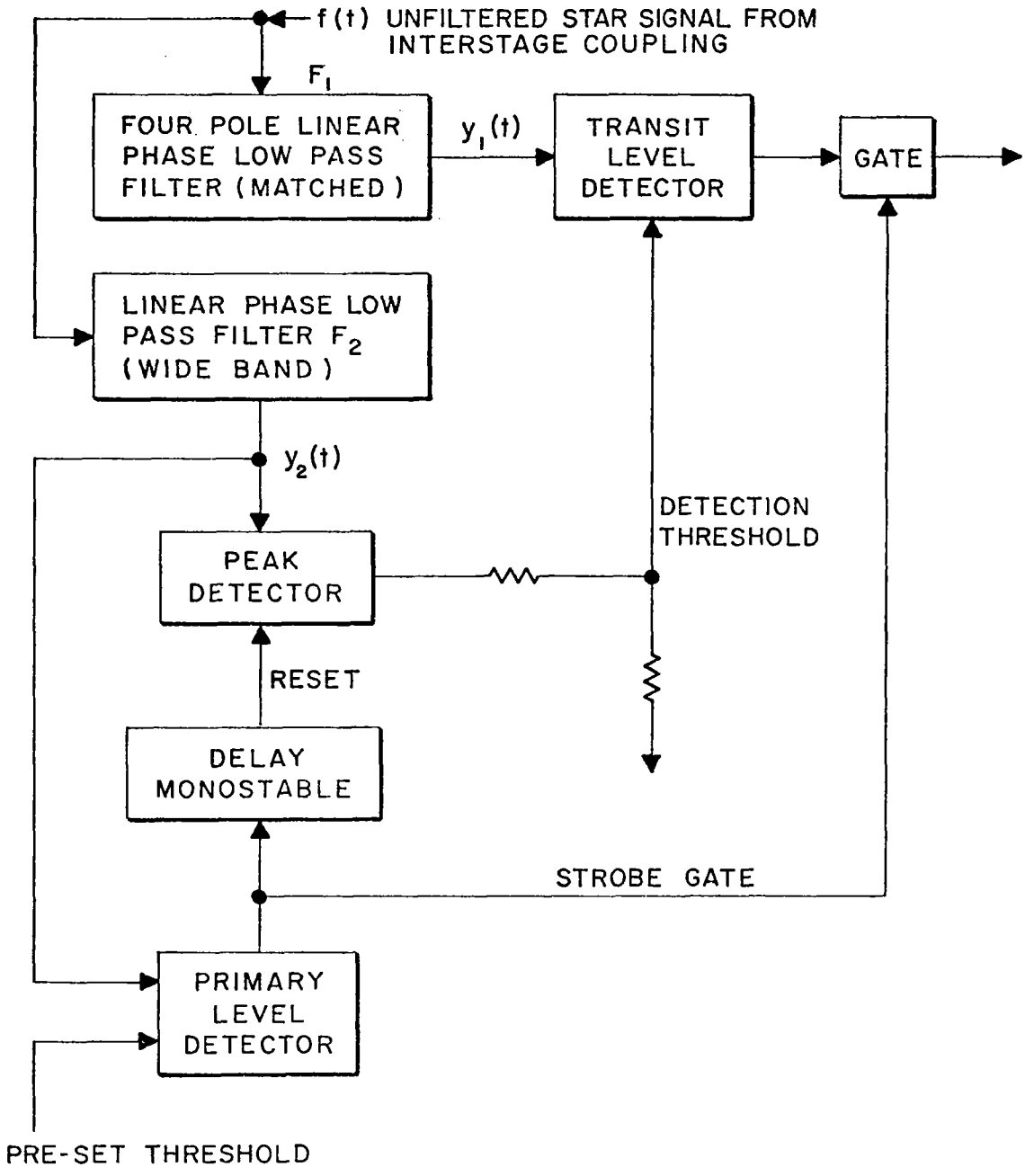

Figure 22: Automatic detection threshold.

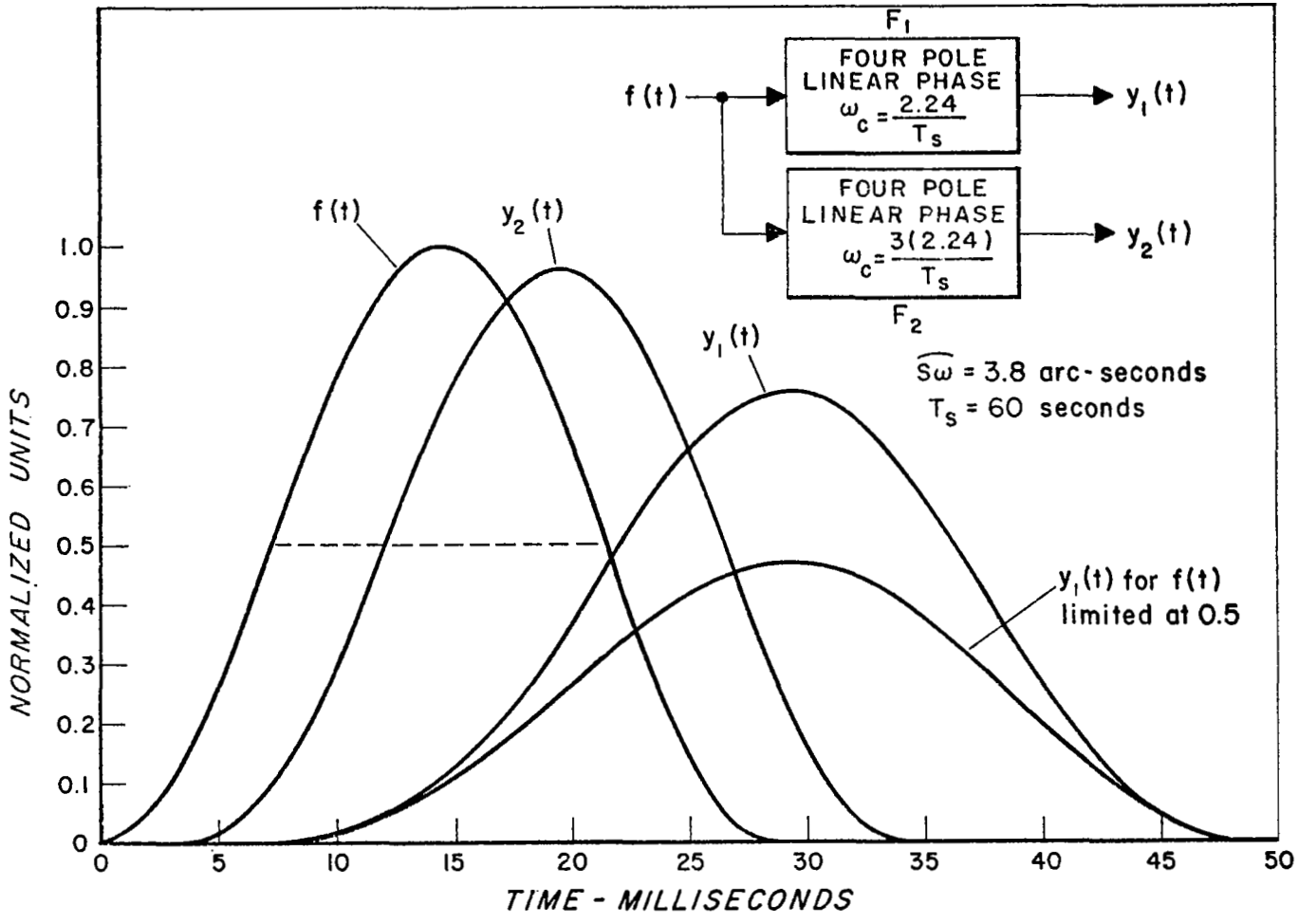

Figure 23: Signals from four-pole linear phase filters F_1 and F_2.

The impulse response for this transfer function was determined by partial fraction expansion of equation (20) and from a table of Laplace transforms and was found to be

$$h(t) = (0.5630)\left(2a_1\,\omega_c e^{-R\omega_c t}\cos(S\omega_c t) + 2a_2\,\omega_c e^{-R\omega_c t}\sin(S\omega_c t)\right. \quad (21)$$

$$\left. + 2c_1\omega_c e^{-\omega_c V t}\cos(U\omega_c t) + 2c_2\omega_c e^{-\omega_c V t}\sin(U\omega_c t)\right)$$

where

$a_1 = 1.48348 \times 10^{-1}$

$c_1 = -a_1$

$a_2 = 1.21$

$c_2 = 3.4765 \times 10^{-1}$

$R = 0.5413$

$V = 0.3338$

$S = 0.3467$

$U = 1.1185$

The output signal from filter F_2 is given by the convolution integral

$$y(t) = \int_0^\infty f(\tau) \cdot h(t-\tau)\, d\tau \quad (22)$$

where the input signal is taken as (reference 8, pp. 122-143).

$$f(t) = \sin^2\left(1.17\,\frac{t}{T_s}\right) \text{ for } 0 \le t \le \pi\left(\frac{T_s}{1.17}\right) \quad (23)$$

$$= 0 \qquad \text{elsewhere.}$$

The parameter T_s represents the transit time of a point image to cross the slit, where (reference 8 pp.122-143)

$$T_s = \frac{\widehat{s\omega} \cdot T}{2.16 \times 10^4} \quad (24)$$

T = scan period in seconds

$\widehat{s\omega}$ = slit width in arc-minutes

The value of the filter parameter, ω_c, was determined from the "matching" procedure described in reference 8, pp. 122-143. For the four-pole linear phase filter, the ratio of

$$\frac{y \text{ peak}}{\sqrt{\omega_c}}$$

is a maximum for the given input when

$$\omega_c = \frac{2.24}{T_s} \quad . \tag{25}$$

The noise equivalent bandwidth, Δf, of the filter implied by equation (20) is given by (reference 8, pp. 122-143).

$$\Delta f = \frac{1}{4\pi} \int_{-\infty}^{+\infty} | H(j\omega) |^2 \, d\omega = 0.809 \frac{\omega_c}{2\pi} = \frac{0.288}{T_s} \quad . \tag{26}$$

The transfer function for filter F_2, whose output is also shown in figure 23, was also taken to be that given by equation (20). This filter is "matched" to f(t) when

$$\omega_c = \frac{2.24}{T_s} \quad .$$

but since it is required that filter F_2 have less delay than filter F_1, the value of ω_c was selected as

$$3 \frac{(2.24)}{T_s} \quad .$$

Figure 23 shows how the detection method can accommodate the wide range of target intensities which the sensor must observe. The input signal is shown clipped at the 50% level which corresponds to a bright target, causing the pre-amplifier at the photomultiplier to limit (saturate). The corresponding output signal from filter F_1 is shown and it should be noted that this signal is symmetrical and the employment of the peak detector variable threshold will provide an accurate detection of the clipped signal. Accurate detection free of induced systematic electronic errors will be realizable as long as the "noise free" signal from the photomultiplier is symmetrical. Signals from the photomultiplier which exhibit variable asymmetry will always introduce some systematic errors in the detection process if correction factors are not determined.

It is of interest to compute the signal-to-noise ratio at the output of filters F_1 and F_2. The total noise power at the output of a filter used in a scanning optical sensor is derived in reference 10 (pp. III-67 to III-83). This noise power consists of the summation of two components. One component, N_1, is due to the random variation of the photon arrival rate from the radiant power in the star image. This noise component is commonly termed shot noise. The

second component, N_2, arises because of the scanning of a non-uniform background which consists of a random spatial distribution of stars whose magnitudes are greater than the threshold magnitude.

The shot noise power is given by (reference 10, p. III-68)

$$N_1^2 = e\,\overline{a^2}\,\bar{I}\int_0^\infty h^2(t)\,dt \text{ amperes} \tag{27}$$

where

e = electron charge

$= 1.6 \times 10^{-19}\ \frac{\text{coul}}{\text{electron}}$

$\overline{a^2}$ = factor due to the noise introduced by the dynode chain of the photomultiplier

$\bar{I}$ = average current generated at the photocathode by the average background radiant power and the star radiant flux.

The integral $\int_0^\infty h^2(t)\,dt$ is equal to

$$\int_{-\infty}^{\infty} H(j\omega)\cdot H^*(j\omega)\,df = \int_{-\infty}^{\infty} |H(j\omega)|^2\,df \tag{28}$$

by Parseval's theorem, hence from equation (26)

$$\int_0^\infty h^2(t)\,dt = 2\,\Delta f. \tag{29}$$

The average current, $\bar{I}$, in equation (27) consists of the average current due to background radiation plus the current produced when the star image is centered in the slit. The current produced by the star image is included since the noise computed for the peak signal-to-noise must include the noise generated by the signal itself.

The peak signal current for a star of magnitude M is given by

$$I_s = \epsilon_o\,\frac{\pi}{4}\,D^2\,S_K \times 10^{-.4M} \tag{30}$$

where

ϵ_o = the overall optical efficiency

D = the effective optical aperture diameter

S_K = the photocathode sensitivity per unit area of optical aperture for a zero magnitude star having a given spectral energy distribution

M = star magnitude

The above expression for I_s assumes that 100% of the radiant power concentrated in the star image is passed by the slit. However, the slit may block a small percentage of the radiant power in the star image so as a worst case it is assumed that only 80% of the available radiant power of the star images passes the slit (reference 8, pp. 128-129).

The average component of $\bar{I}$ generated by the background radiation is given by

$$I_B = \epsilon_o \frac{\pi}{4} D^2 S_K 10^{-4} N_B S_A \tag{31}$$

where

N_B = total integrated starlight from stars of sixth magnitude and dimmer which is expressed as equivalent tenth magnitude stars per unit area on the celestial sphere

S_A = total slit area projected on the celestial sphere as seen by the photocathode through the slit plane.

The total slit area is given by (reference 8, p. 149)

$$S_A = N_s \frac{\widehat{s\omega}}{60} \left[\cos\left(\Gamma - \frac{FOV}{2}\right) - \cos\left(\Gamma + \frac{FOV}{2}\right)\right] \frac{180}{\pi} (\text{degree})^2 \tag{32}$$

where

N_s = number of slits radial to the spin axis of the sensor

$\widehat{s\omega}$ = rotational slit width expressed in arc-minutes

Γ = cant angle of the sensor optical system with respect to the vehicle spin axis

FOV = field of view of the optical system.

Combining equations (30), (31), and (32) gives

$$\bar{I} = 0.8 I_s + I_B . \tag{33}$$

In deriving equation (33), it is assumed that the photomultiplier cathode dark current is much less than $\bar{I}$.

The noise component due to scanning the non-uniform background is given by (reference 10, p. III-70)

$$N_2^2 = \epsilon_o^2 \left(\frac{\pi}{4} D^2\right)^2 S_K^2 \overline{\lambda^2} S_A J \sum A_M \tag{34}$$

where

$$J = T_s \int_{-\infty}^{\infty} \frac{\sin^2\left(\frac{\omega T_s}{2}\right)}{\left(\frac{\omega T_s}{2}\right)^2} e^{-(\omega\sigma)^2} |H(j\omega)|^2 \, df$$

$\overline{\lambda^2}$ = square of the star intensity averaged with respect to star density and star magnitude with the average taken only for stars which are dimmer than the threshold magnitude, M_o.

The mean square intensity may be computed as follows:

$$\overline{\lambda^2} = \frac{\sum_{M=M_o+1}^{\infty} A_M \, 10^{-0.4(2)M}}{\sum_{M=M_o+1}^{\infty} A_M} \tag{35}$$

where

A_M = average number of stars per square degree within the brightness range M + 1/2 to M - 1/2.

Figure 23 shows a plot of the noise-free output signal for both filters F_1 and F_2. As can be seen, the noise-free unity input peak is attenuated by filter F_1 to an output peak of 0.76 and is attenuated by filter F_2 to an output peak of 0.9674. The peak of the noise-free input signal corresponds to an assumed worst case of 80% of the total radiation concentrated in the star image which passes the slit and strikes the photocathode. Hence, the input signal peak to both filters corresponds to 0.8 I_s. Therefore, the output peak signal for filter F_1 corresponds to

$$S_1 = 0.8 \times 0.76 \times S_K \, 10^{-.4M} \frac{\pi}{4} D^2, \tag{36}$$

and the outpeak signal for filter F_2 corresponds to

$$S_2 = 0.8 \times 0.9674 \times S_K \, 10^{-.4M} \frac{\pi}{4} D^2. \tag{37}$$

By observing equations (27), (30), (31), (33), (35), and (36) it is apparent that the square of the peak signal-to-RMS noise ratio may be written as follows:

$$R = \left(\frac{S_i}{N}\right)^2 = \left[\frac{S_i}{\left(N_1^2 + N_2^2\right)}\right]^2 = \frac{k_s D^4}{k_1 D^2 + k_2 D^4} \tag{38}$$

where

$$k_s = \left(0.8 \times 0.76 \times S_K \, 10^{-.4M} \frac{\pi}{4}\right)^2 \text{ for filter } F_1$$

$$k_s = \left(0.8 \times 0.967 \, S_K \, 10^{-.4M} \frac{\pi}{4}\right)^2 \text{ for filter } F_2$$

$$k_1 = e \, \overline{a^2} \, 2 \, \Delta f \left(0.8 \, \epsilon_o \, S_K \, 10^{-4M} + \epsilon_o \, S_K \, 10^{-4} \, N_B \, S_A\right) \frac{\pi}{4}$$

$$k_2 = \epsilon_o^2 \, S_K^2 \left(\frac{\pi}{4}\right)^2 \overline{\lambda^2} \, S_A \, J$$

Equation (38) may be solved for the optical aperture diameter so that

$$D = \left[\frac{k_1 R}{k_s - R k_2}\right]^{\frac{1}{2}}. \tag{39}$$

Slit Width

Before the optical aperture diameter can be calculated, the slit width and scan period must be determined. The required slit width can be derived by identifying and considering the error sources of the scanning star sensor. The following errors will be expected to dominate:

(1) angle encoder quantization error,

(2) uncertainty in the detection threshold crossing due to noise superimposed on the signal,

(3) bearing eccentricities,

(4) thermal deformation of slit pattern location,

(5) change of cant angle due to thermal deformation,

(6) optical aberrations, and

(7) sensor mounting errors.

The above seven sources of error should be expected to equally contribute to the overall error for a well balanced design. Hence, if the overall RMS error is ϵ, then

$$\epsilon^2 = \sum_{i=1}^{i=7} \Delta_i^2 = 7\,\Delta^2 \tag{40}$$

For the scanning sensor, ϵ should be 60 arc seconds; hence Δ = 22.7 arc seconds. Noise source number 2, listed above, is related to the slit width and the peak signal-to-RMS noise ratio. The uncertainty in the threshold crossing expressed in terms of the slit width is approximately equal to the slit width divided by the signal-to-RMS noise ratio. For a reliable sensor design it is a practical requirement that the peak signal-to-RMS noise ratio be at least ten to one. Therefore, the slit width, $\widehat{s\omega}$, required for an RMS detection error of Δ = 22.7 arc seconds is

$$\widehat{s\omega} = \Delta \left(\frac{S}{N}\right) \times \frac{1}{60} = 3.77 \text{ arc minutes.} \tag{41}$$

Scan Period

Some of the parameters that affect the scan period are field of view and cant angle. Computer simulations of orbital sightings of Deimos, Phobos, and the star field during the mission have defined the angle of the optical axis with respect to the vehicle spin axis (cant angle) as 45 degrees. In "Detectability of the Moons", other instrument fields of view and minimum bright source shield angles (thus, a corresponding change in cant angle) were run, but these cases gave either marginally acceptable Photos detectability or implied an instrument of unacceptably large dimensions.

The area scanned on the celestial sphere during one revolution of the spin axis is (reference 11, pp. 23-26)

$$A_s = 2\pi \left[\cos\left(\Gamma - \frac{FOV}{2}\right) - \cos\left(\Gamma + \frac{FOV}{2}\right)\right] \left(\frac{1.8 \times 10^2}{\pi}\right)^2 \text{ (degrees)}^2 \tag{42}$$

$$= 2\,[\cos(35^\circ) - \cos(55^\circ)]\,\frac{(1.8)^2}{\pi} \times 10^4$$

$$= 0.505 \times 10^4 \text{ (degrees)}^2.$$

From reference 12, the average number of stars per square degree of second magnitude (photographic) or brighter is given as 9.12×10^{-4}. Hence, the average number of stars detected per scan period is $9.12 \times 10^{-4} \times 0.505 \times 10^{4} = 4.6$. In order to limit the accumulative attitude error resulting from an imperfect mathematical model assumed for the vehicle motion, it is required that the time between star transits be limited to fifty seconds, or less.
So, a scan period of

$$T = 50 \frac{\text{seconds}}{\text{transit}} \times 4.6 \frac{\text{transits}}{\text{revolution}} = 270.0 \text{ seconds or less}$$

meets this requirement. As a result, equation (39) will be solved for the optical aperture diameter for both T = 120 seconds and T = 60 seconds.

Aperture

The photocathode sensitivity for an EMR type-N cathode is (reference 11, pp. 29-37)

$$S_K = 8.25 \times 10^{-14} \frac{\text{amp}}{(\text{cm})^2}$$

for a zero magnitude class A0 star, so for filter F_1 and M = 2, k_s in equation (38) is

$$k_s = 0.39 \times 10^{-28} \tag{43}$$

for T = 120 seconds and $\widehat{s\omega}$ = 3.8 arc minutes, $T_s = 2.11 \times 10^{-2}$ seconds from which

$$\Delta f = \frac{0.288}{0.211 \times 10^{-1}} = 13.6 \text{ Hertz for filter } F_1.$$

The photomultipler gain noise factor is $\overline{a^2} = (1.3)^2$ (reference 10, pp. V-42 to V-50; reference 13, pp. 126-127) and $S_A = 2.66$ (degree)^2 for $N_S = 3$, $\widehat{s\omega} = 3.8$ arc minutes, $\Gamma = 45^{\circ}$, and field of view = 20°. So, for a stellar background of N_B = 320 tenth magnitude stars per (degree)^2 (reference 10, p. III-60) and an overall optical efficiency of $\epsilon_o = 0.5$,

$$k_1 = 5.07 \times 10^{-32}. \tag{44}$$

The mean square intensity as determined by equation (35) may be computed from data given by C. W. Allen (reference 12, p. 135) with $M_o = 2$. This data and the computations are tabulated in Table XIV for M = 3 to M = 10. The result is

$$\overline{\lambda^2} \sum A_M = 0.21 \times 10^{-4}.$$

TABLE XIV

COMPUTATION OF MEAN SQUARE INTENSITY FOR STELLAR BACKGROUND			
M	A_M	$10^{.8M}$	$A_M\ 10^{-.8M}$
3	2.69×10^{-3}	2.51×10^{2}	0.11×10^{-4}
4	8.31×10^{-3}	1.58×10^{3}	0.05×10^{-4}
5	2.51×10^{-2}	10^{4}	0.025×10^{-4}
6	7.95×10^{-2}	6.3×10^{4}	0.013×10^{-4}
7	2.14×10^{-1}	3.98×10^{5}	0.0054×10^{-4}
8	5.62×10^{-1}	2.51×10^{6}	0.0022×10^{-4}
9	1.55	1.58×10^{7}	0.00098×10^{-4}
10	4.17	10^{8}	0.00042×10^{-4}
			$0.207 \times 10^{-4} = \overline{\lambda^2} \sum A_M$

The integral in equation (34) was rewritten as

$$J = \frac{1}{\pi a} \int_{-\infty}^{\infty} \frac{\sin^2 ax}{x^2} e^{-x^2} \left| H\left(j \frac{x}{\sigma}\right) \right|^2 dx \qquad (45)$$

where

$$a = \frac{T_s}{2\sigma} = \frac{2.56\ \sigma}{2\ \sigma} = 1.28. \qquad (46)$$

This integral was evaluated numerically for $\omega_c = \frac{2.24}{T_s}$, with the result $J = 0.41$. Hence,

$$k_2 = 2.41 \times 10^{-32}.$$

For a peak signal-to-RMS noise ratio of ten to one, $R = 10^2$ in equation (39), so

$$D = 0.37 \text{ cm} = 0.146 \text{ inch}.$$

This aperture is quite small, so it is possible to reduce the scan period. Repeating the computations for T = 60 seconds

$$D = 0.525 \text{ cm} = 0.206 \text{ inch}.$$

It is interesting to note for this case $N_1 = 2.82 \times 10^{-32}$ and $N_2 = 0.183 \times 10^{-32}$. The scanning noise power, N_2, tends to be small if the limiting optical aperture diameter is below one centimeter because $N_1 = k_1 D^2$, whereas $N_2 = k_2 D^4$. In general, small optical aperture diameters result because of very slow scan rates.

For filter $F_2 = \frac{3(0.288)}{T_s} = 0.82 \times 10^2$ for T = 60 seconds,

so

$$k_1 = 30.6 \times 10^{-32}.$$

Also, the integral in equation (45) becomes $J = 5.2 \times 10^{-1}$ when ω_c is tripled, so $k_2 = 3.06 \times 10^{-32}$. Since the output pulse from F_2 peaks at 0.967 of the input peak, $k_s = 0.628 \times 10^{-28}$. Therefore,

$$R = \left(\frac{S}{N}\right)^2 = 55 \text{ or } \frac{S}{N} = 7.42 \text{ when } D = 0.206 \text{ inch.}$$

The diameter of 0.21 inch is still physically small so the optical aperture diameter can be increased to 0.5 inch without compromising size constraints. For D = 0.5 inch = 1.25 cm and T = 60 seconds, the peak signal-to-RMS noise ratio at the output of filter F_1 becomes 21.1 and at the output of F_2 becomes 16.9.

Optical System

Both reflective and refractive optical systems were considered for the application. A 20° field of view causes serious central obscuration in any refractive system even at the focal surface of the system. For the scanning configuration, a 10 min image size could be obtained with the PMT directly in contact with the focal surface. However, since it is advantageous to rotate the optical system about an axis canted 45° from the optical axis, the presence of a PMT in the rotating member would require rotating electrical contacts between the PMT, the PMT supply, and detection electronics. The focal surface could be shifted outside the primary mirror housing either by a plane mirror, as in a Newtonian configuration, or by a hyperbolic secondary as in a Cassegrain configuration. In either case, however, the result of the image transfer would be an increase in central obscuration. Decrease in relative aperture required to compensate for the increased obscuration would increase the size of the blur spot beyond the baseline requirement of 10 min. Thus, a reflective system was not feasible for this application

The difficulties inherent in the wide field requirement for a reflective or catadioptric system are not present in the proposed refractive system, shown in figure 24, as a modified double gauss system of nine elements with three cemented doublets. The prescription has been adjusted to give maximum efficiency of light transfer when the star image formed by the lens is scanned by a radial slit. The parameters controlling the major off-axis aberrations, coma and

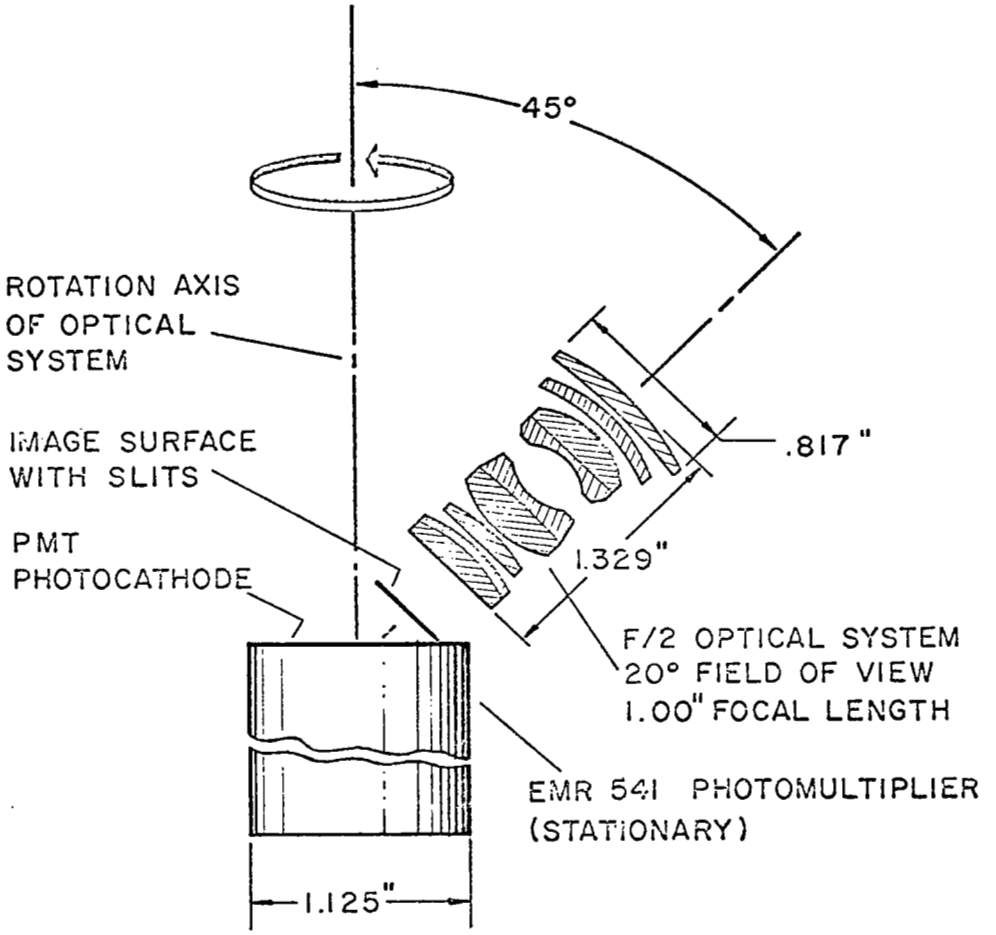

Figure 24: Optical system schematic.

astigmatism, were selected to produce image shapes narrow in the direction of the slit scan. The image surface is slightly concave to the lens with a radius of 38 inches. The diametral dimensions of the optical system are chosen to produce no vignetting of the image intensity for objects 10^{o} off the optical axis.

Transfer of light passing through the slits to the photosensitive surface of the photomultiplier (PMT) occurs at the interface between the rotating image surface and the stationary PMT. The PMT was chosen so that the most extreme ray from the upper part of the slit falls within the photosensitive boundary of the PMT cathode. Reflective surfaces on the housing surrounding the image surface-PMT interface increase the efficiency of the transfer by redirecting light into the PMT.

Photodetector Selection

In order to achieve adequate signal-to-noise ratios with a minimum aperture optical system for the detection of star signals with the scanning star sensor, it is required that the photodetector be a photomultiplier. Previous investigations have shown that current solid state detectors are inadequate or, at best, marginal for sensors rotating at relatively short scan periods. One of the principal reasons for the superiority of photomultipliers is the relative noise-free gain achieved by the electron multiplication provided by the secondary emmissions of the photomultiplier dynode chain (reference 13). The dynode chain provides adequate gain to raise the signal levels well above the level of the thermal Johnson noise of the photodetector load resistor.

Extensive investigation has been performed in the applicability of photomultiplier tubes. The results of these investigations have shown that Venetian blind tubes are optimum for several reasons; in particular, the rugged tube structure, the large photocathode area, and the high multiplier gain are some of its outstanding characteristics. Venetian blind photomultipliers have been utilized in two previous SCADS-type experimental systems. For a breadboard design of SCADS system (NAS5-9661), a Venetian blind tube designated as the EMR-543A (manufactured by Electro-Mechanical Research, Inc.) was employed. For the ATS Self-Contained Navigation System Experiment, the Venetian blind photomultiplier employed was an EMR-541E. Both tubes were ruggedized and capable of withstanding the environment of space vehicle launching. Since both tube types supplied by EMR performed satisfactorily, this study will primarily consider EMR photomultipliers.

The cathode type employed by the photomultiplier is particularly important in scanning sensor applications. It is desirable that the cathode exhibit high quantum efficiency and a low dark emission rate. EMR has given letter designations to indicate different cathode types. For example, the EMR-543A has a cathode designated as an "A" cathode, and its response conforms closely to an S-4 response with a typical peak quantum efficiency of fourteen percent and a cathode dark current of $.274 \times 10^{-15}$ ampere per square centimeter of cathode area at $+20^{o}C$. Similarly, the EMR-541E has an "E" cathode which conforms closely to an S-20 response with a typical peak quantum efficiency of

twenty-five percent and a cathode dark current of $.407 \times 10^{16}$ ampere per square centimeter at +20°C. The "E" cathode has a broad range of spectral response, plus its peak sensitivity corresponds closely with the spectral energy distribution of blue stars. The EMR "N" type cathode has a higher quantum efficiency than the "A" type but is somewhat less efficient than the "E" type. The "N" cathode response conforms closely to the S-11 response. Typical peak quantum efficiency of "N" cathode is 21.5 percent; however, its dark current is $.51 \times 10^{-17}$ ampere per square centimeter at +20°C. Hence, its dark current characteristic is much superior to either the "A" or "E" cathodes. In addition, the "N" cathode can withstand a much higher temperature (+150°C) than either the "A" (+75°C) or "E" (+85°C) cathodes. The high temperature characteristic is particularly attractive since some cathode heating is likely to occur if ever the sensor sees either direct sun radiation or Earth-reflected sun radiation.

Because of its desirable characteristics of relatively high quantum efficiency, low dark current and tolerance to high temperatures, the EMR type "N" cathode is recommended for the present scanning sensor. The type "N" cathode is currently available in the EMR-541N photomultiplier. The active cathode diameter of the EMR-541N is 25 millimeters which is sufficiently large to collect the energy from the canted optical system.

Sensor Electronics

Figure 25 provides an electronic block diagram for the celestial scanning sensor. The primary functions of the electronics are summarized below:

(1) Converts radian star energy passing through the rotating slit mask into electrical signals using a photomultiplier detector.

(2) Amplifies analog signals from the photomultiplier to levels convenient for signal detection and data encoding.

(3) Filters analog signals to maximize the signal-to-noise ratio and to also preserve the pulse shape in order to achieve the best possible system accuracy.

(4) Detects filtered analog signals by threshold detection where the threshold is automatically set to trigger at 50% of the signal peak through use of a peak detector circuit, delay filter, and level detector.

(5) Encodes with an incremental angle encoder (14 bits/revolution), the angular rotations of the sensor optics and reticle plane driven by a low power, brushless DC motor.

(6) Counts the number of pulses from the incremental angle encoder with a one bit counter which continuously cycles once per revolution of the optics and slit reticle.

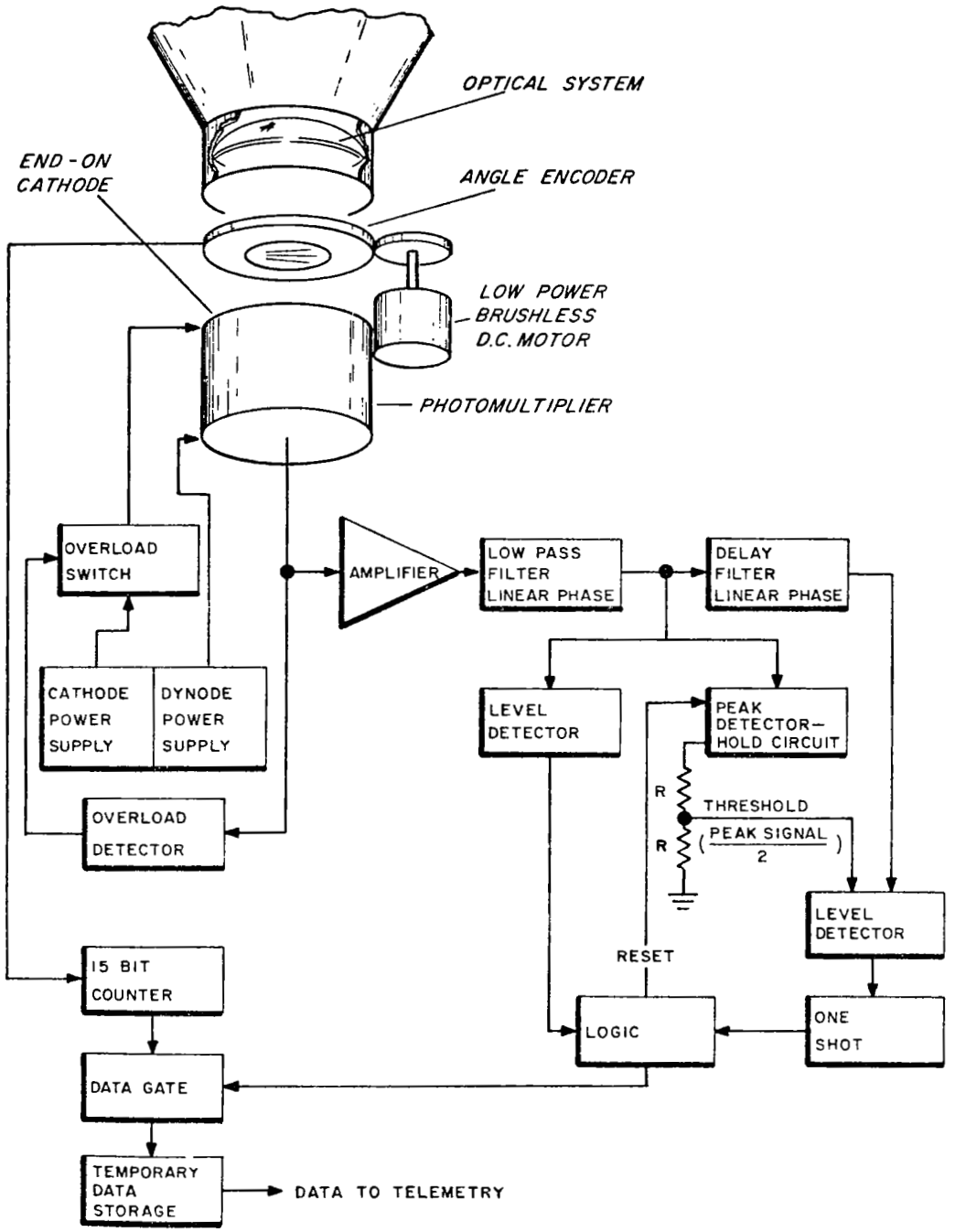

Figure 25: Block diagram - sensor electronics

(7) Gates the contents of the 14 bit counter into temporary data storage at the instant of leading edge threshold crossing and also at the trailing edge threshold crossing of the signal pulse threshold detection, produced each time an image of a stellar body transits any one of the three slits in the reticle mask.

(8) Detects overload conditions of the photomultiplier and reverse biases the cathode-first dynode to prevent cathode degradation caused by Mars reflected sunlight entering the optics or by inadvertent scanning of the sun.

Estimated Sensor Power Requirement

The estimated power required for the scanner is 7.9 watts distributed to the various parts of the instrument as follows:

Photomultiplier High Voltage Power Supply	0.5 watts
Angle Encoder	2.5 watts
Motor	3.0 watts
Electronics	1.4 watts
Low Voltage Power Supply	0.5 watts
Total	7.9 watts

Mechanical Design and Sensor Configuration

The design concept for the celestial scanner is shown in Figure 26 (CDC Dwg. No. 55003800). The light shield and optics are mounted at the top of a tube which surrounds the photomultiplier tube and rotates in two azimuth bearings. These bearings are mounted in the instrument housing separated by two bearing spacer sleeves used to control bearing preload. The photomultiplier tube is mounted in the base cover plate of the housing which is stationary.

The drive motor and speed reducer assembly is mounted on the base cover plate with the driving pinion extending through the plate to engage an internal gear mounted on the end of the rotating tube which supports the optics. The angle encoder is mounted near the top of the tube with the photoheads attached to the housing.

The drive motor would be a brushless DC motor similar in design to a unit made by the Marine Systems Division of Sperry Rand Corporation. Their brushless DC motors are qualified for space application and can be operated unsealed with service life in excess of the 90-day operating period for the Viking mission. With a motor which can be operated unsealed, the harmonic drive can be eliminated with a savings in weight and power consumption.

The bearings of smaller cross section are of the torque tube type similar to Fafnir AMVN546K but with separator and lubrication for operation in the hard

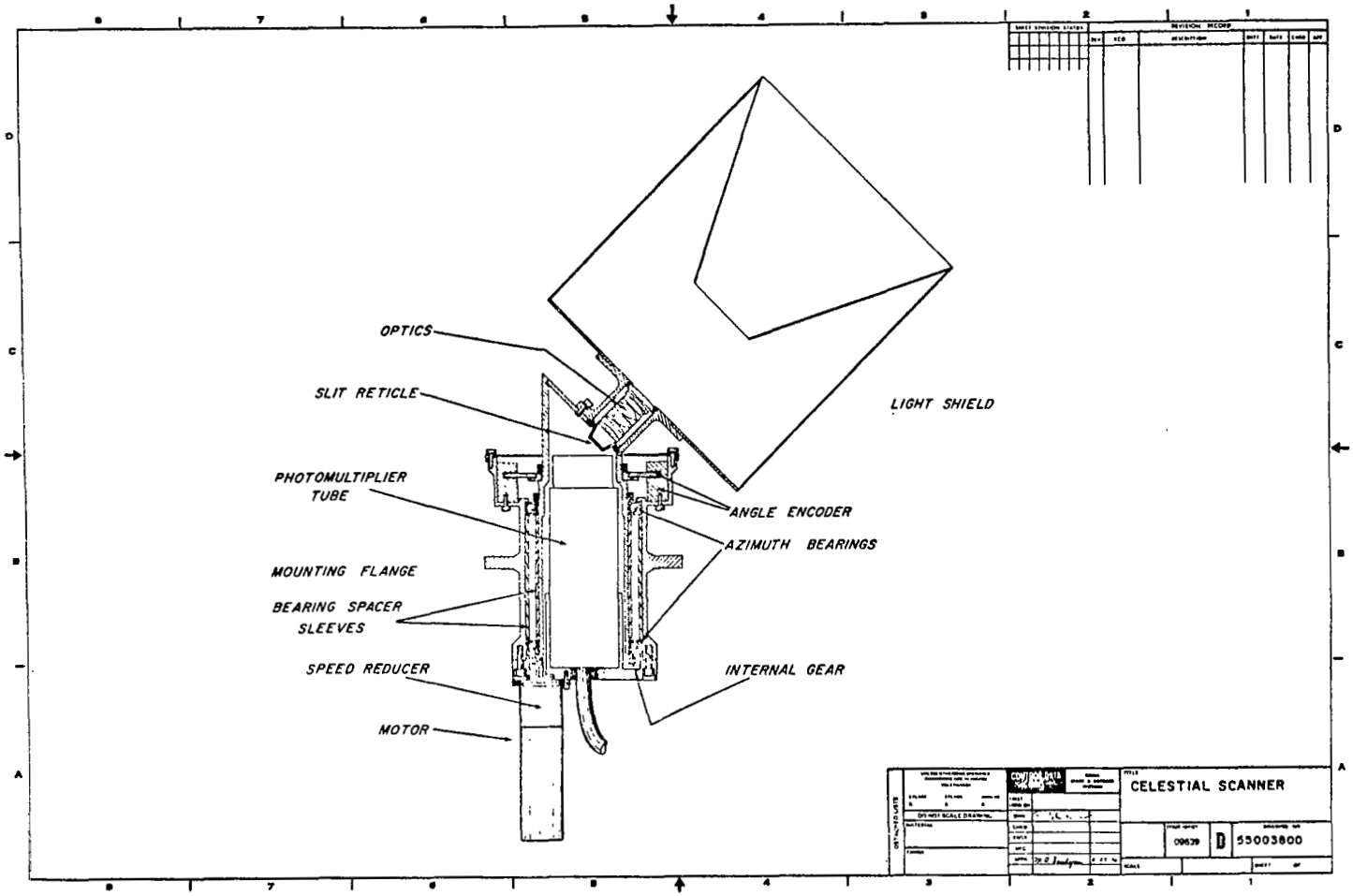

Figure 26: Mechanical configuration for scanning sensor.

vacuum of space. Since these bearings rotate at the low optical scanning rate of one revolution per minute, giving a total of approximately 10^5 revolutions (for the 90-day operating period) under essentially no load, adequate bearing life is assured.

The estimated weight of the sensor design is 7.0 pounds. Table XV shows a summary of the estimated weights of component parts.

TABLE XV

CELESTIAL SCANNER WEIGHT SUMMARY	
Light Shield	.41
Optics Assembly	.50
Photomultiplier with High-Voltage Power Supply	1.00
Angle Encoder	.19
Motor, Speed Reducer and Motor Controls	.67
Bearings, Spacers and Ring Nuts	.78
Housing	1.65
Electronics Assembly	1.80
	7.00 lbs

The space required by the scanner will be the volume of the stationary housing and drive motor, plus the swept volume of the light shield and optics. A sketch of the space envelope of the scanner is shown in figure 27. The overall height of the required space envelope is 18.81 inches. The maximum diameter of the housing is 5.0 inches. The motor extends 6.75 inches below the flange. The maximum diameter swept by the rotating light shield is 18.88 inches at a height of 7.38 inches above the flange.

Variance Calculation for Star Pulse Transit Time

Star pulse transit time may be accurately measured by averaging the leading and trailing edge threshold crossing times. It is possible to derive an analytic expression for the transit time variance from a few simple, valid assumptions. The noise amplitude is assumed to have a stationary Gaussian density function and the slope of the noise-free signal is assumed to be constant in the vicinity of the threshold crossings. The RMS noise level is assumed to be relatively small with respect to the noise-free signal which must be true to achieve reliable signal detection. The transit time variance may be calculated given the slope of the noise-free signal at both the leading and trailing edge threshold crossings, the correlation coefficient of the noise amplitudes in the vicinity of the trailing edge threshold crossing time with respect to the amplitudes at the leading edge crossing time, and the variance of the noise amplitude.

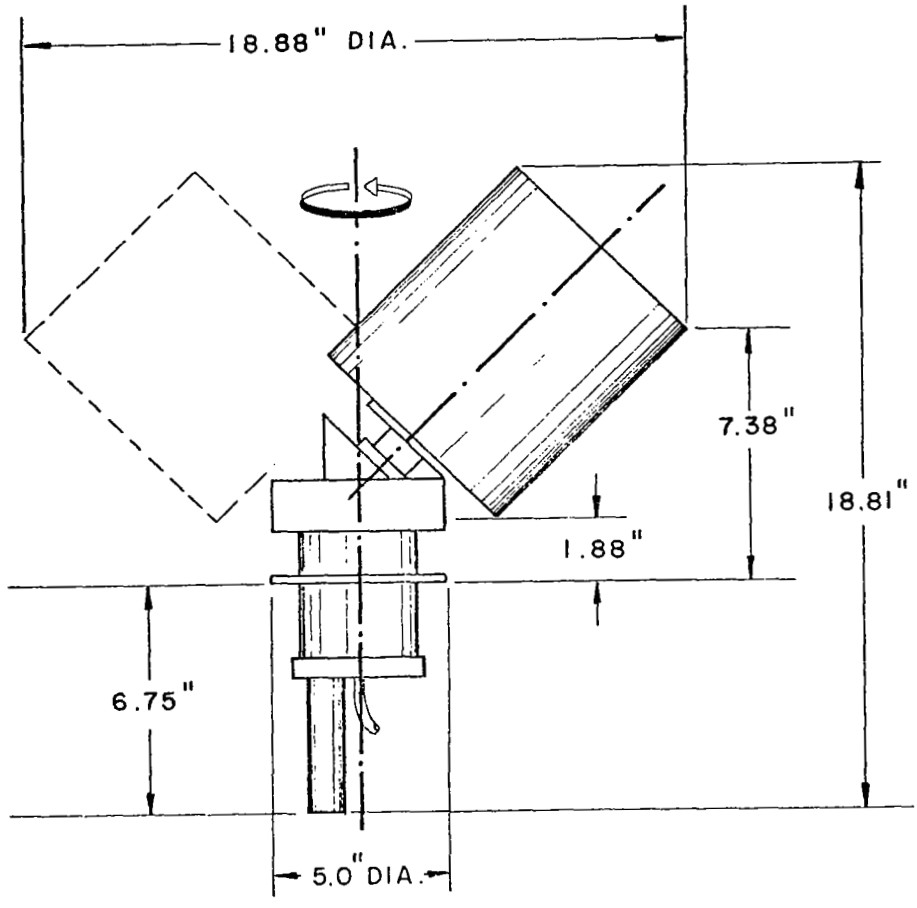

Figure 27: Space Envelope of Celestial Scanner.

Figure 28 illustrates the threshold crossings of the noise-free star signal and the star signal with superimposed noise. The leading edge threshold crossing of the noise-free signal occurs at time T_a and its trailing edge crossing occurs at T_b. Superimposing random noise on the noise-free signal causes a random time error, t_1, in the leading edge threshold crossing. The leading edge threshold crossing of the noisy star pulse then becomes a random variable

$$T_1 = t_1 + T_a.$$

Similarly, random noise causes a random time error, t_2, in the trailing edge threshold crossing time, so the trailing edge threshold crossing of the noisy star pulse becomes a random variable

$$T_2 = t_2 + T_b. \tag{47}$$

Since the average of the threshold crossing times defines the star pulse transit time, $t_s = \frac{1}{2}(T_1 + T_2)$, the variance of the transit time is given by

$$\sigma^2(t_s) = E\left[\frac{T_1 + T_2}{2} - \frac{T_a + T_b}{2}\right]^2 \tag{48}$$

$$= E\left[\frac{t_1 + t_2}{2}\right]^2$$

$$= \tfrac{1}{4}\overline{t_1^2} + \tfrac{1}{4}\overline{t_2^2} + \tfrac{1}{2}\overline{t_1 t_2}\ .$$

From figure 28 the slope of the noise-free signal in the vicinity of T_a is given by $+ k_1$, and the slope of the noise-free signal in the vicinity of T_b is given by $- k_2$. At the leading edge threshold crossing of the noisy star pulse, the noise amplitude is given by random variable I_1, so the random time error in the leading edge threshold crossing time is given by

$$t_1 = -\frac{I_1}{k_1}\ .$$

Then, the variance of the leading edge crossing time is given by

$$\sigma^2(t_1) = \overline{t_1^2} = \frac{1}{k_1^2}\,\overline{I_1^2}\ . \tag{49}$$

Similarly, at the trailing edge threshold crossing the noise amplitude is given by random variable I_2, so the random time error in the trailing edge threshold crossing is given by

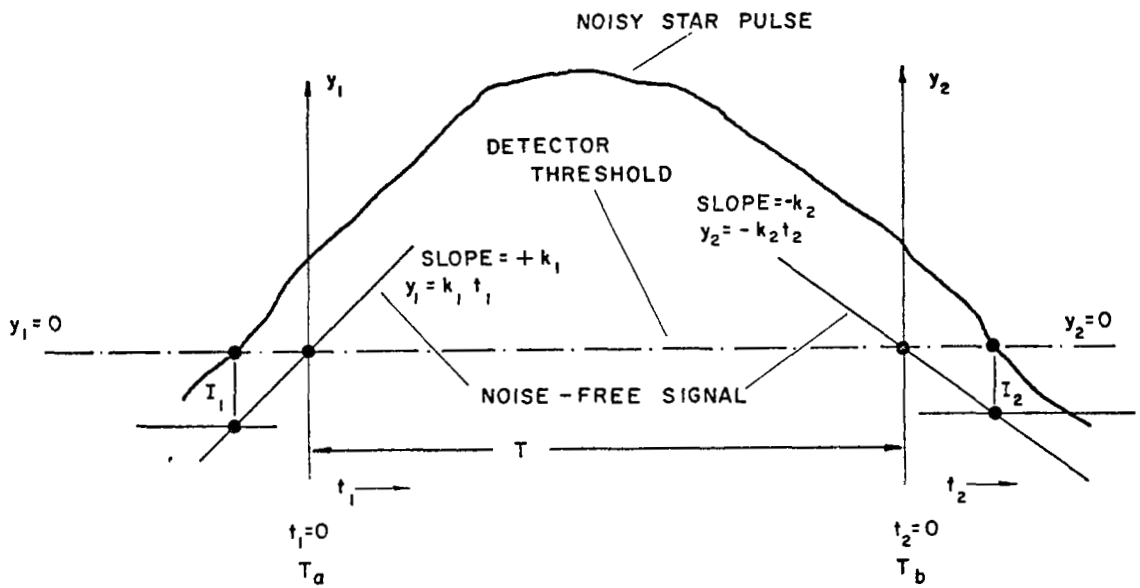

Figure 28: Star pulse threshold crossings.

$$t_2 = \frac{I_2}{k_2} .$$

The variance of the trailing edge crossing time is then given by

$$\sigma^2 (t_2) = \overline{t_2^2} = \frac{\overline{I_2^2}}{k_2^2} . \tag{50}$$

Also, the covariance of the threshold crossing times is given by

$$\overline{t_1 t_2} = - \frac{1}{k_1 k_2} \overline{I_1 I_2} \tag{51}$$

Substituting into equation (48), the transit time variance becomes

$$\sigma^2 (t_s) = \frac{\overline{I_1^2}}{4k_1^2} + \frac{\overline{I_2^2}}{4k_2^2} - \frac{\overline{I_1 I_2}}{2k_1 k_2} . \tag{52}$$

From the definition of the correlation coefficient for random noise amplitudes I_1 and I_2,

$$\rho_{12} = \frac{\overline{I_1 I_2}}{\sqrt{\overline{I_1^2}} \sqrt{\overline{I_2^2}}}$$

so

$$\sigma^2 (t_s) = \frac{\overline{I_1^2}}{4k_1^2} + \frac{\overline{I_2^2}}{4k_2^2} - \rho_{12} \frac{\sqrt{\overline{I_1^2}\ \overline{I_2^2}}}{2k_1 k_2} . \tag{53}$$

If the statistics of the noise amplitudes at time T_b are the same as the noise amplitudes at T_a, then

$\overline{I_1^2} = \overline{I_2^2} = \overline{I^2}$ and equation (53) becomes

$$\sigma^2 (t_s) = \frac{\overline{I^2}}{2} \left(\frac{1}{2k_1^2} + \frac{1}{2k_2^2} - \frac{\rho_{12}}{k_1 k_2} \right) \tag{54}$$

In addition, if the star pulse is symmetrical, then the magnitude of the slope for the noise-free signal at the trailing edge equals the slope at the leading edge. Thus, $k_1 = k_2 = k$ and equation (54) becomes

$$\sigma^2 (t_s) = \frac{\overline{I^2}}{2k^2} (1 - \rho_{12}) . \tag{55}$$

This result is given without proof by Mityashev in reference 14.

For the above analysis, the slope of the noise-free pulse is assumed constant in the neighborhood of the threshold crossings, whereas, the slope of the noisy pulse is not necessarily constant in those regions. The former assumption is valid since the noise-free filter input signal is a well behaved deterministic function of time. Although the slope of the noisy pulse may be changing in the region of the threshold crossings, it is assumed that the noisy signal is monotone increasing in the neighborhood of the leading edge threshold crossing and monotone decreasing in the neighborhood of the trailing edge threshold crossing. This restriction is realized for signals having relatively high peak signal-to-RMS noise ratios. Peak signal-to-RMS noise ratios of five to one or greater are necessary in order to set a threshold which yields an acceptable false alarm rate and a high detection probability given that the star signal is present ($P_d | S \geq .9$). This also insures that the constant slope assumption of the noise-free signal is valid for all noise amplitudes except for the very infrequent large amplitudes.

Equation (55) tends to become more and more invalid as the threshold setting closely approaches the peak of the star pulse. Right at the pulse peak, equation (55) becomes indeterminant since $\rho_{12} = 1$ and $k = 0$.

A typical (noise-free) star signal from the output of the filter used for the celestial sensor analysis is plotted in figure 23. In order to evaluate equation (55) for the output of filter F_1, determination of the correlation coefficient, ρ_{12}, of the noise for the interval between the leading and trailing edge threshold crossings is required. This can be done by applying Campbell's theorem (reference 15). So

$$\rho(\tau) = \frac{\int_0^\infty h(t)\, h(t + \tau)\, dt}{\int_0^\infty h^2 (t)\, dt} \tag{56}$$

For a threshold set at 60% of the peak of $y_1 (t)$, $\tau = 15.5 \times 10^{-3}$ seconds.

Evaluating equation (56) by numerical integration for the four-pole linear phase transfer function of filter F_1,

$$\rho_{12} = 0.079.$$

The slope of the output from F_1 is given by

$$\frac{d}{dt}\left[y_1(t)\right] = \int_0^\infty f(\tau)\,\frac{d}{dt}\left[h(t-\tau)\right]d\tau. \tag{57}$$

Numerical integration of equation (57) gives at 60% of the peak

$$\frac{d}{dt}\left[y_1(t)\right] = 61.5 = k \tag{58}$$

Since the slope of the output signal $y_1(t)$ is proportional to the peak value of the signal,

$$\frac{k_p}{k} = \frac{I_p}{0.76}\,. \tag{59}$$

So

$$k_p = \frac{61.5}{0.76}\,I_p = 81\,I_p \tag{60}$$

and

$$\sigma^2(t_s) = \frac{\overline{I_N^{\,2}}}{2(81I_p)^2}\,(1 - 0.08). \tag{61}$$

So

$$\sigma(t_s) = \frac{0.836 \times 10^{-2}}{\left(S/_N\right)} \tag{62}$$

where

$$\frac{I_p^{\,2}}{I_N^{\,2}} = \left(S/_N\right)^2\,. \tag{63}$$

The calculated signal-to-noise ratio at the output of filter F_1 for a 0.5 inch aperture and a 2nd magnitude star when the scan period is 60 seconds (page 78) is

$$S/_N = 21.1. \tag{64}$$

So,

$$\sigma(t_s) = 3.96 \times 10^{-4} \text{ seconds.}$$

Since $T_s = 10.55 \times 10^{-3}$ seconds for a 3.8 arc minute slit width and a 60 second scan period,

$$\frac{T_s}{\sigma(t_s)} = \frac{10.55 \times 10^{-3}}{3.96 \times 10^{-4}} = 26.5.$$

Angle Encoder Resolution

A star transit is equally likely to occur at any angular position, x, between angle encoder marker pulses. If the angular spacing between adjacent angle encoder marker pulses is L, then the probability density for a star transit occurring within the angular interval

$$-\frac{L}{2} \leq x \leq +\frac{L}{2}$$

is given by

$$p(x) = \frac{1}{L}.$$

The mean square value of the random variable x with zero mean is

$$\overline{x^2} = \int_{-L/2}^{+L/2} x^2 \, p(x) \, dx$$

$$= \frac{1}{L} \frac{x^3}{3} \Bigg|_{-L/2}^{+L/2}$$

$$= \frac{1}{3} \frac{L^2}{4}$$

$$= \left(\frac{L}{\sqrt{12}}\right)^2$$

But from equation (40) the RMS value of the angle encoder quantization error is required to be

$$\Delta = 22.7 \text{ arc seconds}$$

for a well balanced distribution of allowable errors. So

$$L = \sqrt{12}\ (22.7)$$

$$= 82.9 \text{ arc seconds}$$

$$= 1.38 \text{ arc minutes}$$

$$\cong 360 \text{ degrees} \times 2^{-14}$$

Consequently, fourteen bits of angle encoder resolution are sufficient.

Approximate Estimate of Geometric Errors for Moon Detections

The center of the scanned field of view is directly opposite the sun. Therefore, the terminator of the moon of Mars will always be symmetrical with respect to a line drawn from the anti-solar point to the center of the moon as in figure 29.

If the detection scheme utilizes the average of the leading and trailing edge threshold crossings, then there is no geometric error for the center since the signal is symmetrical; but asymmetric pulses are expected from the two side slits. Therefore, a transit time error due to purely geometric causes will result. A rough approximation of this error will be derived in the following discussion.

Figure 30 shows an outline of the image of the moon as seen in the focal plane of the sensor optics. The moon is illuminated by the sun at some arbitrary phase angle, $\bar{\varphi}$, between the sensor-moon vector and the moon-sun vector. The top half of the moon image outline is a circle, whereas, the bottom half of the moon image outline is an ellipse because of the phase angle. Now, a slit tilted at an angle θ with respect to the vertical which moves horizontally to the left in the figure will intersect a circle on the leading edge of the moon image and will intercept an ellipse on the trailing edge of the moon image. In between these two extremes, the radiant power passing through the slit will be proportional to the length of the slit intercepted by the image if the illumination within the image is uniform. The slit output versus slit position is qualitatively plotted in figure 30. Passing a threshold through the slit output characteristic and averaging the threshold crossing permit qualitative determination of the geometric moon detection error versus horizontal slit position as shown in figure 30. The detection error characteristic shows that the error is smallest when the threshold setting is the lowest. The threshold crossing for small (compared to the signal peak) threshold levels may be determined by considering the geometry in figure 30.

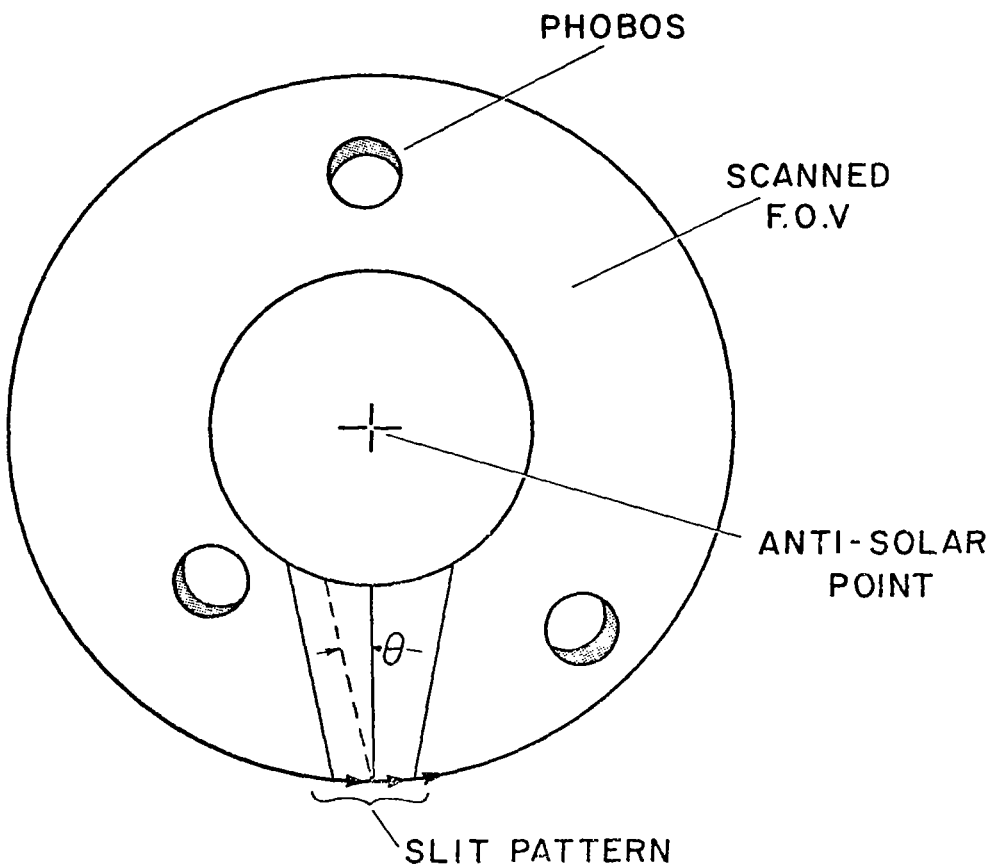

Figure 29: Scanning Mars moon with reticle.

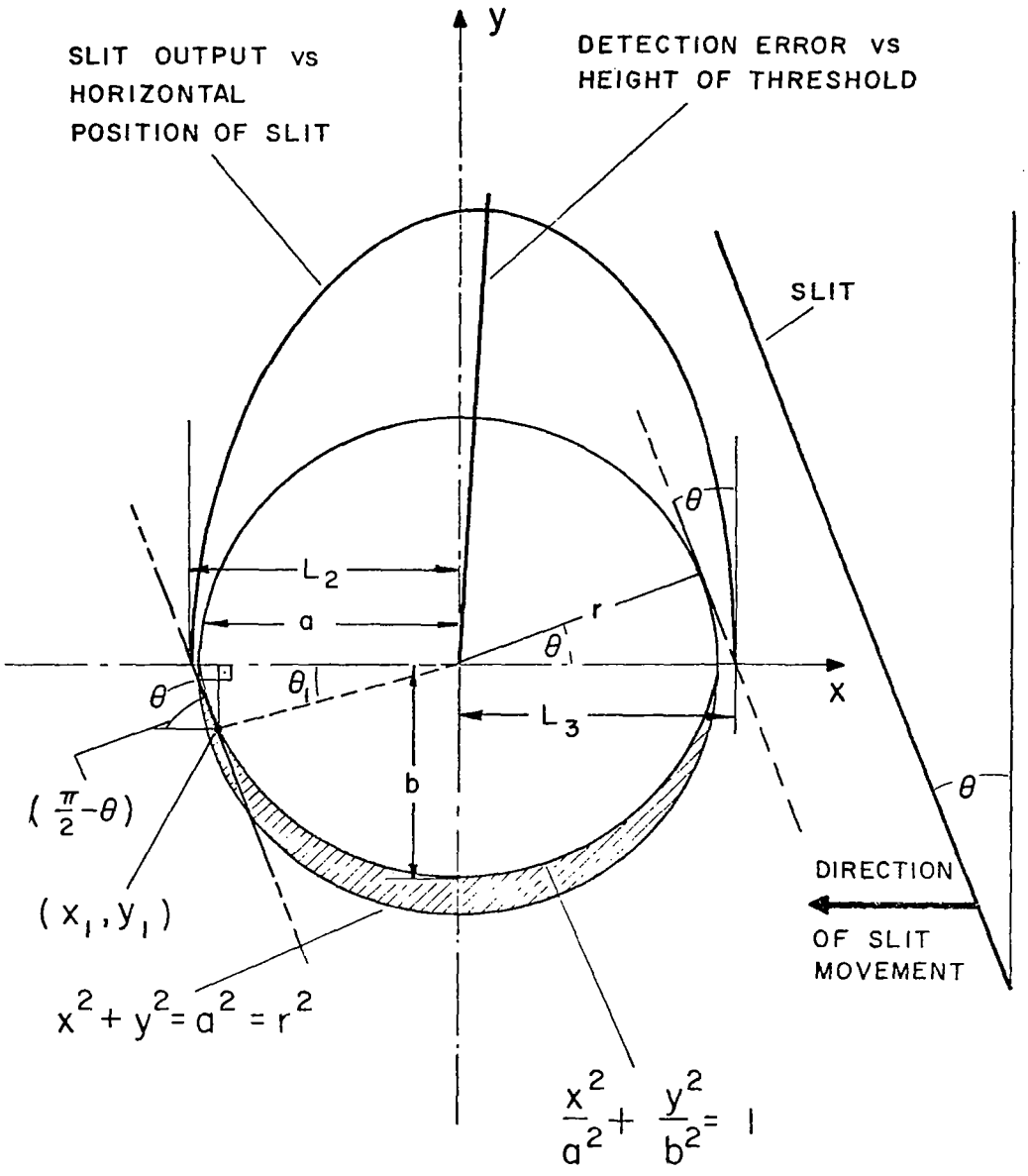

Figure 30: Slit scanning of moon image as seen in focal plane of sensor.

If

R the moon radius

D the distance from spacecraft to moon,

then the angle subtended by the moon radius from the spacecraft is

$$\phi = \frac{R}{D} \cdot \tag{65}$$

Now, if

r = radius of the semi-circle defining the top part of the moon image in figure 30

F = focal length of the optics,

then

$$\frac{r}{F} \doteq \phi \ . \tag{66}$$

Therefore, the distance L_3 in figure 30 is

$$\frac{r}{L_3} = \cos \theta \tag{67}$$

or

$$L_3 = \frac{r}{\cos \theta} = \phi F \sec \theta \ . \tag{68}$$

In order to determine L_2, it is necessary to determine the lengths of the major and minor axes of the ellipse. If

a = the ellipse major axis length

b = the ellipse minor axis length

then,

$$a = r = \phi F.$$

The minor axis length is given by

$$\frac{b}{F} = \frac{R \cos \xi}{D}$$

where R cos ξ is a projection of the moon terminus onto a plane normal to the sensor-moon vector and

$$\frac{R \cos \Phi}{D}$$

is the angle subtended from the sensor by this projection.

The equation for the ellipse is

$$\frac{x^2}{a^2} + \frac{y^2}{b^2} = 1. \tag{69}$$

The slope of the tangent to the ellipse at point (x_1, y_1) is given by

$$\frac{dy}{dx} = \pm \frac{b}{a^2} \frac{x_1}{\left[1 - \left(\frac{x_1}{a}\right)^2\right]^{\frac{1}{2}}} \tag{70}$$

But from figure 30, this slope must equal

$$\begin{aligned} - \tan \left(\frac{\pi}{2} - \theta\right) &= k^{\frac{1}{2}} \\ &= - \cot \theta \\ &= \frac{-1}{\tan \theta} \quad . \end{aligned} \tag{71}$$

Equating equations (70) and (71) yields

$$x_1^2 \left(\frac{b}{a^2}\right)^2 = k - \frac{k}{a^2} x_1^2 \tag{72}$$

$$x_1 = \pm \left[\frac{k}{\left(\frac{b}{a^2}\right)^2 + \frac{k}{a^2}} \right]^{\frac{1}{2}} \tag{73}$$

Substituting equation (73) into equation (69) gives

$$\frac{y_1}{b} = \pm \left[\frac{\left(\frac{b}{a}\right)^2}{\left(\frac{b}{a}\right)^2 + k} \right]^{\frac{1}{2}} \tag{74}$$

From figure 30

$$L_1 = x_1 + y_1 \tan \theta. \tag{75}$$

But from equations (71), (73), and (74)

$$x_1 = \left[\frac{a^4}{a^2 + b^2/k} \right]^{\frac{1}{2}} \tag{76}$$

$$= \frac{a^2}{\left[a^2 + b^2 \tan^2 \theta \right]^{\frac{1}{2}}}$$

$$y_1 = b \left[\frac{b/k}{a^2 + b^2/k} \right]^{\frac{1}{2}} \tag{77}$$

$$= \frac{b^2 \tan \theta}{\left[a^2 + b^2 \tan^2 \theta \right]^{\frac{1}{2}}} .$$

So since

$$\frac{b}{a} = \cos \bar{\varphi}, \tag{78}$$

$$L_2 = \frac{a^2 + b^2 \tan^2 \theta}{\left[a^2 + b^2 \tan^2 \theta \right]^{\frac{1}{2}}}$$

$$= a \left[1 + \cos^2 \bar{\varphi} \tan^2 \theta \right]^{\frac{1}{2}}.$$

The angle error for low thresholds is

$$\epsilon_a = \frac{(L_3 - L_2)}{2F} . \tag{79}$$

So, combining equations (68) and (80) gives the angle error as

$$\epsilon_a = \frac{1}{2F} \left\{ \phi F \sec \theta - \phi F \left[1 + \cos^2 \bar{\varphi} \tan^2 \theta \right]^{\frac{1}{2}} \right\} \tag{80}$$

$$\epsilon_a = \frac{\phi}{2}\left\{\sec\theta - \left[1 + \cos^2\Phi \tan^2\theta\right]^{\frac{1}{2}}\right\} \quad .$$

The phase angle Φ can range from 35° to 55° and $\phi \leq \frac{1}{2}$ degree. For $\Phi = 35^\circ$, and

$$\phi = \frac{1^\circ}{2},$$

equation (80) becomes

$$|\epsilon_a| = 18.6 \text{ arc seconds.}$$

For $\Phi = 55^\circ$, $\theta = 20^\circ$ and $\phi = \frac{1^\circ}{2}$

$$|\epsilon_a| = 38.3 \text{ arc seconds.}$$

In general, a difficulty exists in this approximation for if the distance to the moon is not known, then the angle subtended, ϕ, is not known. However, a procedure may be used which initially neglects the geometric errors in computing the approximate orbits. These approximate orbits are then used to compute the distance to the moon from the spacecraft. Then, the geometric corrections may be included to calculate new orbits which should yield a suitably accurate solution.

Refined Analytical Model for Determining Moon Transit Correction Factors

In order to compute the trajectories of the moons of Mars from data provided by a scanning celestial sensor, it is required that transit data be obtained for those moons as the scanning slits intercept the images of the moons formed by the sensor optics. The accuracy of the trajectory computations depends on the accuracy of the slit transit measurements provided by the sensor. But since the slit transit measurements are determined by threshold detection of the signal generated by the photodetector as the slit scans over the image of the moon, the accuracy of the signal in turn depends upon the phase angle between the moon-sun vector and the moon-spacecraft vector, the relative dimensions of the moon diameter, distance of the spacecraft from the moon and the width of the slit gap. The signal shape also depends upon the sensor orientation on the spacecraft and the slit orientation in the sensor. Because the primary function of the celestial sensor instrumentation is to accurately locate the moons of Mars, it is worthwhile to calculate the signal generated by the radiant power passing through a slit scanning a moon body from which estimates can be made in the uncertainties of the moon transit data. Also, it should be possible to determine correction factors which can be applied to the moon transit data. Because of the complexity of the problem, the solution will have to be obtained numerically. Only the method of computation is outlined.

The method of solution will be an extension of the analysis described in reference 16. The problem will be formulated by projecting the slit gap on the surface of the moon and then summing (numerically integrating) the radiant power reflected from each elemental area of the moon's surface which is not blocked by the projected slit mask. The geometry illustrating the vector relationships between sun, spacecraft, and elemental area within the slit that is projected on the moon surface is illustrated in figure 31. The projection of the slit on the surface of the moon can be determined by the intersection of the moon surface with a plane containing the slit and a point which represents the optical system center. In figure 31, it is assumed that axis k_o is normal to the plane containing the slit. The unit vector from the moon center to the sun is represented by $\vec{S}$ and the vector from the moon center to the spacecraft position is represented by $\overline{C}$. The radius vector from the moon center to the elemental area on the moon surface is represented by $\overline{R}$. If L is the solar constant at the mean solar distance of the moon, then the radiant power incident on a unit elemental area of the moon's surface is given by

$$L \frac{\overline{R} \cdot \vec{S}}{|\overline{R}|} \frac{\text{watts}}{(\text{cm})^2} \tag{81}$$

Note that the incident radiant power is zero if $\overline{R} \cdot \vec{S} \leq 0$.

The elemental area shown on the surface of the moon in figure 31 is given by

$$dA = ds_1 \cdot ds_2 \tag{82}$$

where

$$ds_1 = R \cos \nu d\phi$$

$$ds_2 = R \, d\nu$$

$$R = |\overline{R}| .$$

The elemental angle, $d\nu$, is determined by the angle subtended by the slit gap, $\widehat{s\omega}$. Figure 32 shows the geometry when viewed in the plane of vectors $\overline{R}$ and $\overline{C}$ when $\phi = \alpha$. The distance at the surface of the moon subtended by the angular slit width is given by

$$w = \widehat{s\omega} \, |\overline{G}| . \tag{83}$$

The vector $\overline{G}$ is the vector from the spacecraft to the elemental area on the moon surface and given by $\overline{G} = \overline{R} - \overline{C}$. (84)

The distance w when projected normal to $\overline{R}$ is given by

$$x = \frac{w}{\cos \varepsilon} \tag{85}$$

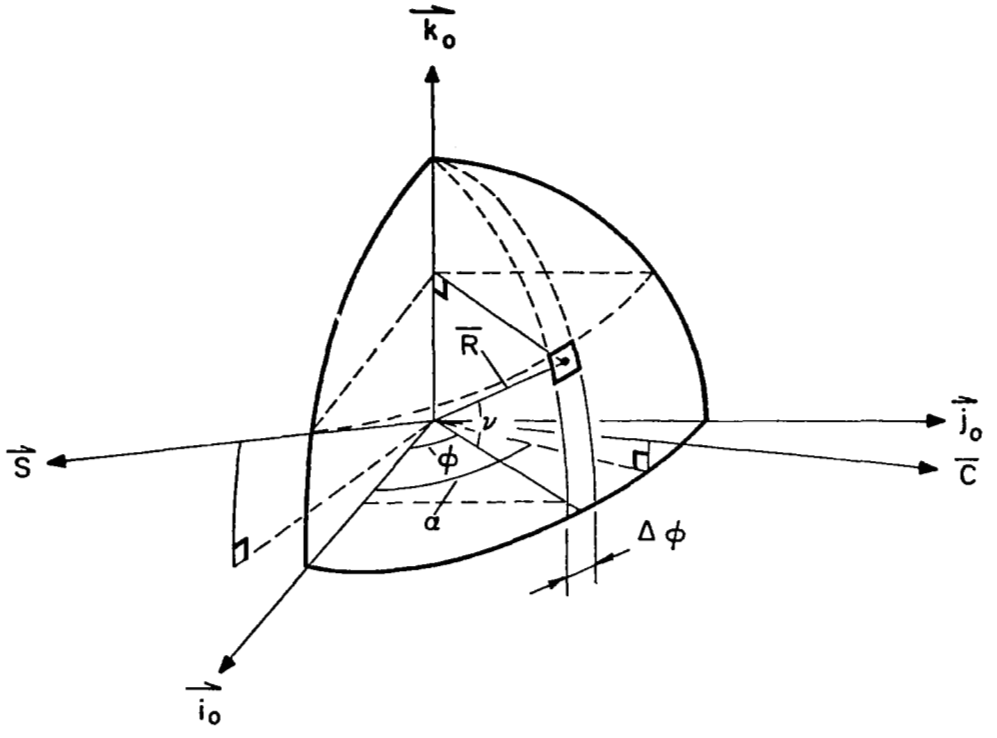

Figure 31: Sun and spacecraft vectors in coordinate system of moon.

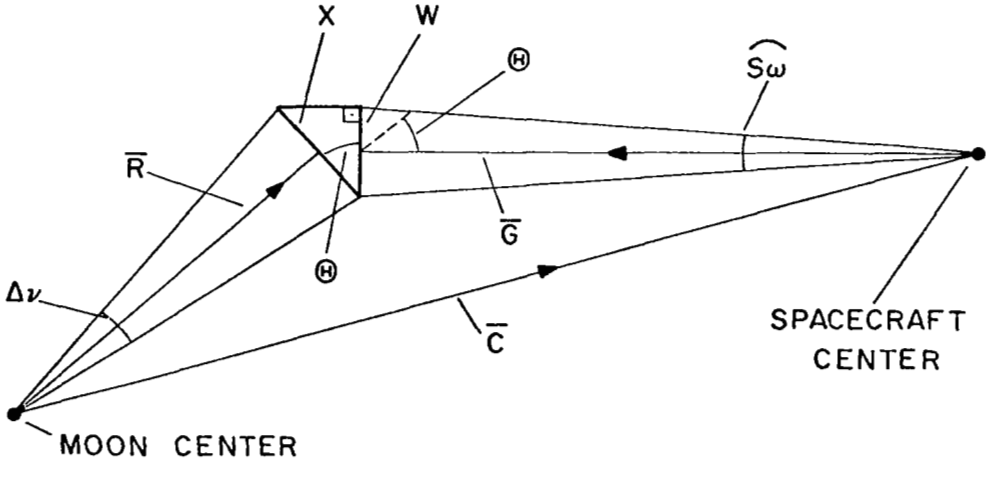

Figure 32: Angles subtended by elemental angles on moon's surface.

where

$$\cos \Theta = - \frac{\bar{R} \cdot \bar{G}}{|\bar{R}| \, |\bar{G}|} .$$

So,

$$d\nu = \frac{x}{|\bar{R}|} = - \frac{\widehat{s\omega} \, |\bar{G}|^2}{\bar{R} \cdot \bar{G}} \tag{86}$$

The moon albedo is defined as

$$a = \frac{\text{total reflected energy}}{\text{total incident energy}} \tag{87}$$

which is assumed to be wavelength invariant.

The radiant power reflected per steradian in the direction specified by angle θ is given by reference 17 (p. 185) where

$$J_o = \frac{P}{\pi} \cos \theta \, \frac{\text{reflected watts}}{\text{steradian}} \tag{88}$$

where

P = total power radiated into the hemisphere

θ = angle measured from normal to surface area.

Therefore, the radiant power reflected in the direction of the spacecraft is given by

$$L \, \frac{\bar{R} \cdot \vec{S}}{|\bar{R}|} \, \frac{\text{incident watts}}{(\text{cm})^2} \cdot dA \, (\text{cm})^2 \cdot a \cdot \frac{\cos \Theta}{\pi} \, (\text{steradian})^{-1} \tag{89}$$

Since an area, A_c, located at the spacecraft, which is a distance $|\bar{G}|$ from the elemental area on the moon surface, intercepts

$$\frac{A_c}{|\bar{G}|^2}$$

steradians, the radiant power reflected from the elemental area on the moon's surface which illuminates an area A_c at the spacecraft is given by

$$dH = L \, \frac{\bar{R} \cdot \vec{S}}{|\bar{R}|} \cdot dA \cdot a \, \frac{\cos \Theta}{\pi} \, \frac{A_c}{|\bar{G}|^2} \tag{90}$$

$$dH = \frac{aL}{\pi} A_c \frac{\bar{R} \cdot \vec{S}}{|\bar{G}|} \widehat{s\omega} \cos \nu d\phi \text{ watts} .$$

The total radiant power reflected by the moon through the sensor slit is given by

$$H \doteq \frac{aL}{\pi} A_c \sum_{0 \leq \phi \leq 2\pi} \frac{(\bar{R} \cdot \vec{S})}{|\bar{G}|} \widehat{s\omega} \cos \nu \Delta\phi . \tag{91}$$

In general, the angle subtended by the slit gap for scanning star sensors will always be small, i.e.,

$$\widehat{s\omega} \leq 1 \text{ degree.}$$

So, the small angle approximation for w in equation (83) is valid. However, when $|\bar{C}|$ becomes sufficiently larger than $|\bar{R}|$, $d\nu$ in equation (86) may become sufficiently large so the error due to small angle approximation is not negligible. Figure 33 illustrates a technique for providing a better approximation for equation (91). The distance w is subdivided into an integral number of increments Δw, such that the corresponding increments $\Delta\nu$ are sufficiently small to yield a good small angle approximation. The radius vector $\bar{R}$ is at a nominal angle, ν, with respect to the $\vec{i} - \vec{j}$ plane, so

$$\Delta x_1 = \frac{\Delta w}{\cos \Theta} , \tag{92}$$

but

$$\Delta \nu_1 = \frac{\Delta x_1}{R} . \tag{93}$$

Now, let

$$\nu_1 = \nu + \Delta \nu_1 \tag{94}$$

and let $\bar{R}_1$ be the radius vector at the new position determined by ν_1. Then

$$\Delta x_3 = \frac{\Delta w}{\cos \Theta_1} \tag{95}$$

$$\cos \Theta_1 = \frac{\bar{R}_1 \cdot \bar{G}}{|\bar{R}_1||\bar{G}|} \tag{96}$$

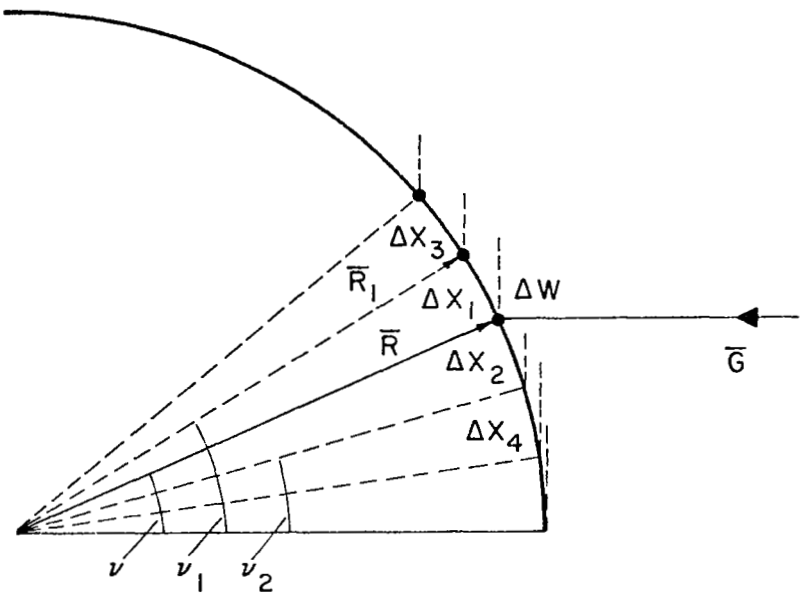

Figure 33: Improved approximation for large angles of $d\nu$.

$$\Delta\nu_3 = \frac{\Delta x_3}{R} \tag{97}$$

$$\nu_3 = \nu_1 + \Delta\nu_3 \tag{98}$$

.
.
.
.
etc.

Similarly, in the negative ν direction

$$\Delta x_2 = \frac{\Delta w}{\cos \Theta} \tag{99}$$

$$\Delta\nu_2 = \frac{\Delta x_2}{R} \tag{100}$$

$$\nu_2 = \nu - \Delta\nu_2 \tag{101}$$

$$\Delta x_4 = \frac{\Delta w}{\cos \Theta_2} \tag{102}$$

$$\Delta\nu_4 = \frac{\Delta x_4}{R} \tag{103}$$

$$\nu_4 = \nu_2 - \Delta\nu_4 \tag{104}$$

.
.
.
.
etc.

Incorporating equations (92) through (104), etc., into equation (90) yields a double summation given by

$$H = A_c \frac{aL}{\pi} \sum_{\nu} \sum_{\phi} (\bar{R}_i \cdot \vec{S}) \frac{\left(-\bar{R}_i \cdot \bar{G}\right)}{|\bar{G}|^3} \cos \nu_i \, \Delta\nu_i \, \Delta\phi \tag{105}$$

The $\bar{R}_i$ used in determining cos Θ_i may be computed from $\vec{R}$ and $\Delta\nu_i$.

Since

$$\bar{R} = |\bar{R}| \ (\vec{X} \cos \nu + \sin \nu \ \vec{k}) \tag{106}$$

$$\vec{X} = \left(\frac{\bar{R}}{|\bar{R}|} - \sin \nu \ \vec{k} \right) \ \frac{1}{\cos \nu}, \tag{107}$$

but

$$\bar{R}_i = |\bar{R}| \ \{\vec{X} \cos (\nu \pm \Delta\nu_i) + \sin (\nu \pm \Delta\nu_i) \ \vec{k}\} \tag{108}$$

so the new vector $\bar{R}_i$ is determined by substitution of equation (107) into equation (108).

For evaluation of equations (91) or (105), it will be assumed the phase angle between the sun vector and the moon-spacecraft vector is known or has been previously determined. Also assumed known is the distance from the moon-center to the spacecraft, the optical system field of view, the optical system focal length, the cant angle of the optical axis with respect to the spin axis, the pointing direction of the spin axis and the orientation of the slit gap in the focal plane. Since equations (91) and (105) were derived with the k_o axis normal to the plane containing the slit, it will be necessary to orient the sun, spacecraft and optical axis so all the known parameter conditions are satisfied when the k_o axis is normal to the plane containing the slit. The proper orientation can be derived by a suitable series of coordinate transformations.

Figure 34 shows the sun vector coincident with the negative $\vec{j}_1$ axis and the moon-spacecraft vector lying in the $\vec{i}_1 - \vec{j}_1$ plane at a phase angle $\bar{\varphi}$ with respect to the sun vector. If the distance between the moon-center and the spacecraft is D, the moon-spacecraft vector is

$$\bar{C} = (\sin \bar{\varphi} \ \vec{i}_1 - \cos \bar{\varphi} \ \vec{j}_1) \ D. \tag{109}$$

Figure 34 shows the spacecraft coordinate axes, $(\vec{i}_2 - \vec{j}_2 - \vec{k}_2)$, at the tip of the moon-spacecraft vector $\bar{C}$. The spacecraft coordinate system is assumed to have the same orientation as the $\vec{i}_1 - \vec{j}_1 - \vec{k}_1$ system, hence

$$\begin{pmatrix} \vec{i}_2 \\ \vec{j}_2 \\ \vec{k}_2 \end{pmatrix} = \begin{pmatrix} 1 & 0 & 0 \\ 0 & 1 & 0 \\ 0 & 0 & 1 \end{pmatrix} \begin{pmatrix} \vec{i}_1 \\ \vec{j}_1 \\ \vec{k}_1 \end{pmatrix} \tag{110}$$

The vehicle spin axis is chosen coincident with the $\vec{j}_2$ vector, which is equivalent to the negative sun vector.

A third coordinate system is defined by a rotation about the $\vec{j}_2$ axis (vehicle spin axis). Hence, for a clockwise rotation about the $\vec{j}_2$ axis, the

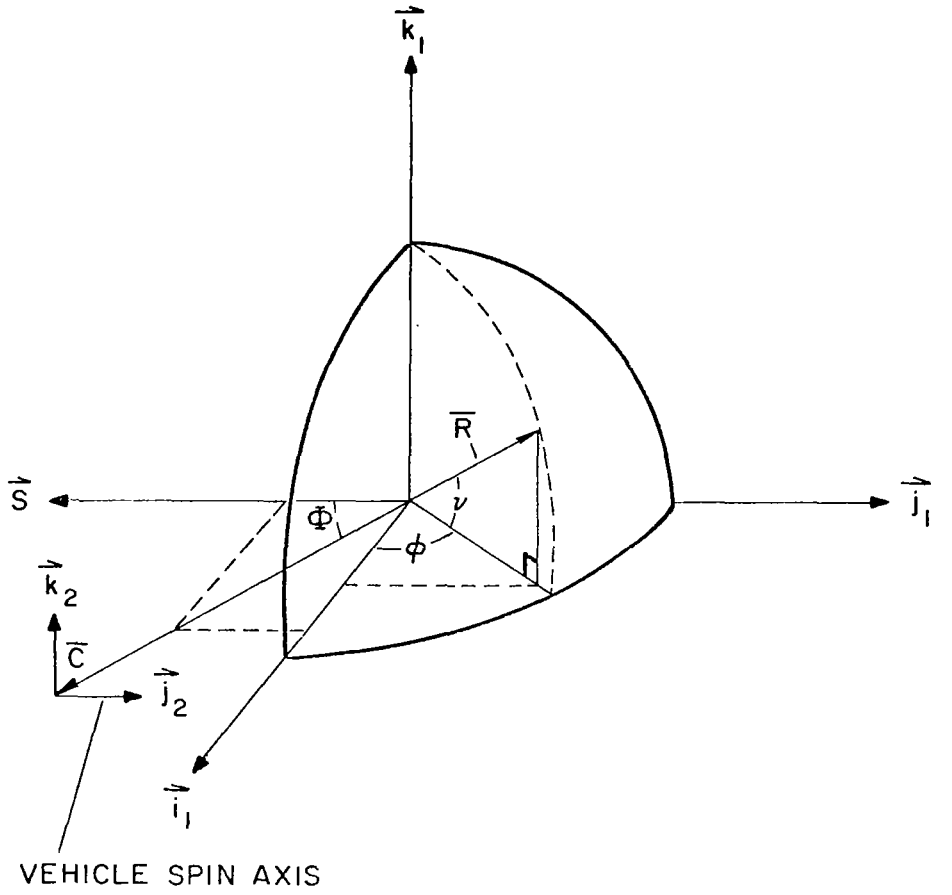

Figure 34: Phase angle between sun vector and moon spacecraft vector.

$\vec{i}_3 - \vec{j}_3 - \vec{k}_3$ coordinate system orientation becomes

$$\begin{pmatrix} \vec{i}_3 \\ \vec{j}_3 \\ \vec{k}_3 \end{pmatrix} = \begin{pmatrix} \cos \omega & 0 & \sin \omega \\ 0 & 1 & 0 \\ -\sin \omega & 0 & \cos \omega \end{pmatrix} \begin{pmatrix} \vec{i}_2 \\ \vec{j}_2 \\ \vec{k}_2 \end{pmatrix} \tag{111}$$

Figure 35 shows the optical axis lying in the $\vec{i}_3 - \vec{j}_3$ plane canted at an angle Γ with respect to spin axis $\vec{j}_3$ ($\vec{j}_2$). Now, let $\bar{F}$ represent a vector from the $\vec{i}_3 - \vec{j}_3$ origin to the optical system focal plane,

$$\bar{F} = F (-\sin \Gamma \vec{i}_3 - \cos \Gamma \vec{j}_3) \tag{112}$$

where

F = focal length of the optical system.

Next, let the vector $\bar{d}$ lie in the $\vec{i}_3$ plane and intersect with the focal plane such that the vector extends from the edge of the field of view to the center of the focal plane.

$$d = d (\cos \Gamma \vec{i}_3 - \sin \Gamma \vec{j}_3) = d_1 \vec{i}_3 + d_2 \vec{j}_3 \tag{113}$$

where

$$d = F \tan \left(\frac{FOV}{2}\right).$$

The vector $\bar{d}$ is coincident with the slit which is radial to the spin axis.

In order to specify the direction of the slits which are non-radial to the vehicle spin axis, it is necessary to generate another set of coordinate axes, $\vec{i}_4 - \vec{j}_4 - \vec{k}_4$. From figure 35, let

$$\bar{M} = \bar{F} - \bar{d} \tag{114}$$

$$= \vec{i}_3 F \left[-\sin \Gamma - \tan \left(\frac{FOV}{2}\right) \cos \Gamma\right] + \vec{j}_3 F \left[-\cos \Gamma + \tan \left(\frac{FOV}{2}\right) \sin \Gamma\right]$$

$$= m_1 \vec{i}_3 + m_2 \vec{j}_3.$$

Now, define the cross product of vectors $\bar{M}$ and $\bar{d}$ as

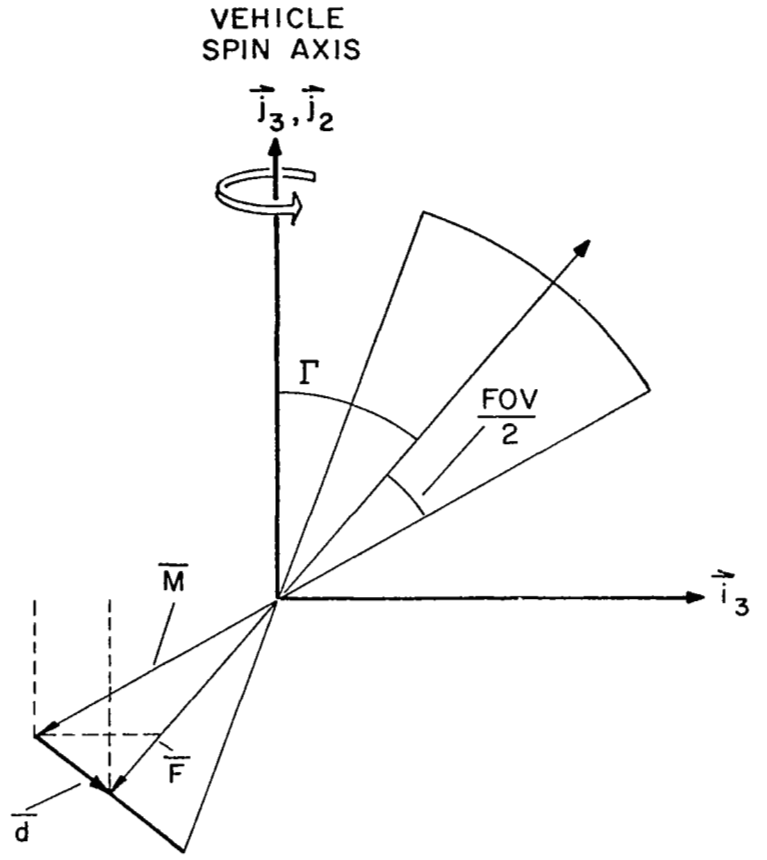

Figure 35: Orientation of optical system in spacecraft

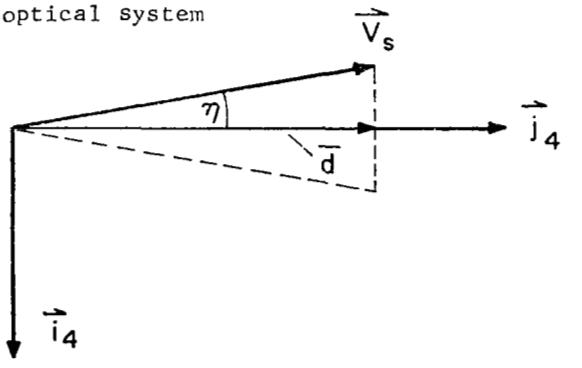

Figure 36: Orientation of sensor slit(s) in focal plane

$$\vec{i}_4 = \frac{1}{|\bar{d}|\,|\bar{M}|\,\sin\,\cos^{-1}\dfrac{(\bar{d}\cdot\bar{M})}{|\bar{d}|\,|\bar{M}|}} \begin{vmatrix} \vec{i}_3 & \vec{j}_3 & \vec{k}_3 \\ m_1 & m_2 & 0 \\ d_1 & d_2 & 0 \end{vmatrix} \tag{115}$$

and let

$$\vec{j}_4 = \frac{\bar{d}}{|\bar{d}|} = (\cos\Gamma \;\vdots\; -\sin\Gamma \;\vdots\; 0) \begin{pmatrix} \vec{i}_3 \\ \vec{j}_3 \\ \vec{k}_3 \end{pmatrix} \tag{116}$$

So,

$$\vec{k}_4 = \vec{i}_4 \times \vec{j}_4.$$

Figure 36 shows the $\vec{i}_4$- $\vec{j}_4$ plane or focal plane of the sensor optics. Now, let the unit vector $\vec{V}_s$ coincide with the slit being considered

$$\vec{V}_s = \sin\eta\,\vec{i} + \cos\eta\,\vec{j}_4 = (-\sin\eta \;\vdots\; \cos\eta \;\vdots\; 0) \begin{pmatrix} \vec{i}_4 \\ \vec{j}_4 \\ \vec{k}_4 \end{pmatrix} \tag{117}$$

The slit which is radial to the vehicle spin axis is designated by $\eta = 0$ and the non-radial slits are designated by $\eta \neq 0$.

The plane containing the slit is defined by the vectors $\vec{V}_3$ and $\bar{M}$., so the slit starts to intersect the image of the moon in the optical system focal plane when the plane containing the slit is tangent to the moon. The plane containing the slit is completely defined by the normal, $\vec{n}$, to that plane given by the cross product of $\vec{V}_s$ and $\bar{M}$.

$$\vec{n} = \frac{1}{|\vec{V}_s|\,|\bar{M}|\,\sin\left\{\cos^{-1}\dfrac{\vec{V}_s\cdot\bar{M}}{|\bar{M}|}\right\}} \begin{vmatrix} \vec{i}_3 & \vec{j}_3 & \vec{k}_3 \\ v_1 & v_2 & v_3 \\ m_1 & m_2 & 0 \end{vmatrix} \tag{118}$$

where

$$\vec{V}_s = -\frac{\sin\eta}{|\bar{d}|\,|\bar{M}|\,\sin\left\{\cos^{-1}\dfrac{(\bar{d}\cdot\bar{M})}{|\bar{d}|\,|\bar{M}|}\right\}}\begin{vmatrix} \vec{i}_3 & \vec{j}_3 & \vec{k}_3 \\ m_1 & m_2 & 0 \\ d_1 & d_2 & 0 \end{vmatrix} + \cos\eta\,\frac{\bar{d}}{|\bar{d}|} \qquad (119)$$

$$= v_1\,\vec{i}_3 + v_2\,\vec{j}_3 + v_3\,\vec{k}_3.$$

The plane containing the slit is tangent to the moon when the vector normal to the plane containing the slit, $\vec{n}$, is coincident with the moon radius vector, $\bar{R}$, and the radius vector is directed at the point of tangency. The vector $\bar{R}$ is shown in figure 34 and is given by

$$\bar{R} = R\,(\cos\delta\cos\phi \;\vdots\; \cos\delta\sin\phi \;\vdots\; \sin\delta)\begin{pmatrix}\vec{i}_1\\ \vec{j}_1\\ \vec{k}_1\end{pmatrix} \qquad (120)$$

Vectors $\bar{R}$ and $\vec{n}$ are coincident when

$$\frac{\bar{R}}{R} = \pm\vec{n}. \qquad (121)$$

There are three unknowns in equation (121), namely, ϕ, δ, ω, so at least two additional equations are required before the point of tangency is known. Since the vector $\bar{M}$ lies in the plane containing the slit, $\bar{M}$ is orthogonal to $\bar{R}$ when the tangency condition exists, so

$$\bar{M}\cdot\bar{R} = 0 \qquad (122)$$

Also, since $\vec{V}_s$ lies in the plane containing the slit

$$\vec{V}_s\cdot\bar{R} = 0 \qquad (123)$$

An additional relationship is available because vector $\bar{G}$ lies in the plane containing the slit, so

$$\bar{G}\cdot\bar{R} = (\bar{R}-\bar{C})\cdot\bar{R} = 0. \qquad (124)$$

Two solutions should result for ω because of equation (121), one solution, ω_1, should correspond to the moon entering the slit and the second solution, ω_2, should correspond to the moon leaving the slit. For $\omega_1 \le \omega \le \omega_2$, the moon intersects the slit.

Let us define an incremental value of ω such that

$$\Delta\omega = \frac{\omega_2 - \omega_1}{r} \tag{125}$$

where r is some integer which will provide enough data points for a sufficiently accurate plot of H versus ω. As ω is incremented from ω_1 to

$$\omega = \omega_1 + \Delta\omega \tag{126}$$

the moon image will pass into the slit gap and the plane containing the slit will slice the volume of the moon body. However, the normal to the plane containing the slit may not necessarily be coincident with the $\vec{k}$ axis as required by equations (91) or (105); therefore, a coordinate transformation is required. Let the new k axis designated by $\vec{k}_o$ be coincident with $\vec{n}$.

$$\vec{k}_o = \vec{n} \,. \tag{127}$$

Now, define the new $\vec{i}$ axis as

$$\vec{i}_o = \vec{n} \times \vec{k}_1 \tag{128}$$

so

$$\vec{j}_o = \vec{k}_o \times \vec{i}_o \,. \tag{129}$$

After the transformation to the $\vec{i}_o - \vec{j}_o - \vec{k}_o$ coordinate system, it is necessary to determine the new value for ν in equations (91) and (105). Figure 37 shows the geometry when the moon radius vector $\vec{R}$ lies in the same plane

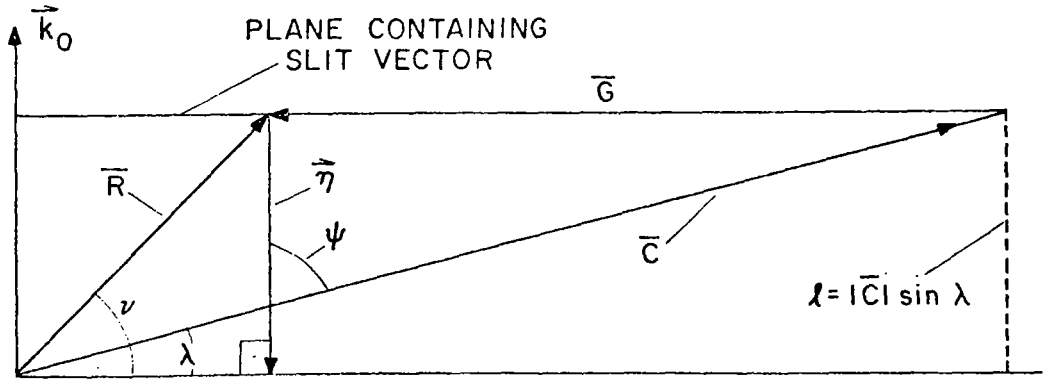

Figure 37: Geometry for determination of ν.

as the moon-spacecraft vector $\overline{C}$. Since the G vector must lie in the plane containing the slit when the elemental area on the moon surface is subtended by the slit gap, then the distance ℓ between the $\vec{i}_o - \vec{j}_o$ plane and the plane containing the slit is

$$\ell = |\overline{C}| \sin \lambda \tag{130}$$

but

$$\lambda = \frac{\pi}{2} - \psi \text{ and} \tag{131}$$

$$\psi = \cos^{-1} \frac{\overline{N} \cdot \overline{C}}{|\overline{C}|} \tag{132}$$

so

$$\nu = \sin^{-1} \frac{\ell}{|\overline{R}|} \quad . \tag{133}$$

Now, with all vectors defined in the $\vec{i}_o - \vec{j}_o - \vec{k}_o$ coordinate system, numerical computation of H may be performed for $\omega = \omega_1 + \Delta\omega$.

For the next increment of ω with

$$\omega = \omega_1 + 2\,\Delta\omega$$

a new transformation to the $\vec{i}_o - \vec{j}_o - \vec{k}_o$ coordinate system as given by equations (127), (128), and (129) must be determined in order to have $\vec{k}_o$ axis normal to the plane containing the slit. This transformation must be repeated after each increment in ω. Also, for each ω increment, a new value of ν must be computed from equations (130) through (133).

The image of the moon center at the optical system focal plane is centered in the slit gap when $\nu = 0$. This is the moon position in the slit gap which is ideally required for computing the trajectories for the moons of Mars.

After the plot of H versus ω has been obtained, this characteristic should be used as an input to the electronic filter used in the sensor in order to get a true picture of the signals obtained by scanning a moon body. Therefore, if h(t) is the filter impulse response, the filter output is given by

$$y(t) = \int H\left(\frac{2\pi}{T}\,\tau\right) h(t - \tau)\, d\tau \tag{134}$$

where

$$H\left(\frac{2\pi}{T}\,t\right)$$

is determined from the H versus ω data points and the angular rotation rate of the vehicle about its spin axis.

After y(t) has been numerically determined, it is possible to accurately evaluate errors in detecting the condition where $\nu = 0$ by threshold detection of the moon signal. Thus, it should be possible to determine accurate correction factors for moon detections if the sun phase angle and distance between moon and spacecraft are known.

Sensor Bright Source Shield

The sensor shield is illustrated in figure 38. This shield design provides the following characteristics:

(1) No directly illuminated element is visible from the aperture of width a to the lens.

(2) No secondarily illuminated surface is visible from the aperture to the lens.

(3) At least three bounces occur prior to entering the lens aperture.

The dimensions for the shield are determined based on the minimum volume which maintains the above characteristics. The volume for the shield may be derived from the geometry shown in figure 38.

The angle y of triangle 1-2-3 equals

$$y = \pi - \left(\pi - \left[\frac{\pi}{2} - \frac{\theta}{2}\right]\right) - \left(\frac{\pi}{2} - \alpha\right) \tag{135}$$

$$= \alpha - \frac{\theta}{2} .$$

So from the Law of Sines for triangle 1-2-3,

$$\frac{p}{\sin\left(\frac{\pi}{2} - \alpha\right)} = \frac{a}{\sin\left(\alpha - \frac{\theta}{2}\right)} \tag{136}$$

Therefore,

$$h_1 = p \cos\frac{\theta}{2} \tag{137}$$

$$= \cos\frac{\theta}{2}\left[\frac{a \cos\alpha}{\sin\left(\alpha - \frac{\theta}{2}\right)}\right]$$

From right triangle 2-6-3,

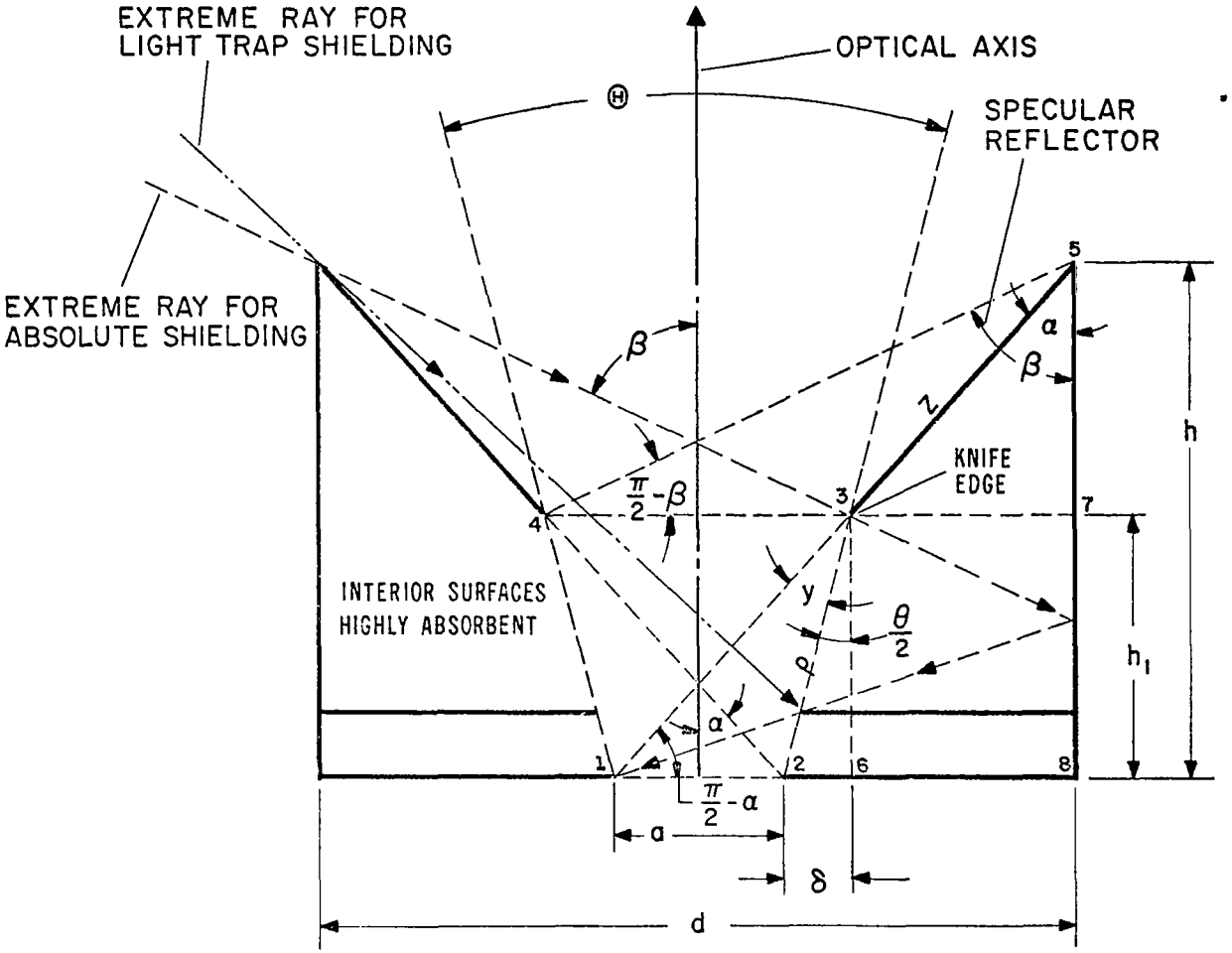

Figure 38: Bright object shield geometry showing shield cross-section and principal angles.

$$\delta = p \sin \frac{\theta}{2} \tag{138}$$

$$= a \frac{\cos \alpha \sin \frac{\theta}{2}}{\sin \left(\alpha - \frac{\theta}{2}\right)}$$

Using the Law of Sines for triangle 3-4-5,

$$\frac{Z}{\sin \left(\frac{\pi}{2} - \beta\right)} = \frac{a + 2\delta}{\sin (\beta - \alpha)} \tag{139}$$

which may be written as

$$Z = a \frac{\cos \beta}{\sin (\beta - \alpha)} \left[\frac{\sin \left(\alpha - \frac{\theta}{2}\right) + 2 \cos \alpha \sin \frac{\theta}{2}}{\sin \left(\alpha - \frac{\theta}{2}\right)}\right] \tag{140}$$

$$= a \frac{\cos \beta}{\sin (\beta - \alpha)} \left[\frac{\sin \left(\alpha + \frac{\theta}{2}\right)}{\sin \left(\alpha - \frac{\theta}{2}\right)}\right]$$

From right triangle 3-7-5,

$$h - h_1 = Z \cos \alpha \tag{141}$$

$$= a \cos \alpha \cos \beta \frac{\sin \left(\alpha + \frac{\theta}{2}\right)}{\sin (\beta - \alpha) \sin \left(\alpha - \frac{\theta}{2}\right)}$$

so

$$h = \frac{a \cos \alpha \left[\cos \beta \sin \left(\alpha + \frac{\theta}{2}\right) + \cos \frac{\theta}{2} \sin (\beta - \alpha)\right]}{\sin (\beta - \alpha) \sin \left(\alpha - \frac{\theta}{2}\right)} \tag{142}$$

$$= a \cos^2 \alpha \frac{\sin \left(\beta + \frac{\theta}{2}\right)}{\sin (\beta - \alpha) \sin \left(\alpha + \frac{\theta}{2}\right)} .$$

From right triangle 1-8-5,

$$\frac{\frac{d}{2} + \frac{a}{2}}{h} = \tan \alpha. \tag{143}$$

Therefore, the sunshield may be enclosed in a volume, V

$$V = \frac{\pi}{4} d^2 h \tag{144}$$

$$= \frac{\pi}{4} (2 h \tan \alpha - a)^2 h$$

$$= \frac{\pi}{4} h a^2 \left[\frac{\sin 2\alpha \sin \left(\beta + \frac{\theta}{2}\right) - \sin \left(\alpha - \frac{\theta}{2}\right) \sin (\beta - \alpha)}{\sin \left(\alpha - \frac{\theta}{2}\right) \sin (\beta - \alpha)} \right]^2$$

$$V = \frac{\pi}{4} a^3 \sin \left(\beta + \frac{\theta}{2}\right) \frac{\left[\cos \alpha \sin (\alpha + \beta) \sin \left(\alpha + \frac{\theta}{2}\right)\right]^2}{\left[\sin (\beta - \alpha) \sin \left(\alpha - \frac{\theta}{2}\right)\right]^3}$$

Now, the normalized volume function defined as

$$F(\alpha, \beta, \theta) = \frac{V}{a^3} \tag{145}$$

may be plotted as a function of α for fixed θ and β. A typical curve is shown in figure 39 which shows the normalized volume is minimized for some α within the range

$$\frac{\theta}{2} < \alpha < \beta.$$

The normalized minimum volume was obtained for $\theta = 20^\circ$ and $\beta = 40^\circ$. The shield dimensions for a clear optical aperture of a = 0.5 inches are shown in figure 40.

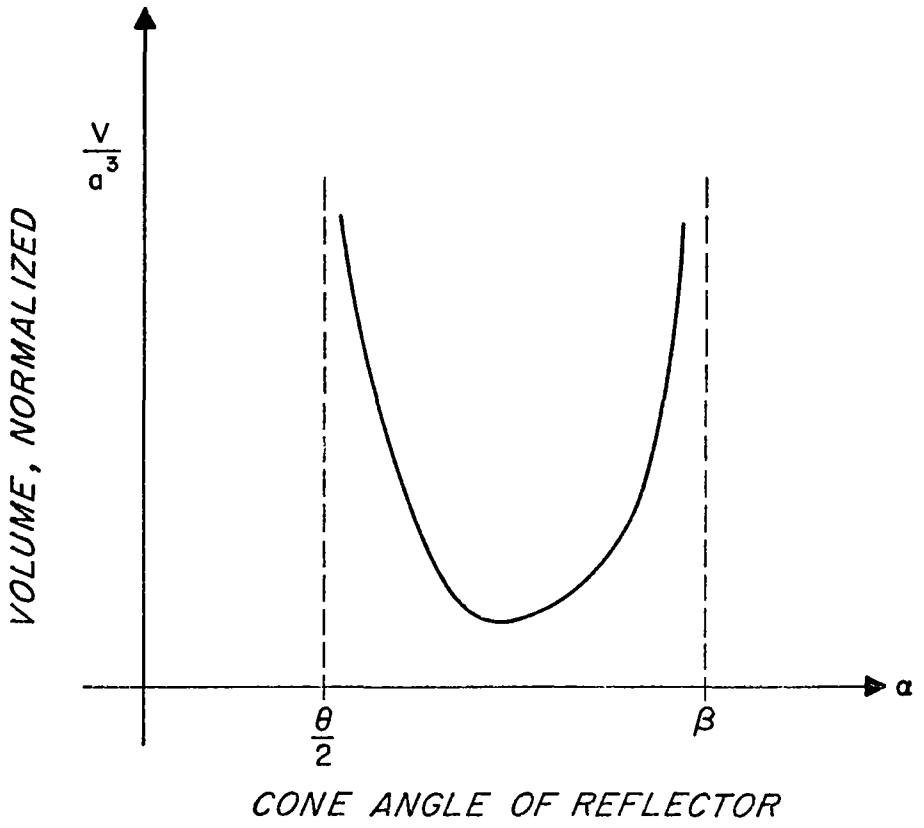

$$\frac{V}{a^3} = \frac{\pi \sin(\beta + \frac{\theta}{2})[\cos\alpha \sin(\beta+\alpha)\sin(\alpha+\frac{\theta}{2})]^2}{4[\sin(\alpha-\frac{\theta}{2})\sin(\beta-\alpha)]^3}$$

Figure 39: Normalized light baffle volume versus shield angle.

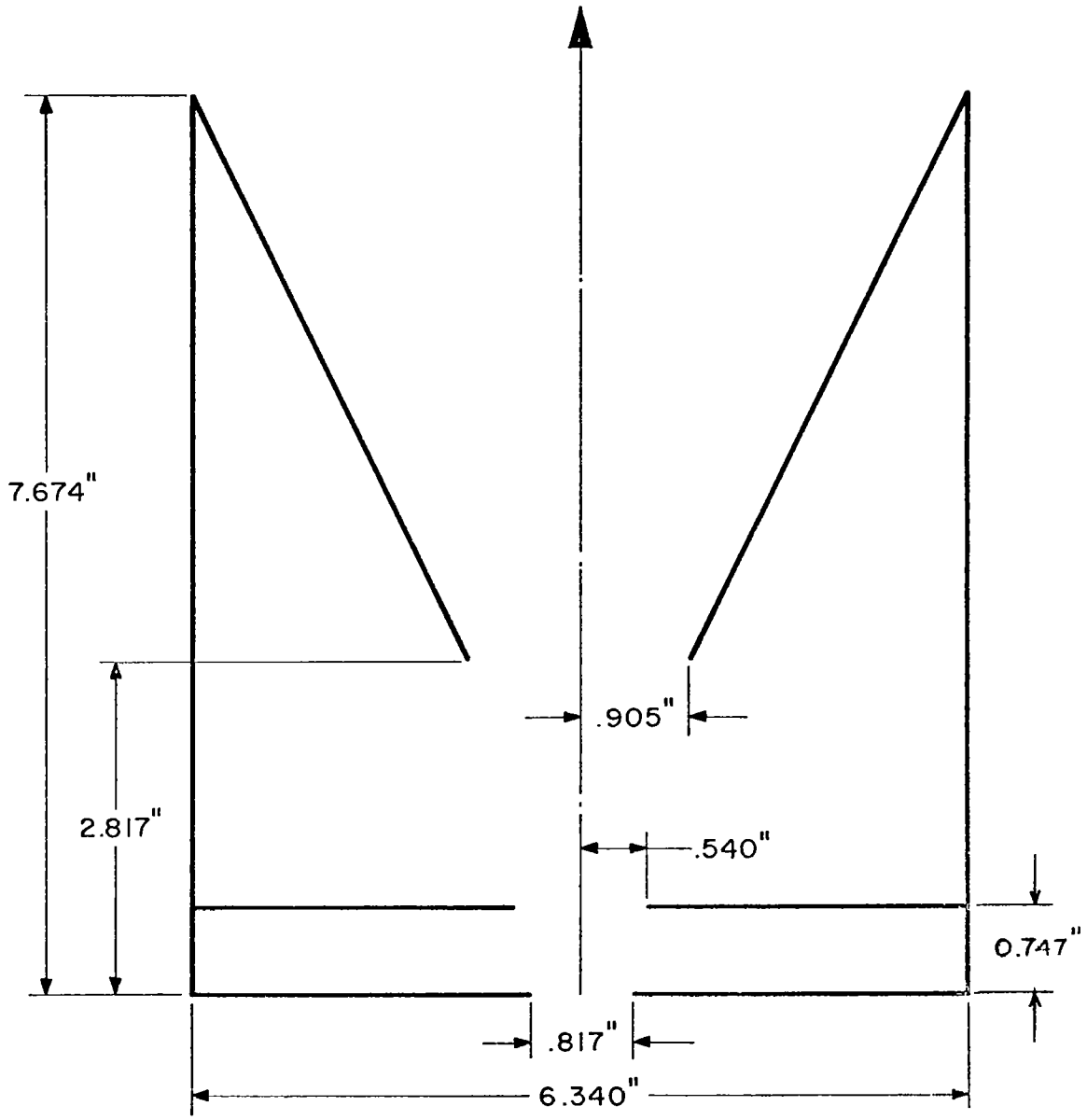

Figure 40: Shield dimensions.

CONCLUDING REMARKS

Perturbation of Spacecraft Due to Moons

A method of computing the perturbations by use of a linearization about a single reference Kepler orbit was first developed. The resultant formula is given by equation (5). Here an integration of an explicit function is required.

Numerical results are given for the following values of the unperturbed elements of the spacecraft's orbit:

$i = 0^{\circ}, 40^{\circ}$

$a = 20415.5$ km

$e = 078199$

$Tp = 0$ hr

$0 \leq \omega \leq 180^{\circ}$

$0 \leq \Omega \leq 360^{\circ}$

Since asymmetry exists, all values of ω and Ω were studied.

Results for the case $i = 40^{\circ}$ are summarized on page 24. A physical rationale is then given for these results. It is expected that these results may be generalized for all inclinations other than those near or equal to zero.

For inclinations at or near zero, a collision of the spacecraft and Phobos is possible under certain initial conditions. If initial conditions near these are chosen, long-track perturbations result which are positive or negative. A canceling effect is thus possible and does occur if the positive and negative yielding initial conditions occur relatively near each other.

The results given can be generalized to other cases except those near resonance. That is, cases in which the ratio of the spacecraft's period to a moon's period is a rational fraction whose numerator and denominator are relatively small. For these cases, the perturbations grow large, and equation (5) may not be valid.

Availability of the Moons

The strongest single factor which hinders the detectability of the moons is the scattering of Mars reflected sunlight into the instrument field of view. This problem is not too serious in case of Deimos, but is more serious for Phobos because of its relatively low orbital altitude.

A clear picture of the availability of Phobos as a function of spacecraft orbital parameters does not emerge. In four percent of the cases examined eleven spacecraft orbits yielded no Phobos detections. If, however, a large number of spacecraft orbits are allowed ($\approx$ 80), a sufficient number of Phobos detections will occur.

Navigational Problem

The orbits of the spacecraft, moons, and the potential of Mars can be determined by observing the parallax of the moons as viewed from the spacecraft. If the direction is measured with an accuracy of one minute of arc, then after eighty spacecraft orbits (a = 20,415.5 km) the position errors of the spacecraft and Deimos are about 4 km. Because few sightings of Phobos ($\approx$ 10) occur, its computed position has approximately twice this error.

The lower harmonics, i.e., the coefficients of the Legendre functions of degree two, are quite well determined by the measurements, but the higher harmonics are not. This occurs not because of a defect in the measurement, but because of the relatively high altitude of the three bodies and the relatively small values assumed for the higher coefficients.

Not only are the higher harmonics poorly determined by the measurements, but if these harmonics are assumed known and the assumed values are slightly in error, then only small degradation is transmitted to the solved for unknowns. Also, the effect of an error in the mass of Mars does not increase as a longer data gathering interval is used.

Attitude and Moon Direction Determination

Both the accuracy of attitude determination and the direction to a moon are functions of the detectable stellar background. Moreover, the accuracy of the moon direction is a function of its position in

the field of view. In general, the proposed instrument can determine the attitude to an accuracy of approximately three minutesof arc and that of the direction to a moon to approximately five minutes of arc. These error estimates can be reduced for the same instrument if a less complicated attitude motion model were allowed. That is, if it were allowed to assume the attitude were constant, or varied linearly for a time interval longer than five minutes.

Instrumentation

A feasible sensor design was derived which has the dynamic range capability to detect the moons of Mars as well as stars as dim as 2.2 magnitude. Primary components for the sensor consist of a sunshield, refractive optics, slit reticle, photomultiplier, angle encoder, and brushless D. C. motor. The sunshield, optics, and slit reticle form an assembly which is rotated with a sixty second period. The overall power requirement is 7.9 watts and the entire instrument weight was determined as seven pounds. Analysis showed that instrumentation errors could be kept within the limits imposed for the calculation accuracies required for calculation of spacecraft and moon orbits as well as the Mars potential.

APPENDIX A

EXPLICIT FORMULAS FOR $U(u, \tau)$ and $V(u, \tau)$

In the analysis concerning the "Perturbations of the Spacecraft Due to the Moons", two matrices, $U(u, \tau)$ and $V(u, \tau)$ were introduced. The final equation (7) for these perturbations was a function of these matrices. As given in the text,

$$U(u, \tau) = (-\alpha_1(\tau)\ \alpha_2'(u) + \alpha_2(\tau)\ \alpha_1'(u))/n^*(1 + e)$$

$$+ \frac{3(nT + \tau)}{1 - e} \begin{pmatrix} b_1(\tau)\ c_1(u) & b_1(\tau)\ c_2(u) & 0 \\ b_2(\tau)\ c_1(u) & b_2(\tau)\ c_2(u) & 0 \\ 0 & 0 & 0 \end{pmatrix}$$

$$V(u, \tau) = -\frac{3}{1 - e} \begin{pmatrix} b_1(u)\ c_1(\tau) & b_2(u)\ c_1(\tau) & 0 \\ b_1(u)\ c_2(\tau) & b_2(u)\ c_2(\tau) & 0 \\ 0 & 0 & 0 \end{pmatrix}$$

where

$$\alpha_1 = \begin{pmatrix} a_{11} & a_{12} & 0 \\ a_{21} & a_{22} & 0 \\ 0 & 0 & a_{33} \end{pmatrix}$$

$$\alpha_2 = \begin{pmatrix} a_{14} & a_{15} & 0 \\ a_{24} & a_{25} & 0 \\ 0 & 0 & a_{36} \end{pmatrix}$$

$$c_1 = a_{12} - a_{14}$$

$$c_2 = a_{22} - a_{24}$$

The equations for α_1, a_2, b_1, b_2, c_1, and c_2 are as follows:

$$a_{11}(t) = \frac{1}{1 - e^2}\left[\frac{2\,r(1 + e)^2}{p} - \frac{p}{r} + 1 - (1 + e - e^2)\cos\nu\right]$$

$$a_{12}(t) = \sin\nu$$

$$a_{21}(t) = \frac{1 + e}{1 - e}\sin\nu\left(1 + \frac{r}{p}\right)$$

$$a_{22}(t) = -\frac{r}{p} + \left(\frac{r}{p} + 1\right)\cos\nu$$

$$a_{33}(t) = \frac{r}{p}(1 + e)\cos\nu$$

$$a_{14}(t) = \frac{1}{1 + e}\sin\nu$$

$$a_{15}(t) = \frac{1}{1 - e}\left[-\frac{2 + e}{1 + e}\cos\nu + \frac{2r}{p}(1 + e) + \frac{1}{1 + e}\left(1 - \frac{p}{r}\right)\right]$$

$$a_{24}(t) = \frac{1}{1 - e}\left[\left(\frac{r}{p} + 1\right)\cos\nu - \frac{2}{1 + e}\frac{p}{r} + \frac{er}{p}\right]$$

$$a_{25}(t) = \frac{2}{1 - e}\sin\nu\left(1 + \frac{r}{p}\right)$$

$$a_{36}(t) = \frac{r}{p}\sin\nu$$

$$b_1(t) = -e\sin\nu$$

$$b_2(t) = \frac{p}{r}$$

$$c_1(t) = \frac{e}{1 + e} \sin \nu$$

$$c_2(t) = \frac{1}{1 - e}\left[\frac{2}{1 + e}\frac{p}{r} - \frac{r}{p} - \left(\frac{r}{p} + 1\right) e \cos \nu\right]$$

where r and ν are functions of t.

APPENDIX B

DETERMINATION OF USABILITY OF $\overline{P}$ AS A POSITION OF OBSERVATION IN THE PRESENCE OF A SUNLIT HEMISPHERE

We are given: (figure 41)

- $\hat{s}$ direction to sun
- $\overline{P}$ position of observer
- $\hat{c}$ direction of optical axis
- r radius of sphere centered at (0, 0, 0)
- β minimum acceptable angle to sunlit sphere, $\beta > 0$

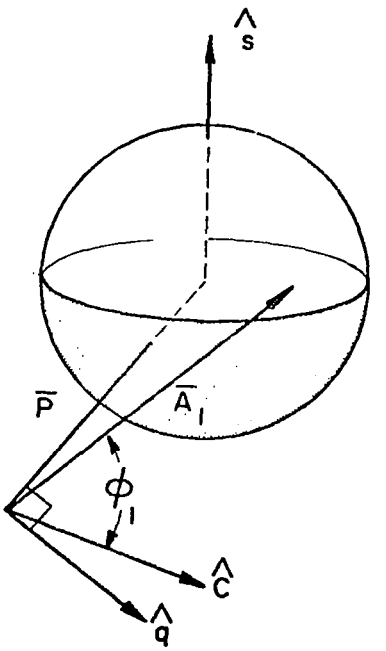

Figure 41: Geometry of the sunlit hemisphere.

Consider the set of all points on the sunlit hemisphere and denote this set as H. Let ϕ be the angle from the optic axis, $\hat{c}$, to a line joining the terminus of $\overline{P}$ with a point of H. Finally, let ϕ_m be the minimum value of ϕ over the set H, and let $\overline{A}_m$ be the vector from the observer to that point of H which gives rise to ϕ_m. Now, we define $\overline{P}$ as usable if $\phi_m \geq \beta$. Otherwise, it is not usable.(4) The problem is to develop a criterion as to whether or not $\overline{P}$ is uable.

Two major cases must be considered as to whether or not the positively extended optical axis intersects the shpere. Suppose

$$\hat{c} \cdot \overline{P} < 0 \text{ and } D^2 = (\hat{c} \cdot \overline{P})^2 - P^2 + r^2 > 0, \; P = |\overline{P}|.$$

For this case, the positively extended optical axis intersects the sphere. The distance to the sphere in the direction of $\hat{c}$ is

$$\lambda = - \hat{c} \cdot \overline{P} - D$$

and the vector from the origin to the point at which the extended optical axis first intersects the sphere is

$$\overline{B} = \lambda \hat{c} + \overline{P}.$$

Now,

$$\overline{B} \cdot \hat{s} \geq 0 \rightarrow \overline{P} \text{ is not usable.}$$

If $\overline{B} \cdot \hat{s} < 0$, additional tests are required to determine the state of $\overline{P}$, but if any point of H is visible from the terminus of $\overline{P}$, then $\overline{A}_m$ lies on the boundary of H, i.e., $\hat{s} \cdot \overline{A}_m = 0$.

Define

$$\hat{p}_1 \text{ such that } \hat{p}_1 \cdot \hat{s} = 0 \text{ and } \hat{p}_1 = \mu_1 \hat{s} + \mu_2 \overline{P}, \; \mu_2 \geq 0.$$

---

(4) The problem of direct obscuration of a moon by Mars is not considered here, but is an additional test which is imposed later. For the additional test the moon's position must also be given.

Hence,

$$\hat{p}_1 = \frac{\overline{P} - \overline{P} \cdot \hat{s}\,\hat{s}}{\left|\overline{P} - \overline{P} \cdot \hat{s}\,\hat{s}\right|} .$$

Also define $\hat{p}_2 = \hat{s} \times \hat{p}_1$. Now, if $r > \overline{P} \cdot \hat{p}_1$, then no point of H is visible from the terminus of $\overline{P}$; hence, $\overline{P}$ is usable.

Suppose $r \leq \overline{P} \cdot \hat{p}_1$. Then let

$$\cos \theta_1 = \frac{r}{\overline{P} \cdot \hat{p}_1} \leq 1, \quad 0 \leq \theta_1 \leq \pi.$$

Define

$$\hat{\mu} = \cos \theta \, \hat{p}_1 + \sin \theta \, \hat{p}_2, \quad -\theta_1 \leq \theta \leq \theta_1.$$

$$\overline{A}(\theta) = r \, \hat{\mu} - \overline{P}$$

Now, $\overline{A}(\theta)$ is a vector from the observer to that portion of the boundary of H which is visible to the observer. So, $\overline{A}_m$ is a member of the set $\overline{A}(\theta)$.

If $\overline{A} \cdot \hat{c} \leq \left|(A(\theta))\right| \cos \beta$, for $-\theta_1 \leq \theta \leq \theta_1$; then $\overline{P}$ is usable. Otherwise $\overline{P}$ is not usable.

We now must consider the second major case, i.e., the positively extended optical axis does not intersect the sphere. Hence, $\hat{c} \cdot \overline{P} \geq 0$ or $D^2 < 0$.

Consider all points on the sphere, i.e., the set $r \hat{r}$ for all unit vectors $\hat{r}$. Let $\overline{A} = r \hat{r} - \overline{P}$. Define $\overline{A}_1$ such that

$$\overline{A}_1 \cdot \hat{c} = \text{max. over all } \hat{r}.$$

Then,

$$\overline{A}_1 = \left(\frac{r^2}{p^2} - 1\right) \overline{P} + \frac{r}{p} \sqrt{P^2 - r^2} \, \hat{q}$$

where

$$\hat{q} = \frac{P^2\,\hat{c} - (\hat{c} \cdot \overline{P})\,\overline{P}}{\left|P^2\,\hat{c} - (\hat{c} \cdot P)\,P\right|} .$$

Let

$$\overline{Q}_1 = \overline{A}_1 + \overline{P} = \frac{r^2}{P^2}\,\overline{P} + \frac{r}{P}\,\sqrt{P^2 - r^2}\,\hat{q}.$$

Now, suppose $\overline{Q}_1 \cdot \hat{s} \geq 0$, then the terminus of $\overline{Q}_1$ lies in H. Hence, $\overline{A}_1 = \overline{A}_m$ and $\overline{P}$ is usable if

$$\overline{A}_1 \cdot \hat{c} \leq |\overline{A}_1| \cos \beta.$$

Otherwise $\overline{P}$ is not usable.

If $\overline{Q}_1 \cdot \hat{s} < 0$, then $\overline{A}_m$ lies on that part of the boundary of H that is visible to the observer. The problem is thus reduced to a previous case.

A flow diagram is given in figure 42.

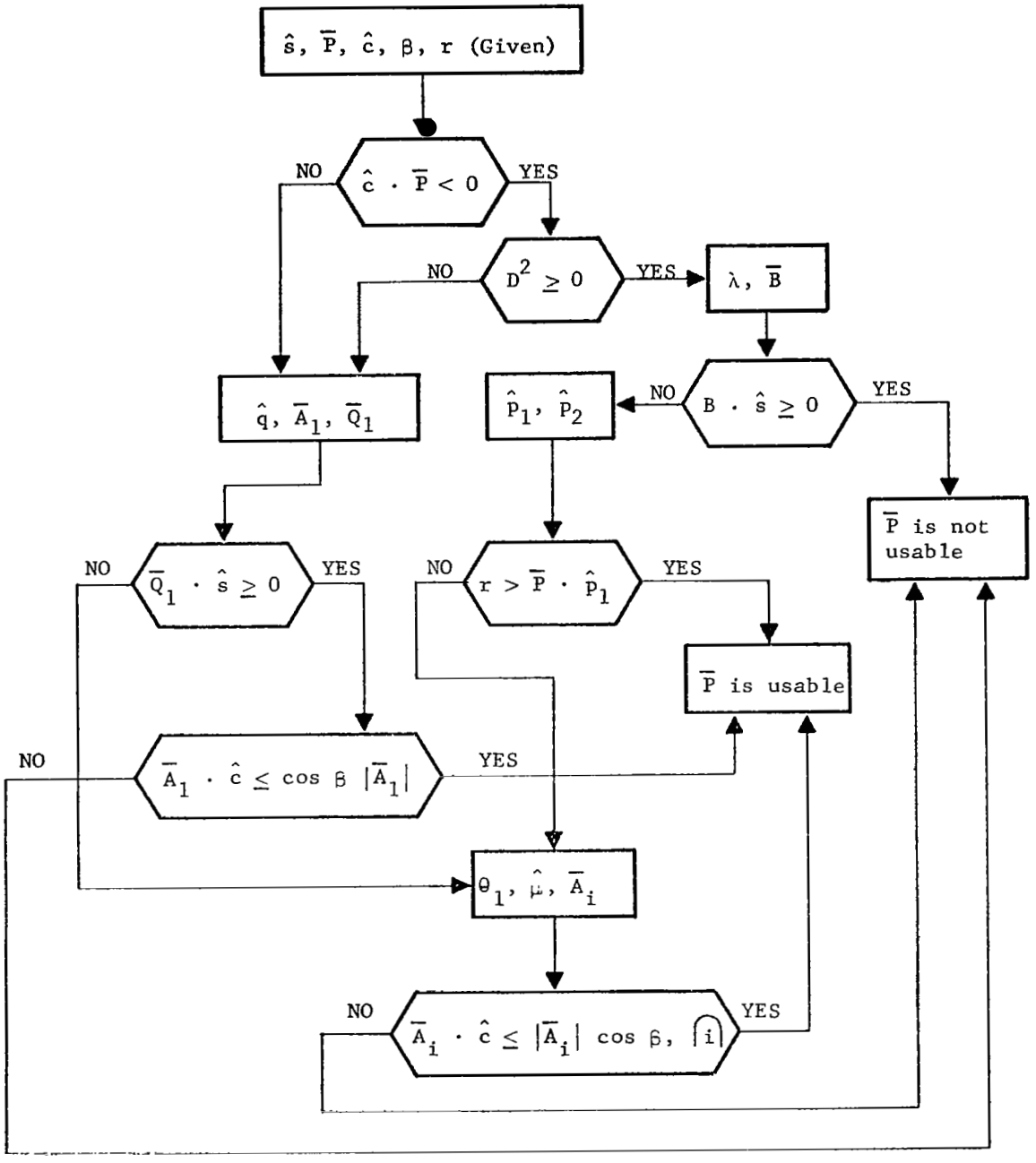

Figure 42: Flow chart to determine the usability of $\overline{P}$.

APPENDIX C

DETERMINATION OF THE INSTRUMENT MAGNITUDE OF MOONS

Assume the moons are spherical diffuse reflectors. Then,

$$H = \frac{8\ a\ L}{27} \left(\frac{\rho}{r}\right)^2 \frac{\sin \phi + (\pi - \phi) \cos \phi}{\pi}$$

where (figure 43)

H = flux (watts/m^2) at the position of the observer due to sun reflected light from a moon of Mars

a = moon albedo (assumed 0.1)

L = flux from sun in the vicinity of Earth (watts/m^2)

ρ = radius of moon

r = distance of observer from moon's center

ϕ = phase angle (radians)

If we assume a detector at the observer whose response is uniform for $.38 \leq \lambda \leq .6$ microns, then

$L = 418.1$ watts/m^2 (reference 18)

The magnitude of the moon as seen by the observer is then $m = -2.5 \log \frac{H}{H_o}$, where

H_o = flux from a m = 0 source received at a detector behind a lens system with 80% optical efficiency

$= 8.36 \times 10^{-9}$ watts/m^2 (reference 10, p. V-3)

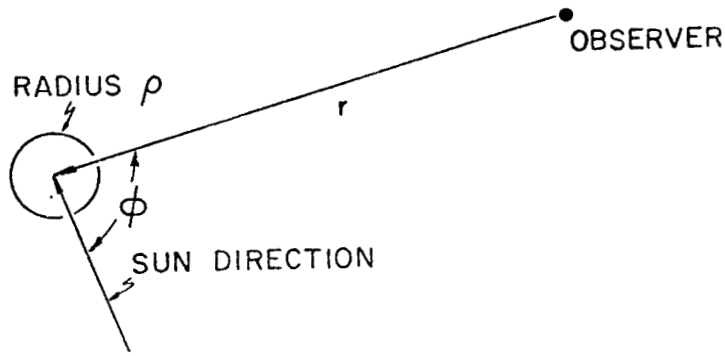

Figure 43: The phase angle, ϕ.

REFERENCES

1. Grosch, Charles B., and Paetznick, Harlan R.: Method of Deriving Orbital Perturbing Parameters from Onboard Orbital Measurements of an Ejected Probe or a Natural Satellite. NASA CR - 1412, 1969.

2. Lewis, William B., and Vannelli, Bruce D.: Self-Contained Navigation Experiment. NASA CR-105920, 1969.

3. Redmond, John C., and Fish, Ferol F.: The Luni-Tidal Interval in Mars and the Secular Acceleration of Phobos. Icarns, vol. 3, no. 2, July 1964, pp. 87-91.

4. Enhanced Photo Shows Mars' Moon", Aviation Week and Space Technology, May 25, 1970.

5. Battin, Richard H.: Astronautical Guidance McGraw-Hill Book Co., Inc., 1964.

6. Kochi, K. C.: Exact First-Order Navigation Guidance Mechanization and Error Propagation Equations for Two-Body Reference Orbits. AIAA Journal, vol. 2, no. 2, February 1964, p. 365.

7. Harrison, Edwin F., and Campbell, Janet W.: Reconnaissance of Mars Satellites. Paper presented at 8th Aerospace Sciences Meeting, AIAA (New York, New York), January 1970.

8. LaBonte, Anton E.: Study of a Scanning Attitude Determination System (SCADS) for a Synchronous Satellite. NASA CR-100149, 1968.

9. Hansen, Peter D.: New Approaches to the Design of Active Filters. The Lightning Empiricist, Vol. 13, no. 1-2, Philbrick Research, Inc., 1965.

10. Farrel, Edward J., Zimmerman, Duane C., Nickel, Donald F., and Borden, Richard C.: A Theoretical Investigation of Information Limits of Scanning Systems. NASA CR-672, 1967.

11. Nickel, Donald F., and Grosch, Charles B.: Feasibility Study of Scanning Celestial Attitude Determination System for Small Scientific Spacecraft. NASA CR-95807, 1967.

12. Allen, C. W.: Astrophysical Quantities. The Athlone Press, 1963.

13. Mooers, Alden J.: Breadboard Design of a Scanning Celestial Attitude Determination System. NASA CR-91532, 1967.

14. Mityashev, B. V.: The Determination of Time Position of Pulses in the Presence of Noise. MacDonald and Company, 1965.

15. Parzen, E.: Stochastic Processes. Holen-Day, Inc., 1962.

16. Meisenholder, G. W.: Planet Illuminance California Institute of Technology. Technical Report No. 32-361, 1962.

17. Smith, Warren J.: Modern Optical Engineering. McGraw-Hill Book Company, Inc., 1966.

18. Handbook of Geophysics. Revised ed., Macmillan , 1961.

NASA-Langley, 1971 —— 21 CR-1805